A Search for Signatures of Dark Matter in the AMS-01 Electron and Antiproton Spectrum

by

Gianpaolo Patrick Carosi

Bachelor of Science, Harvey Mudd College (2000)

Submitted to the Department of Physics
in partial fulfillment of the requirements for the degree of

Doctor of Philosophy

at the

MASSACHUSETTS INSTITUTE OF TECHNOLOGY

January 2006

Author ....
Department of Physics
Jan 13th, 2006

Certified by ....
Peter Fisher
Professor
Thesis Supervisor

Certified by ....
Kate Scholberg
Assistant Professor
Thesis Supervisor

Accepted by ....
Thomas Greytak
Associate Department Head for Education

A Search for Signatures of Dark Matter in the AMS-01 Electron and Antiproton Spectrum

by

Gianpaolo Patrick Carosi

Submitted to the Department of Physics
on Jan 13th, 2006, in partial fulfillment of the
requirements for the degree of
Doctor of Philosophy

Abstract

If dark matter consists of Weakly Interacting Massive Particles (WIMPs), such as the supersymmetric neutralino, various theories predict that their co-annihilation in the galaxy can give rise to anomalous features in the otherwise smooth spectra of charged cosmic rays. Up to now searches for these spectral anomalies have focused largely on antiparticles ($\bar{p}$, e^+) due to their lower astrophysical backgrounds. In this thesis we present results of a search for dark matter co-annihilation in the charge $Z = -1$ spectrum of AMS-01 (essentially electrons and antiprotons). To avoid model dependent complications we assume that the primary co-annihilation channel is through W^+W^- production. We use the galactic propagation software GALPROP to determine the dark matter spectra at Earth from a smooth isothermal source. Fits to the data did not reveal any contribution from dark matter and limits were placed on the rate of W^+W^- production in the galaxy and on the corresponding cross-section for WIMP annihilation through the W^+W^- channel (given a smooth isothermal distribution).

Thesis Supervisor: Peter Fisher
Title: Professor

Thesis Supervisor: Kate Scholberg
Title: Assistant Professor

Acknowledgments

There are a great many people who I'd like to thank for making this thesis possible. First of all I'd like to thank Prof. Peter Fisher for the initial idea of this work and for guiding me through the ups and downs of the analysis. This thesis would not exist without his assistance and support. Special thanks should also go to Dr. Andrew Strong (Max Planck Institute) and Dr. Igor Moskalenko (Stanford) whose GALPROP propagation software was essential to this analysis and who kindly answered many questions with regards to it. I'm also grateful for the valuable advice given to me by Prof. Edmund Bertschinger and Prof. Kate Scholberg. Prof. Scholberg first introduced me to the AMS experiment and guided me through my first few years at MIT and her insights and patience during that time was invaluable. A great deal of gratitude also goes to Prof. Ulrich Becker for showing me the essence of experimental technique and hardware development.

In addition to the Bldg 44 professors a large number of students have also assisted me throughout the years. Dr. Reyco Henning and Dr. Ben Monreal provided great graduate student role models and patiently explained many of the details of AMS analysis to me. Sa Xiao and Gray Rybka have directly contributed to this thesis by assisting me in the research. Feng Zhou, Marta Lewandowska, Scott Hertell, Dafne Baldassari, Bilge Demirkoz, Masha Kamenetska, Teresa Fazio, Tom Walker and Drew Werner all deserve me thanks for their help and friendship throughout these years.

Thanks should also go out to Prof. Sam Ting and the entire AMS collaboration, especially Dr. Vitaly Choutko for his explanations of aspects of the analysis and Dr. Mike Capell for his detailed assistance with my thesis. This thesis would never have been possible without the excellent detector built and flown by the AMS collaboration.

Finally I'd like to thank my family for all their support while I pursued my dreams of graduate school. Without them none of this would be possible.

Contents

List of Figures

List of Tables

Chapter 1

Introduction

The existence of dark matter presents a great mystery in our understanding of the universe [1]. Evidence for dark matter from gravitational effects on astrophysical bodies has been around for over 70 years [2] and strong arguments based on Big Bang nucleosynthesis, structure formation and recent precise cosmological measurements [3] essentially rule out all known particles. New particles, based on theoretical extensions to the standard model, could possibly account for this missing matter [1].

Perhaps the most widely studied of these potential dark matter candidates is the class of Weakly Interacting Massive Particles (WIMPs) which have the general properties of being stable, heavy (of order 10 GeV to several TeV) and interact with standard model particles at roughly the weak scale. A number of theoretical candidates fit this profile including the supersymmetric neutralino [4], Kaluza-Klein particles [5] and heavy 4th generation neutrinos [6].

A feature of WIMPs in most models is their ability to co-annihilate, in which two WIMP particles interact and annihilate into a variety of stable particles, such as neutrinos, photons, positrons, etc. Studies of structure formation in the galaxy require WIMPs to be moving non-relativistically (or else they would smooth out density fluctuations too quickly) which means their co-annihilation products will have energies directly related to their rest mass. Searches for signatures of these annihilation products are complementary to the large number of direct detection searches currently underway, which look for rare WIMP-nuclei scattering.

One of the favored channels to look for evidence of WIMP annihilation has been in the spectrum of cosmic ray positrons. Currently there are no known primary sources of antiparticles, such as positrons, so the backgrounds should consist entirely of secondary positrons created from spallation products, such as the decay of pions and kaons generated from protons interacting with interstellar gas [4], or from pair production from synchrotron radiation [7]. In a series of balloon experiments the HEAT collaboration [8] measured the positron spectrum up to 50 GeV. At approximately 10 GeV their spectrum began to deviate from the expected known sources in a manner that could be consistent with some models of dark matter annihilation. The low statistics and low energy of the measurements ruled out any definitive conclusions as to its spectral shape, though.

In June 1998 the AMS-01 experiment launched on the Space Shuttle Discovery for a

10 day mission in which it collected over 100 million cosmic rays, far more events then the three HEAT detection runs combined. Unlike the HEAT experiments AMS-01 did not have a way of discriminating positrons from the large background of protons at energies greater then 3 GeV. It could, however, easily discriminate the large number of charge $Z = -1$ events collected (primarily electrons) from $Z = +1$ events (mostly protons) due to their opposite charge signs. As a result we decided to make precision measurements of the $Z = -1$ spectrum to search for signatures of WIMP annihilation. The clearest signal would occur if WIMPs co-annihilated directly to e^+e^- pairs. Unfortunately most leading candidates are Majorana particles in which this channel is highly suppressed [4]. Alternatively, if the WIMP mass is large enough, it can co-annihilate into a W^+W^- pair which then decays to electrons, positrons, antiprotons, etc [9]. We will assume this is the major WIMP annihilation channel and use the PYTHIA simulation [10] to determine the primary $Z = -1$ spectra (electrons and antiprotons) for different WIMP masses. We will then use the galactic propagation software GALPROP [11] to determine the various distortions to this primary signal from diffusion through the galaxy. In the end we will make a statement as to the rate of W^+W^- production in the galaxy which will allow us to infer possible WIMP annihilation cross-sections which may then be fit to different WIMP models (including the neutralino).

Chapter 2 describes the evidence for dark matter, possible distributions and candidate particles, and the current state of the search for their direct and indirect detection. Chapter 3 then covers the astrophysical production and acceleration of cosmic rays, the primary background for our search, before describing the co-annihilation signal from dark matter and the propagation of these cosmic rays to earth. Chapter 4 describes the AMS-01 experiment and shuttle flight. Chapter 5 lays out the specific analysis techniques used to search for an anomalous dark matter feature in the AMS-01 $Z = -1$ spectrum. Chapter 6 presents the result of this search and Chapter 7 discusses the conclusions of this study and possible future work.

Chapter 2

Weakly Interacting Dark Matter

2.1 Evidence for Dark Matter

Dark matter, by its definition, interacts very weakly, if at all, with stable standard model particles such as photons, leptons, and baryons and has only been inferred to exist through its gravitational effects [4]. Evidence for it first appeared in the 1930s when Fritz Zwicky showed that velocity dispersions of galaxies in galactic clusters were too high for them to be gravitationally bound by the clusters' luminous matter [2]. A large amount of additional unseen gravitating matter was required to contain the member galaxies. Since then evidence for dark matter has steadily been accumulating on scales from dwarf galaxies (kiloparsecs) [4] to the size of the observable universe (Gigaparsecs) [3].

A common example of evidence for dark matter comes from the rotation curves of spiral galaxies. 21-cm line surveys of neutral hydrogen cloud velocities have been measured in many galaxies as a function of radius from the galactic core. The most common results have a flat velocity curve as a function of radius r (after a steep rise in velocity near the galactic center) such as in Figure 2-1 [12]. If there is only luminous matter in the galaxy the velocity of material orbiting the dense galactic core should decrease as $r^{-\frac{1}{2}}$. This implies that most galaxies are embedded in a large dark matter "halo" which extends far beyond the visible part of the galaxy and has a dark matter density which decreases as r^{-2}. Measurements using dwarf galaxies orbiting spiral galaxies yield similar results [13].

At larger scales clusters of galaxies provide evidence for dark matter from gravitational lensing [14], X-ray gas temperatures [15] and from the motion of member galaxies [2], all of which require large amounts of gravitating dark matter in order to match the observations. Measurements of galactic flows, such as the observation that the local group of galaxies is moving at 627 ± 22 km/sec with respect to the cosmic microwave background (CMB), also requires the presence of large amounts of unseen mas s[4]. Recent observations have also located a galaxy that appears to be made almost entirely out of dark matter. Many such "dark galaxies" are predicted by various models of dark matter [16].

Finally, global fits of cosmological parameters from measurements of the CMB with WMAP [3] and surveys of the distribution of galaxies yield the most accurate results

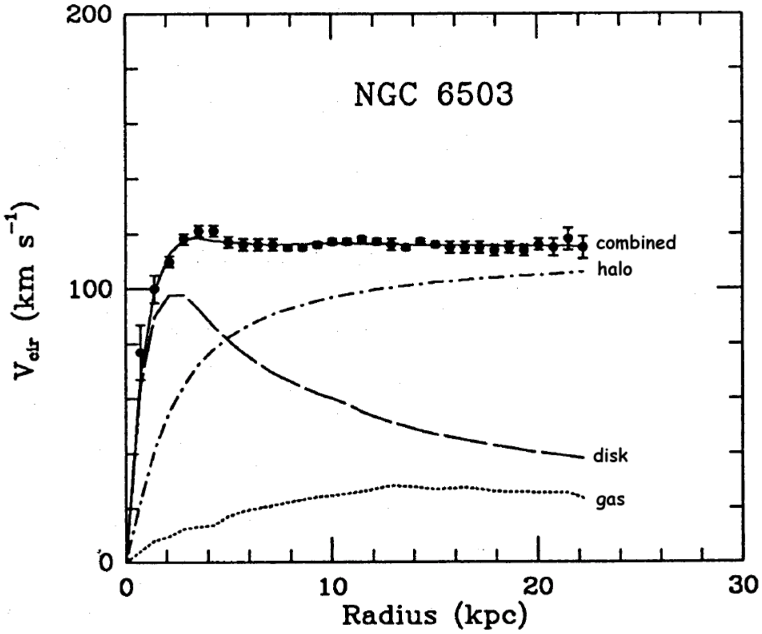

Figure 2-1: Rotation curve of galaxy NGC 6503 (from [12]). The solid line is a three parameter dark halo fit to the measured rotation curve points. The three components of the rotation curve are contributions from the luminous matter in the galactic disk, gas clouds and a presumed isothermal dark matter halo.

for the overall contribution of dark matter to the energy density of the universe. The current estimate of all gravitating matter (dark and ordinary) is given by $\Omega_{matter\ total}h^2 = 0.134 \pm 0.006$, where $h = .72$ is the Hubble constant in units of 100 km/sec/Mpc and Ω is energy density of universe as a fraction of the critical density. The successful predictions of the ratios of deuterium, ^{3}He, ^{4}He and ^{7}Li from Big Bang nucleosynthesis, along with the WMAP results, have determined $\Omega_{baryons}h^2 = 0.024 \pm 0.001$ requiring the majority of the dark matter ($\Omega_{DM}h^2 = 0.111 \pm 0.006$) to be non-baryonic [17].

2.2 Dark Matter Candidates

Non-baryonic dark matter models usually have a few generic characteristics. First, since these particles would be relics from the Big Bang, they should be stable particles whose calculated relic densities match observation [4]. Second, constraints from numerical simulations of structure formation in the early universe disfavor particles moving at relativistic velocities ("hot dark matter") because they smear out the density fluctuations required to form galaxies too quickly. For these reasons the majority of dark matter is thought to be "cold" (moving at galactic velocities on the order of hundreds of kilometers per second). This rules out the light standard model neutrinos as the dominant source of dark matter and recent combined cosmological fits have constrained their contribution to $\Omega_\nu h^2 \leq 0.0072$ (95% CL) [3].

A variety of non-baryonic dark matter candidates currently match these requirements including Weakly Interacting Massive Particles (WIMPs) such as the neutralino (the lightest supersymmetric particle) [4], Kaluza-Klein particles [5], which arise from theories of extra-dimensions, and heavy 4th generation neutrinos [6]. A general feature of many of these WIMP candidates is that they can, with varying degree, co-annihilate to standard model particles and would have cross-sections to do so at approximately the weak-scale ($\sigma \leq 1$ picobarn). This weak-scale coupling is the result of these WIMPs containing no electrical charge, no dipole moment and no strong-force color charge so that they can only interact via the weak-force and gravity (the latter of which was the original source of dark matter detection). Much of the later discussion on detecting neutralino co-annihilation products can be applied to other WIMP candidates as well. Another well motivated candidate is the axion, which is predicted from QCD symmetry breaking. These are extremely light particles ($10^{-6} - 10^{-3}$ eV) which could be detected by resonantly converting them to photons in a strong magnetic field [18]. The AMS experiment is not sensitive to axions and they will not be discussed any further. Other candidates include primordial black holes from the Big Bang which would have formed before Big Bang nucleosynthesis took place (or be counted as baryonic dark matter). These have not been studied in as much detail as WIMPs and will not be discussed here [4].

The present average WIMP density in the universe can be calculated if they were in thermal and chemical equilibrium with standard model particles directly after inflation. While in equilibrium the WIMPs would co-annihilate into standard model particles and vice-versa at equal rates, maintaining the balance between their relative densities. The WIMPs would then drop out of thermal equilibrium once the rate of reactions became less then the Hubble expansion rate H(t) at time t_f. This occurred when $N\langle\sigma v\rangle \leq H(t_f)$, where N is the number density of WIMPs, σ is the cross-section to co-annihilate to standard model (SM) particles, and v is the average WIMP velocity [19]. Freeze out occurs at temperature $T_F \simeq m_\chi/20$ (where m_χ is the WIMP mass) so WIMPs are already non-relativistic (or "cold") when they decouple from the thermal plasma of SM particles [17].

The supersymmetric neutralino is probably the most widely studied WIMP candidate. It is the lightest supersymmetric particle (LSP) in many models and consists of a superposition of the higgsino, bino and photino (super-partners of the higgs, $U(1)_Y$ gauge boson and the photon respectively) [4]. Its mass has been estimated to be 30 GeV $\leq M_\chi \leq$ several TeV, where the lower limit is from experiments at the LEP collider and the upper limit is set from theoretical concerns of the hierarchy problem which motivated SUSY in the first place. Supersymmetric theories also provide a new discrete symmetry called R-parity, defined as $R = (-1)^{3(B-L)+2S}$ where B is baryon number, L is lepton number, and S is spin. This gives $R = 1$ for SM particles and $R = -1$ for their superpartners. Conservation of R-party requires that the lightest SUSY particle (LSP) be stable and allows for relic neutralinos with the correct range of energy densities to match observations [4]. There are also a number of R-parity violating SUSY theories which could also provide useful WIMP candidates.

2.3 Dark Matter Distributions

Current direct and indirect searches for dark matter interactions with SM particles can only be made in the Milky Way. The rates of possible signals are correlated to the density distribution within the galaxy and a good model of this distribution would help to tailor the search. Unfortunately the rotation curve of the Milky Way is poorly constrained (due to our position inside the disk) which leads to large uncertainties on the total amount and distribution of local dark matter. Current rotation curve measurements constrain the local dark matter density, $\rho_0 \approx 0.3\ \frac{GeV}{cm^3}$, to a factor of 2. The velocity dispersion of local dark matter particles is believed to be of the order of the local velocity of the Sun orbiting within the galaxy $\bar{v} = \langle v^2 \rangle^{1/2} \approx 220\ \frac{km}{sec}$ [4]. Both factors are directly correlated to the expected rates for both direct and indirect searches.

The simplest model of a realistic dark matter distribution is the isothermal spherical halo model [4]. This gives a density profile of:

$$\rho(r) = \rho_0 \frac{r_C^2 + r_E^2}{r_C^2 + r^2}\,, \tag{2.1}$$

where r_C is the radius of a constant density core, $r_E = 8.5$ kpc is the distance from the galactic center to the Earth, ρ_0 is the mass density at Earth, and the corresponding velocity distribution, based on a Maxwellian, is given by:

$$f(v) d^3v = \frac{e^{-v^2/v_0^2}}{\pi^{3/2} v_0^3} d^3v\,. \tag{2.2}$$

In the velocity distribution v_0 is the orbital velocity in the flat part of the galactic rotation curve ($v_0 = 220$ km/sec for the Milky Way). This is a bit of a simplification since the phase-space distribution must obey Jean's equation, which strictly relates the velocity and acceleration components of a collisionless fluid to its gravity and pressure [20]. This implies that the velocity and density distributions can not actually be chosen independently. One can obtain exact solutions for the density distribution using numerical simulations which do not differ too much from Equation 2.1 [4]. It should be noted that one of the attractive features of this model, as opposed to one without a constant density core, is the lack of a singularity at the center of the galaxy.

In addition to the overall distribution of dark matter in the galaxy there are a number of theories which suggest structure on smaller scales. Models of cold dark matter halos have predicted large central cusps in which the density rises as $r^{-\gamma}$ toward the center of the galaxy. This could lead to enhanced co-annihilation products such as gamma-rays, though the lack of synchrotron radio emission from electrons due to neutralino co-annihilation around the presumed central black hole has lead some to claim that either the central cusp doesn't exist or that the dark matter is not neutralinos [21]. In addition to the central cusp many numerical models suggest smaller scale clumps of dark matter spread throughout the galaxy [22]. There are also recent numerical simulations which have suggested that Earth-mass dark-matter halos were some of the first structures to develop in the early universe [23]. Since the rate of WIMP co-annihilation goes as ρ^2 any variations in the density could significantly enhance the indirect signal. Direct searches, which detect nuclei recoiling from interacting with a dark matter particle, only scale linearly with local density. Their rates could still be affected by passing through a large dark matter clump, though, so local densities are still a factor.

For simplicity this analysis uses a smooth, cored-isothermal spherical halo model with a core radius of $r_c = 2.8$ kpc [4]. It should be noted that the relatively short path-length of electrons, ~ 3 kpc, (as discussed in §3.3) means that most smooth distributions (NFW, spherical Evans model, etc) look very similar in the range of electrons around the solar system. Any local variations (< 3 kpc) such as clumpiness would boost the signal and will be discussed more in the conclusions section.

2.4 WIMP Detection Methods and Limits

The three main avenues in the search for WIMP dark matter consist of looking for evidence of new particles in accelerator experiments, searches for rare direct interactions of relic WIMPs with standard model particles and searches for the co-annihilation products of relic WIMPs in the galaxy.

Since supersymmetry was first proposed as a theory searches for signs of its effects have been going on at accelerator experiments. These include direct searches for super-partner particles as well as for subtler effects on standard model predictions such as the anomalous magnetic moment of the muon, rare decays such as $b \to s\gamma$ and precise electroweak measurements [4]. It has been somewhat difficult to put stringent lower bounds on the mass of the neutralino from accelerator experiments due to the fact that one is looking for missing energy and momentum from the collision. SUSY also has a large number of new parameters leading to a very large parameter space in which the correct model might lie. The minimal supersymmetric standard model (MSSM) contains as few as possible additional variables while still providing a viable theory. One example of a limit for the lightest neutralinos (with a specific range of MSSM parameters) is given by the ALEPH collaboration at the LEP-II collider of ~ 37 GeV [24]. Of course, with the large set of possible parameters this measurement only really confines a certain set of models.

Since WIMPs are traveling in the halo at non-relativistic velocities they generally interact with regular nuclei via elastic scattering. As a result the interaction rate can be given by:

$$R = \frac{\rho}{M_\chi} \langle \sigma v \rangle \,, \tag{2.3}$$

where ρ is the WIMP mass density near Earth, M_χ is the WIMP mass, v is the WIMP velocity and σ is the cross-section for elastic scattering. The local mass density and velocity of the WIMPs are generally believed to be around 0.3 GeV/cm^3 and 220 km/sec (from galactic rotation curves) leaving their mass and cross-section as free parameters. The current range for the WIMP mass of 30 GeV to several TeV gives typical nuclear recoil energies of 1-100 keV. The cross-sections depend on the type of coupling which, for neutralino WIMPs, can be either scalar interactions (which couple to the nucleons' mass) or axial-vector interactions (which couple to the nucleons' spin). As a result there are searches using targets with high mass nucleons such as Ge or Xe or with large nuclear spin nucleons such as ^{19}F and ^{127}I [17]. All of these experiments require large target masses with very low backgrounds or large background discrimination or both. One possible signal arises if the solar system itself is moving relative to the stationary halo of WIMPs as it orbits the center of the galaxy. A signal would then be an annular modulation of a few percent in nuclear recoil rates as the Earth went around the Sun into and out of a galactic "wind" of WIMPs (relative to the solar system). The current best limits for neutralinos with scalar interactions come from the CDMS experiment (see Figure 2-2) [25]. There has been a reported detection of an annular modulation signal in the DAMA experiment, which uses NaI as a target [26], but this result is in conflict with the CDMS and EDELWEISS [27] experiments at the 99.8% CL [25].

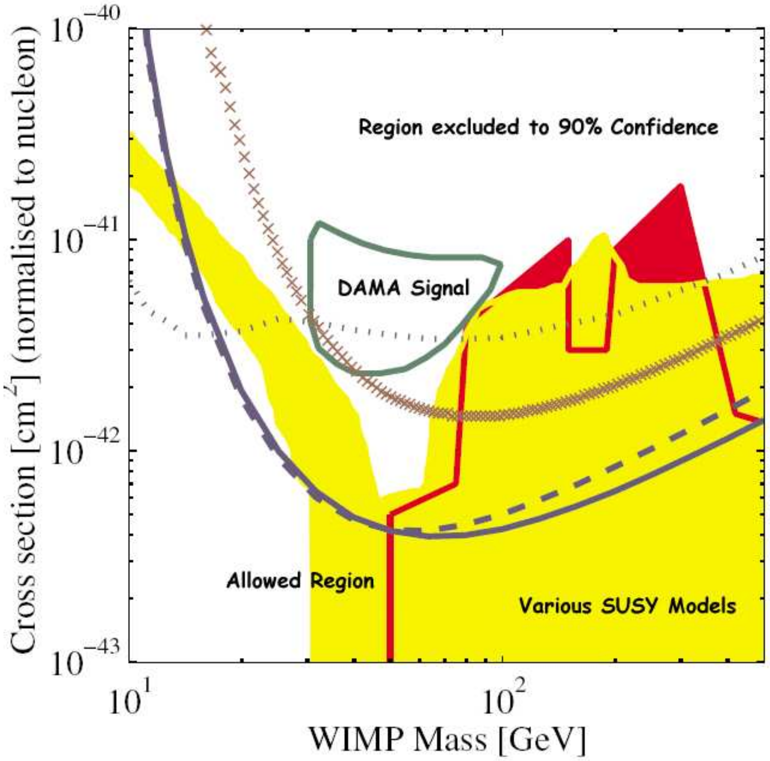

Figure 2-2: Limits on WIMP-nucleon scalar cross-sections from the CDMS II experiment [25]. Values in yellow (light gray) and red (dark gray) are various sets of SUSY models. The solid blue line is the CDMS II limit with no candidate, excluding all models in the region above it at the 90% CL. The dashed curve is the limit from a separate non-blind analysis of CDMS II with 1 candidate event. The brown curve (x-marks) is the EDELWEISS limit. The DAMA 3-σ signal is shown in the green closed area. The dotted line is the limit from CDMS run at the Stanford Underground Facility.

In addition to being able to scatter off nucleons, supersymmetric WIMPs can coannihilate with each other into standard model particles. If WIMPs can be captured over time via elastic scattering in the gravity wells of the Earth, Sun or galactic center, they can co-annihilate into high energy neutrinos and be detected by neutrino telescopes such as SuperK or AMANDA (which look for muons that have been converted from neutrinos as they come up through the Earth). Currently the best upper limit of $\simeq$ 3000 muons/km^2/year has been set by the MACRO experiment [28].

WIMP co-annihilation to gamma-rays in the halo of the galaxy can give both continuum and mono-energetic signals (from the $\gamma\gamma$ and $Z\gamma$ channels). These can be observed by satellite detectors and ground based air-Cerenkov telescopes (ATCs). The current best limits for dark matter produced gamma-rays below 10 GeV come from the EGRET telescope (part of the Compton Gamma Ray Observatory) and for gamma-rays above 100 GeV from the WHIPPLE telescope [29].

Recent results from the WHIPPLE, HESS and CANGAROO-II collaborations have implied an excess of TeV gamma-rays from the galactic core which could be due to heavy ($>$ TeV) dark matter [30].

WIMP co-annihilation in the halo can also release charged particles such as protons, antiprotons, electrons and positrons, which could propagate to Earth (see Figure 2-3). Most searches have looked for an excess in the antiparticle signals due to the lower intrinsic backgrounds. The BESS experiment has noted a small excess in the low energy antiproton spectrum but astrophysical uncertainties preclude any definite statements as to the source [31].

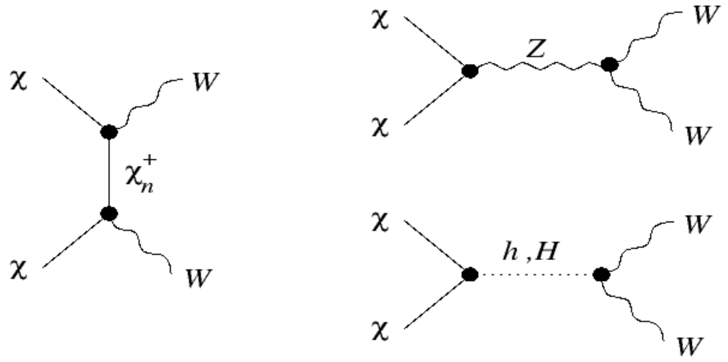

Figure 2-3: Possible neutralino co-annihilation channels to W$^+$W$^-$ bosons, which in turn will decay to stable particles (protons, electrons, positrons, neutrinos, etc). The left-hand diagram is mediated by a supersymmetric chargino (χ_n^+), the upper right-hand diagram is mediated by a Z boson and the lower right-hand diagram is mediated by Higgs bosons (h, H). Figure from [4].

The High Energy Antimatter (HEAT) series of balloon experiments have sent three different detectors into the upper atmosphere to measure the cosmic ray positron flux up to 50 GeV. At approximately 10 GeV and above these experiments have detected an excess in the positron fraction (positrons over positrons plus electrons) which is inconsistent with the assumption that that almost all positrons are produced from pions and kaons generated from cosmic-ray collisions on interstellar gas (see Figure 2-4) [8]. There has been speculation that this anomalous feature could be due to WIMP co-annihilation in the galactic halo though a significant increase in the co-annihilation rate would be required in order to fit the data. Clumped dark matter could significantly enhance the rate of dark matter co-annihilation but it is not clear from numerical simulations whether this would account for the large rise in positrons seen by HEAT. Others have suggested possible astrophysical sources of this positron excess, such as synchrotron produced $e^{\pm}$ pairs from pulsars in the galaxy [7]. This analysis will focus on the WIMP co-annihilation hypothesis. If one looks closely at Figure 2-4 one can see that the AMS-01 positron fraction measurement only extends to 3 GeV which is why the electron spectrum is used here instead. Since there are many primary and secondary sources of cosmic ray electrons their generation and propagation through the galaxy need to be modeled very carefully. This is covered in the next chapter.

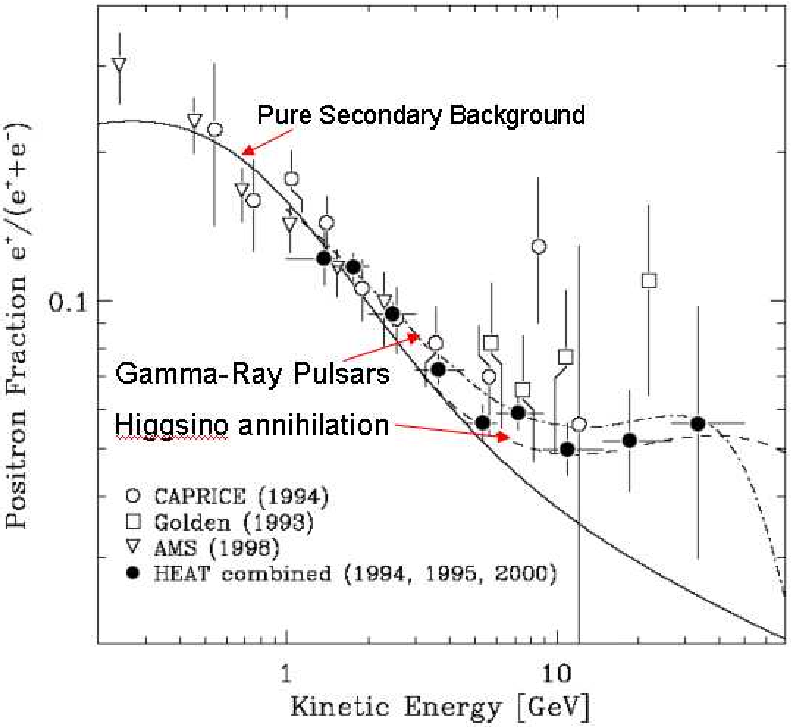

Figure 2-4: The positron fraction measured by HEAT and other experiments (from [8]). The downward slope on pure secondary background is due to the asymmetry in the decay of fully polarized muons created from pions and kaons which were in turn generated by proton/proton collisions in the interstellar medium.

Chapter 3

Cosmic Rays

The flux of charged cosmic radiation raining down on the Earth's atmosphere consists of 98% protons and nuclei, 2% electrons and less than a percent of antiparticles such as positrons and antiprotons [32]. They consist of primary particles generated from astrophysical sources as well as secondary particles that result from inelastic scattering of primaries (spallation) on interstellar material. The flux of cosmic rays from a few GeV to beyond 100 TeV is generally described by a power-law of the form $N(E) \propto E^{\gamma}$ where γ is the spectral index. The measured flux from cosmic nuclei is given by:

$$\Phi_N(E) \approx 1.8 \times 10^4 \; E^{-2.7} \frac{\text{nucleons}}{\text{m}^2 \text{ sec str GeV}} , \tag{3.1}$$

of which about 79% are free protons, 15% are helium nuclei and the remaining 6% are bound in heavier elements [33]. Cosmic electrons have a steeper spectrum given by:

$$\Phi_e(E) \approx 200 \; E^{-3.0} \frac{\text{electrons}}{\text{m}^2 \text{ sec str GeV}} , \tag{3.2}$$

as measured in [34]. These spectra are illustrated in Figures 3-1 and 3-2 [33, 35].

3.1 Standard Astrophysical Production/Acceleration

Primary cosmic rays have a variety of astrophysical sources. For energies below 10^{19} eV they are believed to be generated primarily within the galaxy and sources include supernovae, pulsars, stellar winds, etc. Local sources are required because, due to inverse-Compton scattering off CMB photons, high energy electrons have to be produced within 300 kpc in order to maintain the observed power-law distribution [41]. A typical Type II supernova will eject about 10 $M_{\odot}$ (where $M_{\odot} = 2.0 \times 10^{31} \; kg$) of material with velocities around 10% of the speed of light. With a galactic supernova occurring approximately once a century the average power output per galaxy of about 10^{42} J/yr. The total power required to accelerate cosmic rays to an average energy density of $\rho_E \approx 1$ eV/cm^3 is given by:

$$W_{CR} = \rho_E \pi R^2 \frac{D}{\tau} = 2 \times 10^{41} \; J/yr \, , \tag{3.3}$$

where $R \approx 15$ kpc and $D \approx 0.2$ kpc are the galactic radius and disk thickness, respectively, and $\tau \approx 3 \times 10^6$ years is the average age of cosmic rays in the galaxy (due to diffusion out of the galaxy and energy loss) [42]. As a result supernova remnants only need efficiencies of a few percent to account for the total energy in cosmic rays.

Exactly how supernovae accelerate particles to such large energies is not entirely understood. The general consensus is that the process is governed by Fermi acceleration, in which charged particles are up-scattered off moving magnetized clouds. Fermi's original idea [43] assumed that the particles randomly encountered these moving magnetic clouds as they propagated through the galaxy. This random up-scattering leads to a general acceleration rate proportional to the square of the scattering clouds velocity (second-order Fermi acceleration) [44]. Unfortunately, this process was quickly recognized to be too inefficient to account for the observed spectra [45]. In 1977, however, it was shown [46] that well defined shocks, such as those generated by magnetized supernova remnants expanding into the interstellar medium, could accelerate particles at a rate directly proportional to the velocity of the shock (first-order Fermi acceleration). Each time the particle up-scatters off the supernova shock it gains energy $\Delta E = \alpha E$, crosses the shock boundary, is reflected in the interstellar medium (with no energy lost) and then recrosses the shock boundary to repeat the cycle. After n cycles the total energy becomes $E = E_0(1+\alpha)^n$. If P is the probability that the particle stays at each cycle, the number of particles remaining after n cycles is $N = N_0\ P^n$, where N_0 is the initial number of particles. If one substitutes for n in the energy equation and takes the derivative with respect to energy one can obtain the observed power-law dependence:

$$\frac{dN(E)}{dE} \propto (\frac{1}{E^{(1+S)}})\,, \tag{3.4}$$

where $S = \frac{-ln(P)}{ln(1+\alpha)} \sim 1.1$ for standard shock wave acceleration giving a spectral index of $E^{-2.1}$ [42]. The observed value of the cosmic ray spectral index ($\gamma \approx$ -2.7) can be obtained by accounting for the energy dependence of the probability of a cosmic ray to escape the process.

Observations of secondary nuclei, such as beryllium and boron, which are generated from inelastic scattering of primary nuclei, such as carbon or nitrogen, off interstellar material, show that the ratio of secondary over primary particles decreases for increasing energy. This implies that the primary particles travel through less material and have a shorter circulation time as their energies increase. It also implies that the main acceleration points are separate from the propagation mechanics and, for the most part, one can treat them separately [41]. If the acceleration and propagation occurred together one would expect the ratio of secondary to primary nuclei to remain flat or even to increase with energy for processes that take a longer time to accelerate particles to high energies [47].

3.2 Co-annihilation of Neutralinos

Neutralino dark matter in the galactic halo is another possible source of primary electrons, positrons and other charged cosmic rays. For example, energetic electrons and positrons can be produced by the decay chain from $\chi + \chi \rightarrow$ ZZ, $\mathrm{W}^+\mathrm{W}^-$, etc (see Figure 2-3). It is these co-annihilation products, on top of the standard astrophysical backgrounds, that we will be searching for using AMS-01 data. Specifically we will be focusing on the $\mathrm{W}^+\mathrm{W}^-$ contributions to the electron and antiproton spectra.

The rate of neutralino co-annihilation can be calculated using:

$$R_{co-annihilation} = \frac{\rho^2}{M_\chi^2} \langle \sigma_a v \rangle \,, \tag{3.5}$$

where ρ is the mass density of WIMP particles, M_χ is the mass of one WIMP particle, σ_a is the cross-section for co-annihilation and v is the average WIMP galactic velocities (assumed to be $v = 220$ km/sec) [4].

A broad continuum of electrons and positrons occurs through the fragmentation and decay of heavier co-annihilation products which would be difficult to distinguish from the expected astrophysical backgrounds. WIMPs can co-annihilate directly to electrons and positrons leading to a primary spectrum consisting of a peak at the energy of the WIMP mass. Even though propagation effects would spread out such a peak it would be much easier to detect then the continuum emission.

Unfortunately, most leading WIMP candidates (such as the neutralino) are Majorana particles, implying they are their own antiparticles. In this case two neutralinos in a relative s-wave must have opposite spin by Fermi statistics (spin-$\frac{1}{2}$ fermions) and any co-annihilation to a standard model fermion pair requires them to have spins in opposite directions. As a result the final state fermions will have their spins in opposite directions which forces the amplitude for the process to carry an extra factor of the fermions mass (m_f). As a result the cross-section for this process is suppressed by a factor of m_f^2/m_χ^2, where m_χ is the WIMP mass [4]. Alternatively, if the WIMPs are heavier then the $\mathrm{W}^\pm$ or Z bosons they can co-annihilate into monoenergetic $\mathrm{W}^+\mathrm{W}^-$ or ZZ pairs, which could then directly decay into electrons/positrons with energies peaked around half the WIMP mass [9]. Since the $\mathrm{W}^+\mathrm{W}^-$ or ZZ co-annihilation channels are not suppressed this analysis will concentrate on searching for their decay signatures in the AMS-01 electron data, specifically focusing on the $\mathrm{W}^+\mathrm{W}^-$ states.

3.3 Galactic Propagation

Once energetic cosmic rays are created (by astrophysical processes or by dark matter co-annihilation) they propagate through the galaxy, spiraling around the turbulent magnetic fields, flying through clouds of gas and dust and scattering off photons from starlight and the CMB. In addition, cosmic rays are continually escaping the galaxy with rates that increase with particle energy. The galactic magnetic fields are of order a few μGauss which gives a Larmor radius of approximately $1 - 100$ AU for cosmic rays of energies 1-100 GeV [48]. Cosmic rays will spiral tightly around magnetic field lines until the lines become tangled or kinked in which case the particle may jump to a different field line. As a result this process can best be modeled by diffusion.

From the ratio of spallation products, such as Be and B, to primary stellar nuclei, such as C and N, one can infer that cosmic ray nuclei must traverse an average of 5-10 grams/cm^2 of interstellar material. Integrating along the line of sight in the galaxy results in approximately 10^{-3} grams/cm^2 of material implying a long propagation time in which the particles are diffusing out from their primary sources [41]. One can also compare the ratios of radioactive secondaries, such as ^{10}Be, to their stable counterparts (in this case ^{9}Be) in order to infer the average lifetime of cosmic ray nuclei. Measurements of these ratios suggest that typical escape times for high energy cosmic ray nuclei are about $(1 - 3) \times 10^7$ years [49] in the energy range of interest.

Energy losses for cosmic ray nuclei are primarily from ionization and Coulomb interactions while electrons/positrons have additional bremsstrahlung, inverse-Compton scattering and synchrotron losses. The latter two dominate for electrons/positrons with energies greater then a few GeV leading to steeper power-law spectra compared to nuclei (spectral index of $\gamma_e \approx -3.0$ as opposed to $\gamma_n \approx -2.7$ for nuclei) [32].

This analysis uses a diffusion model of the galaxy with a set of boundaries. It assumes that particles diffuse through the main disk of the galaxy but escape once they reach an edge (in radius or distance from the plane of the disk) where it is believed that the confining magnetic fields of the galaxy become negligible. One can model the propagation within the galactic disk using the following equation:

$$\begin{aligned}\frac{\partial \psi}{\partial t} &= q(\vec{r},p) + \vec{\nabla}\cdot(D_{xx}\vec{\nabla}\psi - \vec{V}\psi) + \frac{\partial}{\partial p}p^2 D_{pp}\frac{\partial}{\partial p}\frac{1}{p^2}\psi \\ &\quad - \frac{\partial}{\partial p}[\dot{p}\psi - \frac{p}{3}(\vec{\nabla}\cdot\vec{V})\psi] - \frac{1}{\tau_f}\psi - \frac{1}{\tau_r}\psi\,, \end{aligned} \tag{3.6}$$

where $\psi = \psi(\vec{r}, p, t)$ is the density per unit of total particle momentum. The first term on the right-hand side, $q(\vec{r}, p)$, is the source term which describes the cosmic ray injection spectrum throughout the galaxy. The second term describes spatial motion and includes diffusion, where D_{xx} is the spatial diffusion coefficient, and convection, where $\vec{V}$ is the velocity of bulk charged particle motion. The spatial diffusion occurs mostly along the magnetic field lines and the diffusion coefficient is defined as $D_{xx} = \beta D_0(\rho/\rho_0)^\delta$ where $\beta = v/c$, ρ is the particles rigidity (momentum over charge), and D_0, ρ_0, and δ are all constants chosen to match cosmic ray Boron/Carbon ratios (see Sec. 2 of [50] for more details). The third term describes diffusive re-acceleration. Using the three-dimensional phase-space density $f(\vec{p})$, the diffusive re-acceleration is given by the following equation [50]:

$$\frac{\partial f(\vec{p})}{\partial t} = \vec{\nabla}_p\cdot[D_{pp}\vec{\nabla}_p f(\vec{p})] = \frac{1}{p^2}\frac{\partial}{\partial p}[p^2 D_{pp}\frac{\partial f(p)}{\partial p}]\,, \tag{3.7}$$

where, by assuming an isotropic distribution, $f(\vec{p}) = f(p)$ (p = $|\vec{p}|$). This equation can be re-written in terms of the density per unit of total particle momentum, $\psi(p)$, by using its relation to the phase-space density, $\psi(p) = 4\pi p^2 f(p)$, resulting in the following equation [50]:

$$\frac{\partial \psi}{\partial t} = \frac{\partial}{\partial p}(p^2 D_{pp} \frac{\partial}{\partial p} \frac{\psi}{p^2}) . \tag{3.8}$$

D_{pp} is the momentum space diffusion coefficient to give re-acceleration and is related to the spatial diffusion coefficient, $D_{pp} \propto p^2/D_{xx}$, where p is momentum (see equation 1 of [50] and Appendix D for more details). Momentum loss from ionization, Coulomb interactions, bremsstrahlung, inverse-Compton scattering and synchrotron radiation is covered by $\dot{p} > 0$. The final two terms of Equation 3.6 are τ_f, the fragmentation time scale, and τ_r, the radioactive decay time scale. The propagation equation lends itself to numerical simulations such as GALPROP [11], the results of which will be discussed in §5.3.5.

3.4 Solar Modulation and Geomagnetic Effects

Once the particles propagate through the galaxy and reach the vicinity of the solar system they must diffuse through the outflowing solar wind before they can reach Earth. The solar wind consists of a large flux of low energy protons traveling at around 350 km/sec away from the sun. This highly conductive plasma carries the Sun's magnetic field along with it and modulates the interstellar cosmic ray spectra below $\sim$ 10 GeV [32]. The solar wind strength varies with the 11-year solar cycle which gives an additional time dependence for cosmic ray fluxes with energy $E \leq 10$ GeV. This analysis focuses on the cosmic ray spectra above 10 GeV where solar effects are negligible.

When the cosmic rays finally reach Earth they must penetrate its dipole magnetic field before they can reach the AMS-01 detector in low Earth orbit (see Figure 3-3 for example trajectories with the Super-K detector). This field provides a directionally-dependent cutoff for primary particles given by the equation:

$$\frac{p}{|z|} = \frac{59.6[GeV/c^2] \cos^4 \lambda}{(1 + (1 - Q \sin\theta \cos^3 \lambda)^{1/2})^2} , \tag{3.9}$$

where p is momentum, z is charge, Q is charge sign, λ is the geomagnetic latitude and θ is the angle which gives the particles incoming direction with respect to the horizon ($\theta = 90^\circ$ are particles incident from the east and $\theta = -90^\circ$ are particles incident from the west) [51]. Particles above this cutoff momentum can be easily traced back into interstellar space where as particles below this cutoff require complicated numerical routines to determine if they originated from interstellar space or from the earth's atmosphere. These latter low energy secondary particles (not to be confused with "secondaries" from inelastic collisions) no longer represent the primary spectra of cosmic-rays and need to be removed from the AMS-01 data sample. This process will be outlined in greater detail in §5.2.4. To give an example a proton traveling along the magnetic equator (λ = 0) from the east needs to have a momentum greater than 59.6 GeV or its origin could be the earth's atmosphere. It it was coming from the west it would only require a momentum of 10.2 GeV (see Figure 3-3).

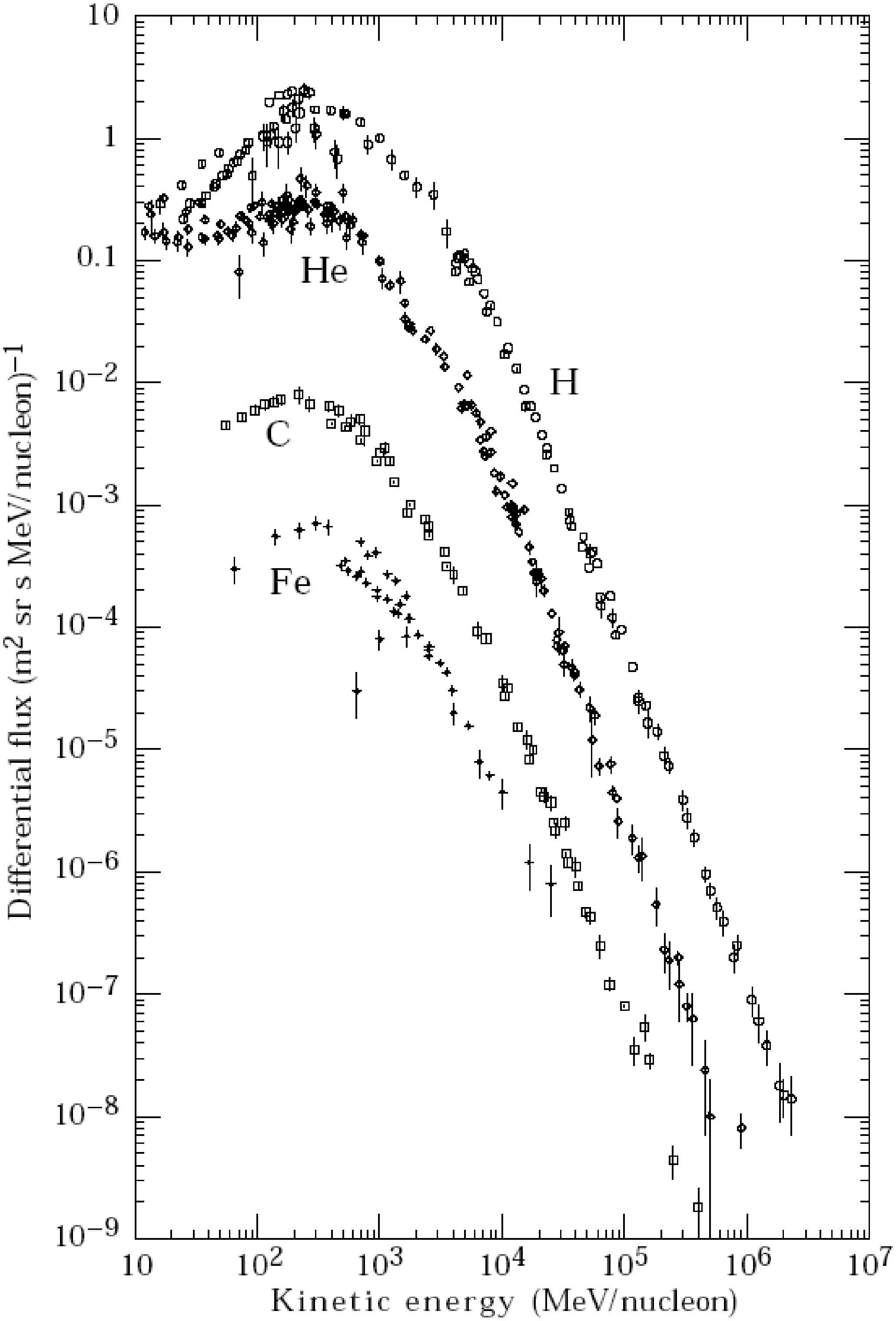

Figure 3-1: Primary cosmic ray nuclei spectrum. 79% of total nuclei come in the form of protons, 15% are bound in helium nuclei and the remaining 6% exist in heavier elements. Figure from [33].

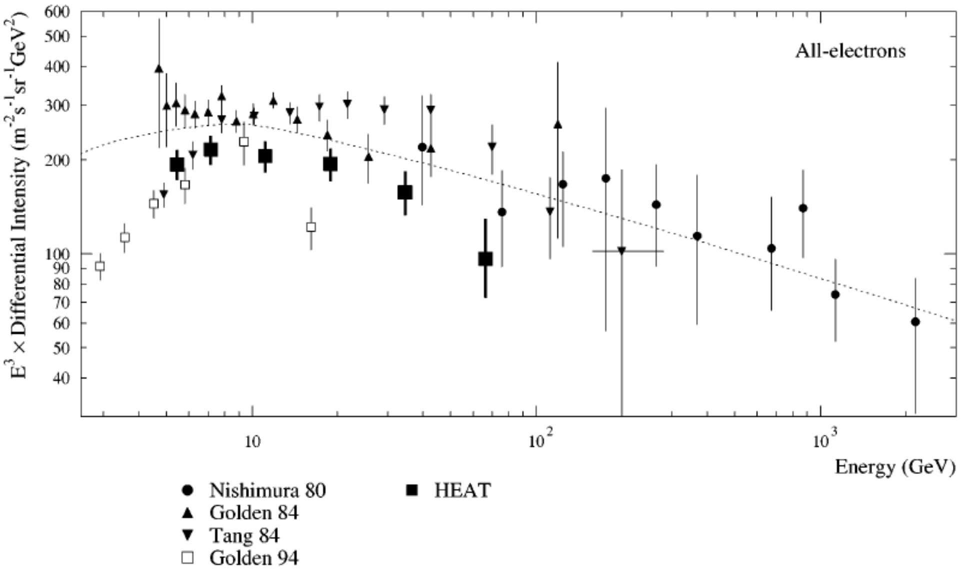

Figure 3-2: Spectrum of electrons + positrons multiplied by E^3. The data is from a number of sources including Nishimura 80 [36], Golden 84 [37], Tang 84 [38], Golden 94 [39], and HEAT [35]. The dotted line is a parametrization from Moskalenko and Strong 98 [40]. Figure from [35].

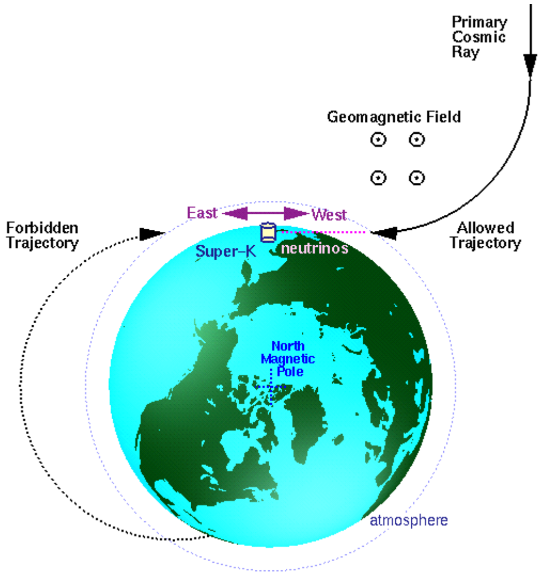

Figure 3-3: Allowed trajectory of a primary cosmic ray from interstellar space and a corresponding forbidden trajectory. Particles which follow the latter are known as secondary particles and could come from interactions in the Earth's atmosphere. Figure from Super-K [52].

Chapter 4

The AMS-01 Detector and Mission

The AMS-01 experiment flew on the Space Shuttle flight STS-91 from June 2-12, 1998 and gathered over 100 million cosmic ray events (mostly protons). This chapter summarizes the AMS-01 hardware, flight details and event reconstruction as described in a variety of references, such as [53, 54, 48].

4.1 The AMS-01 Detector

The AMS-01 detector was designed to make precision measurements of charged cosmic rays from several hundred MeV to almost 300 GeV and required a large number of complementary detector elements. This section will focus on describing the detector layout which consisted of a permanent dipole magnet, silicon tracker, time-of-flight counters (TOF), threshold Cerenkov counters (ATC), and anti-coincidence counters (ACC). The assembled detector can be viewed in Figure 4-1 and the initial results are published in Physics Reports [53].

4.1.1 The Magnet

The AMS-01 magnet was designed to optimize the competing requirements of a large, powerful, uniform dipole magnetic field in a flight-qualified, relatively lightweight system. The external field also needed to be minimized to reduce torques on the space shuttle and interference with electronics. The magnet was made of 6400 2” × 2” × 1” blocks of high grade Nd-Fe-B. The blocks were arranged in a cylinder of length 800 mm, inner diameter 1115 mm and outer diameter 1299 mm. The blocks were arranged into 64 segments with varying field directions to produce a uniform 0.15 T field inside the magnet with a negligible external field (see Figure 4-2 [53]). After construction the field was mapped and found to agree with the design value to 1%. The final magnet weighed 2.2 tons including support structure and had a maximum bending power of $BL^2 = 0.15$ Tm^2. Details of the magnet design can be found in [55].

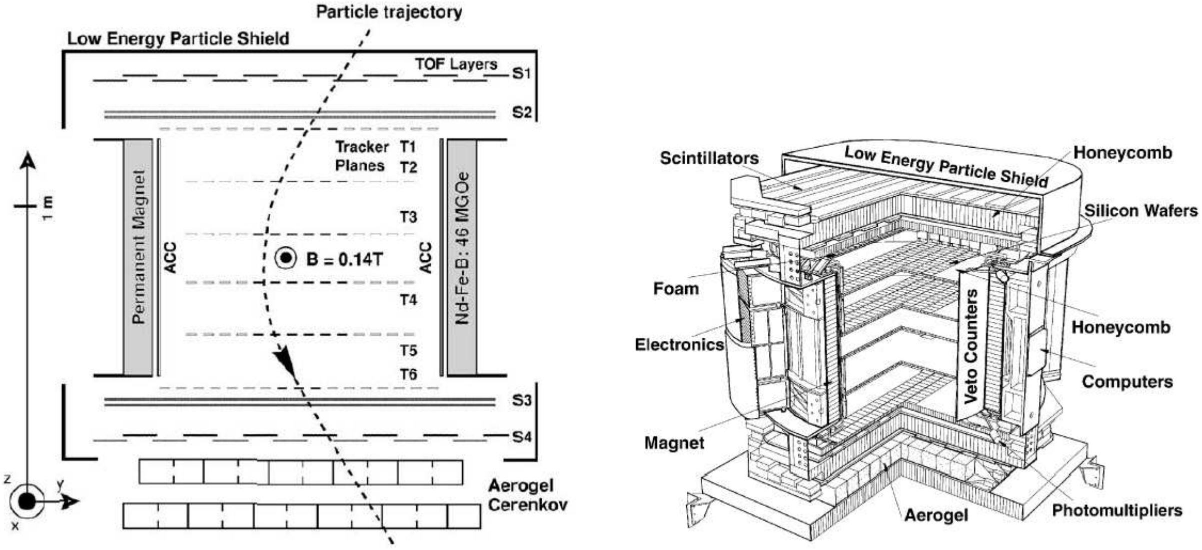

Figure 4-1: AMS-01 Integrated Detector layout [53].

4.1.2 The Silicon Tracker

The silicon tracker was located in the magnet cylinder to precisely measure the charged particle's curved track in the B-field and thereby determine its rigidity (defined as the magnitude of the particles momentum over its charge $\mathrm{R} = |\vec{\mathrm{p}}|/\mathrm{Z}$). Measurements of the particle's energy deposition in the silicon from ionization allowed one to determine the charge of the particle which, when combined with the particle rigidity, determined the momentum. Additional charge measurements were also made by the TOF. The AMS-01 silicon tracker was composed of 6 layers of double-sided microstrip sensors. The tracker provided a position resolution of 10 μm in the bending plane (S-side) and 30 μm in the non-bending plane (K-side) which translated to a momentum resolution of 7% for protons in the 1-10 GeV range. This position resolution, combined with the 0.15 Tesla magnetic field, gave the experiment a maximum detectable rigidity of approximately 360 GV.

The sensors consisted of between 7 and 15 silicon chips chained together to form ladders which ran in the AMS-01 x-direction, parallel to the B-field (see Figure 4-3 [53]). The sensors were read-out with metalized kapton foils of which the K-side had a chained scheme which created an x-position ambiguity (the solution of which is explained in §4.3.2). At readout a "seed strip" was chosen where the signal was $> 3\sigma_{ped}$, with σ_{ped} defined as the strips pedestal width [53]. Signals from individual tracker strips were grouped into clusters by taking up to 2 additional strips on either side of this primary "seed strip" [56]. This was performed separately for the S-side and K-side. Additional details can be found in §4.3.2. Each of the chip's 3D position was determined by laser-metrology and beam-tests to within $10\mu m$. The average material thickness of each

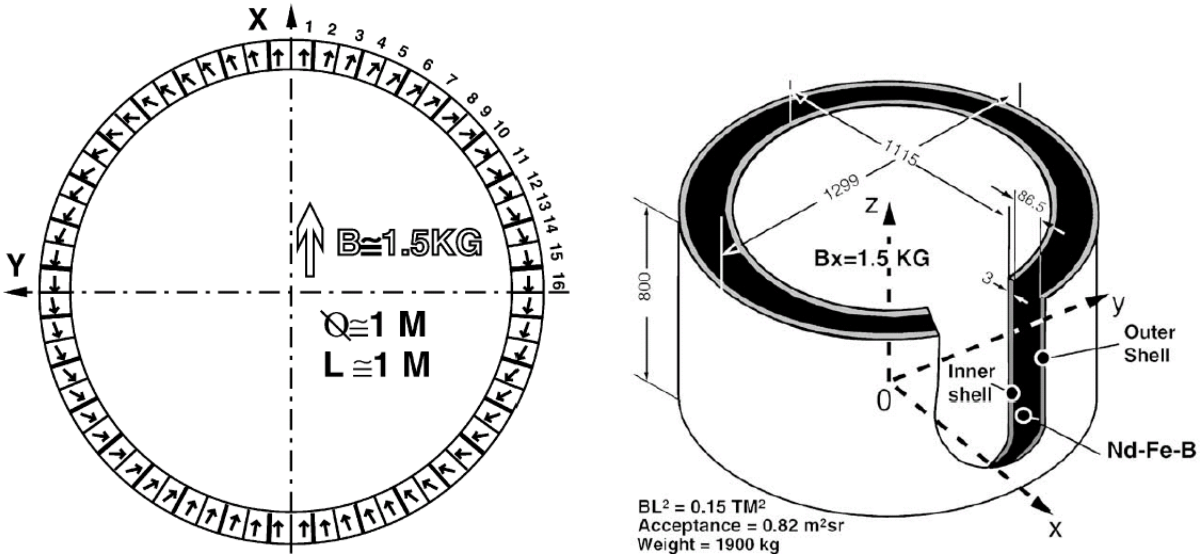

Figure 4-2: AMS-01 Magnet field orientation and dimensions [53]. The varying direction of the magnetic field in the material allowed the flux to be returned primarily within the material allowing for a negligible external field.

tracker plane, including support ladders, was 0.65% of a radiation length at normal incidence [53]. For AMS-01 only 38% of the tracker was instrumented which led to an acceptance of 0.31 m^2-str for events that passed through at least 4 of the 6 planes. Additional details of the AMS tracker construction and performance are given in [57].

4.1.3 The Time-of-Flight (TOF)

The time of flight system had a number of uses including charge measurement, velocity measurement and trigger for the data acquisition. It consisted of 4 layers of 14 scintillator paddles of various lengths with 2 layers above the tracker and 2 below the tracker as illustrated in Figure 4-4 [53]. The paddles were 10 mm thick and 110 mm wide and ranged from 720-1360 mm in length. Adjacent paddles had a 5 mm overlap in order to avoid missing events close to the edges. Layers 1 and 4 were positioned with the paddles along the x-direction while layers 2 and 3 were positioned in the y-direction. Each paddle had 3 photomultiplier tubes (PMTs) attached at each end with a 50 mm long light guide. The signals from the 3 PMTs are summed to give one signal from the anode and one from the 2nd to last dynode [53]. The outputs at each end included the following signals:

- A trigger signal (above a 150 mV threshold) which was sent to the general trigger system;
- A high precision time measurement of the delay between the input anode signal

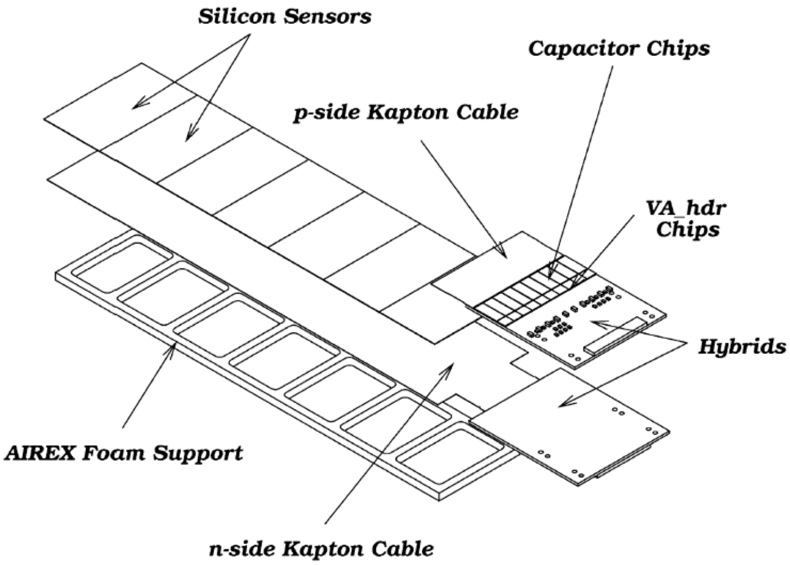

Figure 4-3: A single Tracker ladder [53].

(above 30 mV) and the trigger signal from the general trigger;

- The integrated anode signal;
- The integrated dynode signal;
- A time over threshold signal to give an estimate of the signal time. This is used to tag off-time particles up to 10 μsec before and 6.5 μsec after the event.

From test beam measurements at either end of the TOF the time and position resolution was determined to be 115-125 ps and 14.5-18.5 mm, respectively, depending on the counter length. Charge measurement using the time over threshold allowed for good separation of Z = $|1|$ and Z = $|2|$ particles (to the level of $\approx 5 \times 10^{-3}$) but had poor charge resolution for $|Z| > 1$ [58]. TOF clusters, defined as signals from 1 or 2 adjacent TOF paddles, were also used to trigger the detector [54]. The saturation limit of the readout electronics was 20 kHz [53]. In addition, due to the high time resolution the probability of mistaking a particle's upward or downward direction, and hence its charge sign, is a negligible 10^{-11}. Further details on the TOF can be found in [58].

4.1.4 The Aerogel Threshold Cerenkov Counter (ATC)

The ATC was built of blocks of aerogel with attached lightguides and PMTs to pick up Cerenkov light of high velocity charged particles and allow for particle identification beyond the TOF range. The detector consisted of 168 of these blocks (see Figure 4-5 [59]) arranged in 2 layers, 8×10 in the upper layer and 8×11 in the lower layer. Each cell had eight 11 mm thick aerogel blocks with index of refraction $n = 1.035 \pm 0.001$

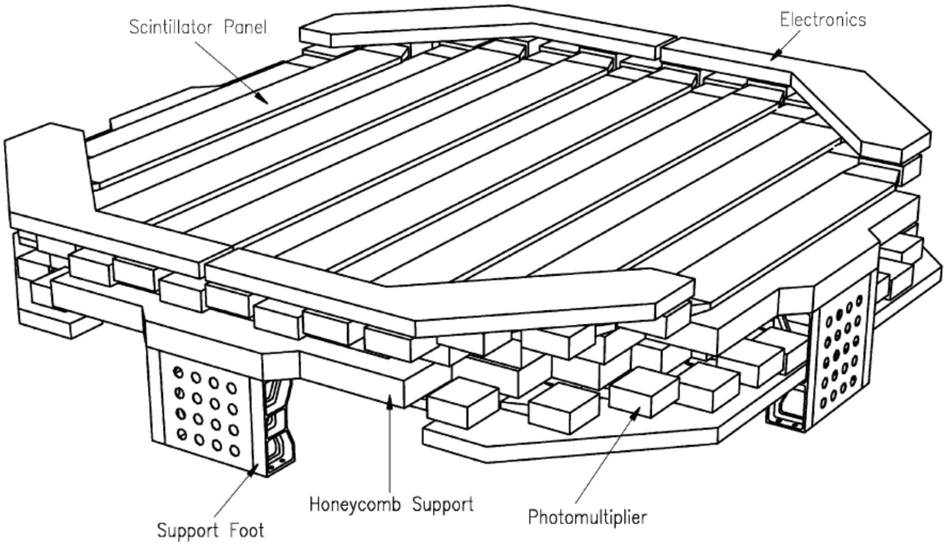

Figure 4-4: The two upper TOF planes [53].

surrounded by 3 reflective teflon layers. A wavelength shifter was located between the 4th and 5th aerogel layer and lowered Cerenkov photon loss up to 40% by absorbing the Cerenkov light ($\lambda = 300$ nm) and re-emitting it with wavelength 420 nm [59]. This lowered scattering losses and shifted the wavelength to the range in which the PMTs have maximum efficiency. The primary goal of this subdetector was the separation of $\bar{p}/e^-$ and p/e^+ up to approximately 3.5 GeV. At higher energies it loses much of its utility and subsequently was not used in this analysis.

4.1.5 The Anti-Coincidence Counter (ACC)

The ACC was made of 16 scintillation paddles, each 1 cm thick, arranged in a cylinder between the magnet bore and the support shell for the tracker. They were the primary veto for events which either passed through the sides of the detector, had large scattering angles or generated a large number of secondaries. If an event had a signal in any part of the ACC above a threshold of 0.15 MeV it was rejected by the Level 1 trigger [56].

4.2 The Flight

The AMS-01 flight on the Space Shuttle *Discovery* took place from June 2 to June 12, 1998. Figure 4-6 [54] illustrates the location of AMS-01 in the aft of the Shuttle bay which remained fixed for the duration of the mission. The Shuttle, however, pointed in various directions with respect to zenith (defined as the line pointing from the center of the Earth through the shuttle into space) throughout the flight. This angle between the AMS-01 z-axis and the local zenith direction will hereafter be referred to as the *zenith angle*. This was the last mission to the *MIR* space station and, as a result, the

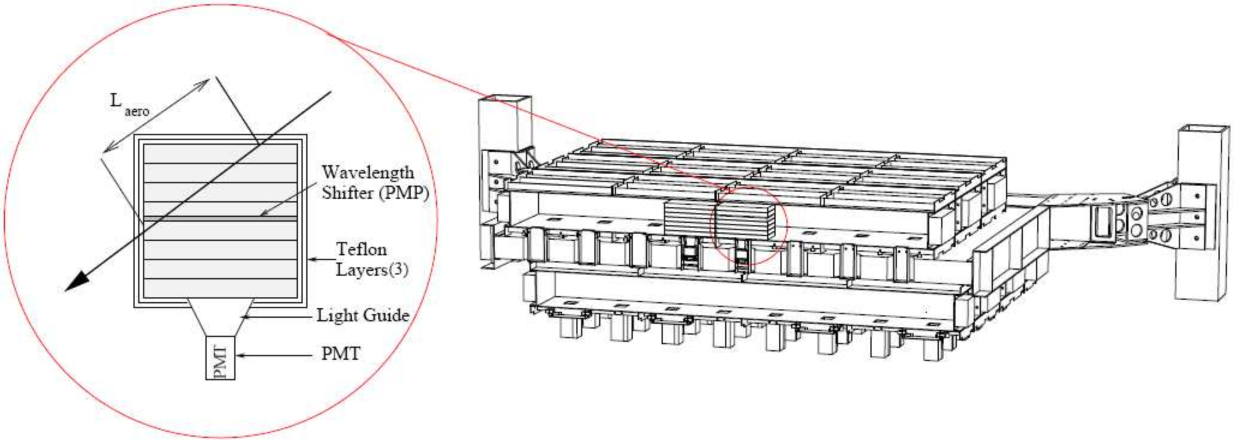

Figure 4-5: The ATC module [59].

shuttle was attached to the station for approximately 4 days. During this time the shuttle orientation with respect to zenith varied between 40 degrees and 140 degrees. In addition, while attached to *MIR*, part of the field of view of the detector was obscured by the station itself leading to a significant increase in spallation products impinging on the detector. As a result the time in which the shuttle was docked with the station will not be used in the analysis.

AMS-01 data was originally going to be downlinked continuously during the mission but a malfunction with the Ku-band antenna required that the data be stored on disks (which were recovered after landing) while a small subset of data was sent down a slower downlink to monitor the detector.

4.2.1 Flight Parameters

The orbital inclination of the flight was 51.7 degrees with an altitude that varied between 320-390 km and had an orbital period of roughly 93 minutes. Data taking began on June 3rd and was collected in 4 distinct periods (see Figure 4-7):

1. During the 25 hours before docking with *MIR* the shuttle was oriented with a zenith angle of 45 degrees.

2. The four days in which shuttle was docked with *MIR* resulted in large variations in zenith angle. Data during this time was excluded due to the increase in $\pi^{\pm}$ and $\mu^{\pm}$ generated from interactions of the cosmic rays with the *MIR* material in the field of view of the detector [54].

3. After separating from *MIR* the shuttle was positioned with zenith angle pointed 0 degrees, 20 degrees, 45 degrees for 19, 25, and 20 hours respectively.

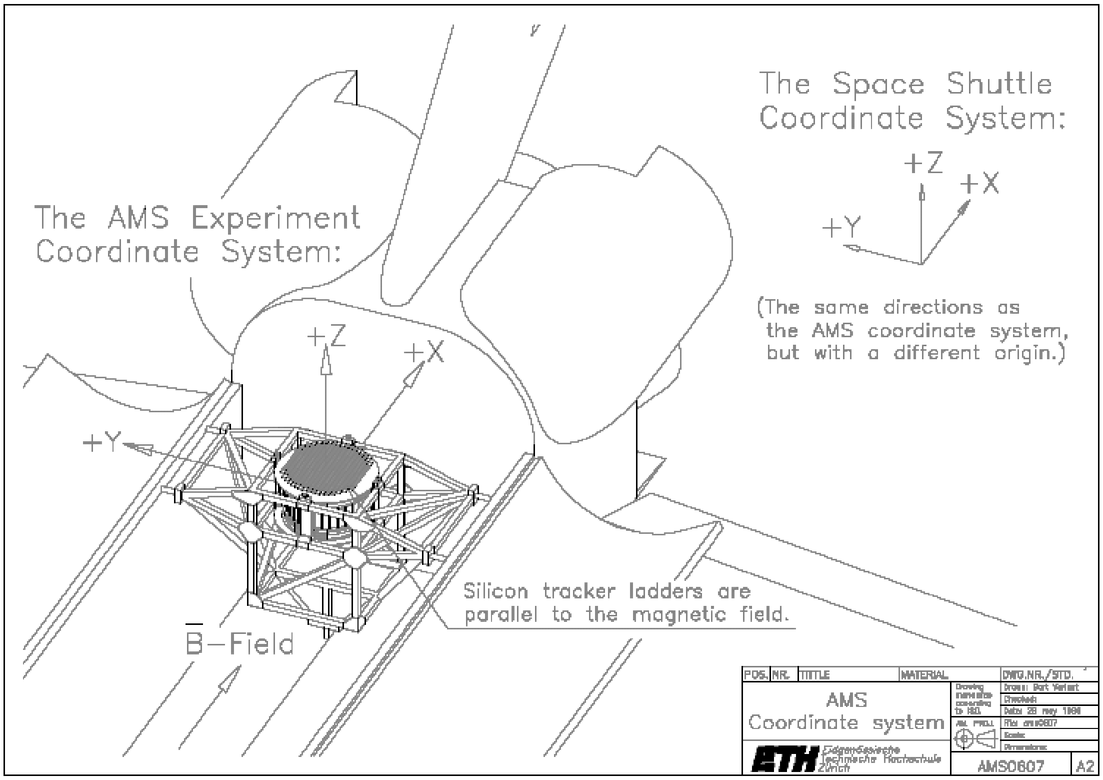

Figure 4-6: AMS orientation in Shuttle Bay (from [54]).

4. Before descending the shuttle was flipped over with AMS pointing toward Earth (zenith angle = 180 degrees) for 9 hours to study the effects of particles interacting with the shuttle bottom. Data for this period was not included in our analysis.

4.2.2 Trigger and Livetime

For an AMS-01 event to be recorded it needed to pass 3 different trigger levels: Fast, Level 1, and Level 3. There was no Level 2 trigger.

1. **Fast Trigger:** This was the initial hardware trigger for the rest of the electronics. It was initiated when each of the 4 TOF planes had at least one end of a member paddle's PMTs rise above a specific voltage threshold. All 4 TOF planes were required to coincide within 200 μs of each other for the trigger to be issued.

2. **Level-1 Trigger (Matrix):** This software trigger was implemented because the TOF acceptance was much larger then the partially instrumented Tracker. A correlation matrix between the outer 2 TOF paddles was used to reject triggers which did not pass through at least 4 tracker planes.

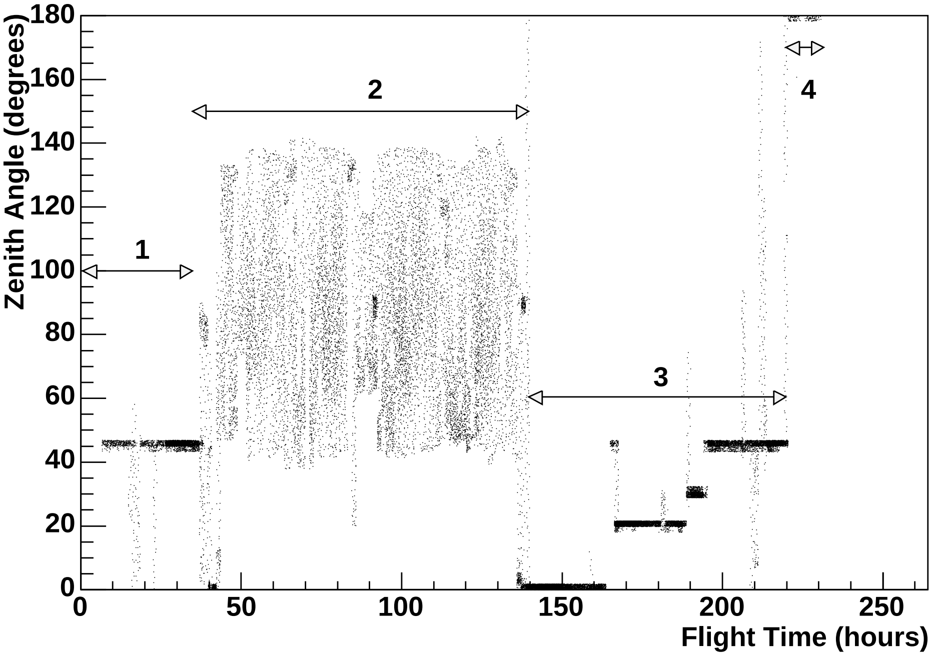

Figure 4-7: AMS-01 zenith angle as a function of time with the various time periods indicated. The data from the time in which *Discovery* was docked with the *MIR* space station (period 2) and when AMS-01 faced Earth (period 4) was not used in this analysis.

3. **Level-1 Trigger (Veto):** In addition all events which left any signal in the ACC were rejected. This cut inelastic scattering events, large scattered events, or events in which a particle was also passing through the sides of AMS.
4. **Level-3 Trigger (TOF):** Initially signals at both ends of a TOF cluster were required for planes 1 and 4 but, after it was discovered that plane 4 was delivering less information, this requirement was only applied to plane 1 [54].
5. **Level-3 Trigger (Tracker):** A fiducial road 6.2 cm wide was generated in the tracker bending plane from the clusters registered in the TOF. Track clusters (groups of up to 5 adjacent tracker strips) were then selected if at least one strip had a signal to noise ratio > 4. The trigger then required at least 3 clusters in 3 different tracker planes within this fiducial road.

It should be noted that an additional Level-3 trigger requirement using the residuals to a straight line fit of the tracker hits was used prior to the docking with *MIR*. Due to lower than anticipated trigger rates this requirement was disabled when *Discovery* docked with *MIR* [54].

To study the trigger efficiencies about 0.1% of the total triggered events was recorded with only the Fast trigger requirement [60]. These “prescaled” events were used to determine corrections to the detector acceptance to be discussed in §5.3.2.

The overall geometric acceptance after these trigger requirements was 0.42 m^2-str. The trigger rate usually varied between 100 and 1600 Hz as a function of position relative to the magnetic poles, though it sometimes spiked to almost 20 kHz within the South Atlantic Anomaly[1] [53]. The readout time was approximately $85\mu s$ which resulted in up to 13% losses at the highest trigger rates (near the poles). This deadtime was accounted for in the calculation of the detector livetime, defined as the percent of time in which the detector was ready to capture an event. This livetime was calculated directly from the Data Acquisition System (DAQ) every few seconds. There were some time (less than 10%) in which the transmission was lost or no livetime was calculated and some of these gaps were filled in by interpolating the livetime offline [61]. Accounting for this livetime will be discussed further in Chapter 5. As trigger rates saturated when the detector was in the South Atlantic Anomaly data from this area was excluded [53]. Events which pass all trigger requirements are subsequently recorded for future analysis. Further information on the AMS-01 trigger can be found in [62].

4.3 Event Reconstruction

This analysis will use the TOF and tracker to fully characterize each event. The velocity, β, and direction of the particles are measured using the TOF. The charge is determined from the energy loss in both the tracker silicon and the TOF scintillators. The particle's rigidity, R, is determined from the curvature in the magnetic field as determined by the tracker. These individual measurements combine to yield the mass, charge sign, charge magnitude and incident momentum vector of the particle.

4.3.1 Velocity Measurements

The velocity was determined by fitting time measurements of the TOF clusters near to the reconstructed track. A mean time (t_m) is calculated for each TOF cluster from the time measurements at each end of the paddles (t_1 and t_2) relative to the AMS-01 general trigger:

$$t_m = \frac{t_1 + t_2}{2}\,. \tag{4.1}$$

Additionally a differential time (t_d) allowed for the position along each paddle to be determined using the known effective speed of light in the scintillator:

$$t_d = \frac{t_1 - t_2}{2}\,. \tag{4.2}$$

The time measurements were corrected for time-walk or "slewing" which resulted from the fact that large signals reach the signal threshold faster than smaller signals. This

---

[1] The South Atlantic Anomaly is a region just southeast of Brazil in which the inner Van Allen radiation Belt comes closest to the Earth's surface. It is due to the Earth's dipole being offset from the center of the Earth [60].

causes an additional asymmetric term in the time resolution which can be partially corrected for in the following equation:

$$t_{corr} = t - \frac{k}{\sqrt{a}}\,, \tag{4.3}$$

where a is the integrated anode signal and k $\approx$ 7.5 ns $\sqrt{\text{pC}}$ for all counters [63].

To determine the velocity, β, a linear χ^2 fit was performed where:

$$\chi^2_{TOF} = \sum_i \frac{(t^1_m - \beta^{-1}\frac{d^i}{c} - K)^2}{(\Delta t^i_m)^2 v}\,. \tag{4.4}$$

The various terms for each layer (i=1-4) include the mean time, t^i_m, track length at the crossing point of the paddle, d^i, speed of light, c, unused offset, K, estimated error in the mean time, Δt^i_m and factor of $v = 1$ or $v = 2$ if 3 or 4 TOF layers are used, respectively [54].

A corrected β_C was also calculated to account for the fact that particles are bounded by the speed of light [56].

4.3.2 Track Reconstruction

The reconstruction of a track from the silicon tracker started with the selection of clusters (as defined in §4.1.2). The actual position of each cluster was calculated by fitting a gaussian to the signal amplitudes of the clusters individual strips. K (non-bending) side clusters required a S/N of 2.75 in the seed strip (as opposed to a S/N of 3.5 in the S-sides [56]) and only the adjacent strips to create a cluster. The K-side's 6 to 8 fold degeneracy (resulting from the common readout strips) could be somewhat resolved by comparing clusters in the inner and outer tracker layers which were slightly offset, and by using the rough track defined by the TOF clusters [56].

Once a set of S and K-side clusters were defined they were combined to make 3-D "hits". A track finding procedure then fit a straight line to all the hit combinations in separate planes (with at least 4 hits used). If the χ^2 was low enough a helix fit was performed, assuming a constant B-field. If the results for the helix fit were good enough more sophisticated fits were performed including:

- **Fast Fit:** Algorithm based on a 5×5 matrix inversion [64];
- **GEANE Fit:** Fit based on Kalman filter using the GEANE CERN library [65].

These fitting procedures returned a particle rigidity, rigidity error and a χ^2. The fit with the best overall quality (low χ^2, large number of hits, etc) was set as the correct track for the candidate particle [48].

4.3.3 Charge Measurements

The amount of energy loss of a particle passing through a material is proportional to the square of the particle's charge (Z^2) and, for the energy regimes relevant for this analysis, the natural log of the velocity multiplied by the relativistic γ ($ln(\beta\gamma)$) [66]. The charge of each particle was determined using a likelihood method based on predefined samples of energy deposition for the TOF and the tracker (after velocity and angle corrections). For charges up to $|Z| = 3$ the TOF and tracker information were combined while for $|Z| > 3$ just the tracker was used [56], however tracks with $|Z| > 1$ were not used in this analysis. The probability for a helium atom to be reconstructed with charge $|Z|=1$ is estimated to be less than 10^{-7} [53].

Chapter 5

Data Analysis

5.1 Introduction

This section outlines the procedures to determine a precise primary Z = -1 spectrum from 10 GeV to 200 GeV and how a search of this spectrum for signatures of dark matter was conducted. The analysis used the AMS-01 data to determine a detected count rate per energy bin. A simulation of the AMS-01 detector, developed by the AMS collaboration using the GEANT 3 Monte-Carlo package [67], was used to characterize the acceptance and momentum resolution of protons and electrons entering AMS-01 with momentum 1-1000 GeV. This analysis can be followed schematically using Figure A-1 in appendix A. A number of cuts were used to obtain clean samples of Z = $+1$ and Z = -1 particles. The Z = $+1$ data set was mostly protons and, along with data from the AMS-01 simulation, allowed an estimation of the mis-measured protons in the Z = -1 data sample. The Z = -1 data set consisted of electrons, mis-measured protons, antiprotons and secondary pions generated in the upper part of the detector. This analysis required a number of data quality cuts to obtain a clean Z = -1 sample of electrons and antiprotons while still retaining enough high energy events to make a flux measurement out to 200 GeV. Throughout this Chapter histograms of spectra will be plotted as a function of the logarithm of the measured momentum in GeV from 0.1 GeV to 1000 GeV in 40 bins. All flux are given in counts per logarithmic bin.

5.2 Data Selection

The AMS-01 dataset consists of approximately 100 million events, the vast majority of which are protons. The AMS-01 Monte-Carlo was used to generate approximately 36 million protons and 15 million electrons to characterize the efficiency, resolution, and acceptance of the detector. These were generated with a logarithmically flat momentum distribution from 1-1000 GeV (to simplify acceptance estimation) and an example set of Monte-Carlo parameters can be seen in appendix B.

The first step in the data analysis was to impose a number of quality cuts for each event to determine a clean sample of Z = $+1$ and Z = -1 events. These cuts were applied in three steps: *preselect, select* and *analysis* which allowed for progressively

PRESELECT			
Cuts	Data (% cut)	MC protons (% cut)	MC electrons (% cut)
No Reconstructed Particle	35.0	88.8	88.2
No Reconstructed Track	8.01	0.00	0.00
TOF hits < 3	0.04	5×10^{-5}	0.00
ACC hit	0.90	12.3	10.6

Table 5.1: Preselection Cuts. Value shown is the percent of events cut which passed all the cuts above it in the table. It should be noted that a large number the simulated events simply missed most of the detector and did not yield a reconstructed particle.

more complicated cuts on each event. The majority of these cuts were developed from studies in previous works (see [54, 48, 68, 69]). The efficiencies of the cuts are listed in Tables 5.1, 5.2 and 5.3.

5.2.1 Preselection Cuts

After the AMS-01 flight the raw data, which consisted of various ADC and TDC values, tracker strips, temperature measurements, etc, were compiled into PAW ntuples using the AMS-01 event reconstruction program [70] (see appendix C for description). Reconstruction was performed as described in Chapter 4 yielding the mass, charge sign, charge magnitude, momentum, velocity and direction for each event. The initial set of preselection cuts required that each event pass a minimum set of requirements, such as having at least one reconstructed track and one reconstructed particle. Additionally all events were required to have hits in at least 3 TOF planes and no hits in the ACC, which would indicate either an event with nuclear scattering or a coincidence with a particle passing through the side of the detector. A list of these cuts can be seen in Table 5.1.

5.2.2 Selection Cuts

Once a subset of reconstructed events was determined various velocity, charge, and rigidity cuts were applied to the data and Monte-Carlo electron and proton events (see Table 5.2).

Track Quality Cuts

Track quality cuts were implemented in order to make sure the rigidity and charge sign of the particle were accurately measured. The rigidity of each event was determined by both a Fast fit and a GEANE fit (see section §4.3.2). The latter was required to be > 0.2 GV (see Figure 5-1). Generally the GEANE fit was considered more accurate at

SELECT	**Data**	**MC protons**	**MC electrons**
Track Cuts	(% cut)	(% cut)	(% cut)
Tracker Halves = 0	0.02	3×10^{-5}	0.00
Tracker Halves don't match	3.20	33.8	28.1
HRidgidity$_{1,2}$/gridgidity too different	39.2	69.3	64.4
span < 4	12.5	13.2	12.5
gaps in track	42.3	47.0	46.1
gridgidity < 0.2 GV	0.56	0.18	0.26
|Tof hit-Extrapolated Tracker hit| > 5.5 cm	25.0	10.4	9.97
FalseTOF hits for 4 hit event	15.4	11.4	11.7
$0.4 <$ GEANE fit track/Fast fit track < 2.5	35.1	7.38	2.41
Fast Fit χ^2 w/o multiple scattering	13.3	3.41	4.43
$\chi^2_{FastFit}$ too different from either $\chi^2_{HRigidity(1,2)}$	0.95	1.74	2.06
Tracker Clustercut	10.0	4.31	5.92
Velocity Cuts	(% cut)	(% cut)	(% cut)
Number of TOF hits to build $\beta < 3$	0.05	4×10^{-3}	3×10^{-3}
χ^2_β(time fit) > 3	3.20	2.11	1.94
χ^2_β(space fit) > 5	0.18	0.00	0.00
$\beta_C < 0$	8×10^{-4}	0.00	0.00
Charge Cuts	(% cut)	(% cut)	(% cut)
Charge from Tracker or Charge from TOF $\neq 1$	17.2	8×10^{-3}	0.13

Table 5.2: Selection Cuts. Value shown is the percent of events cut which passed all the cuts above it in the table. It should be noted that a number of these cuts are momentum dependent making direct comparison between data (assumed to follow a power-law distribution) and simulation (generated with a uniform log distribution) difficult.

low rigidity while the Fast fit worked better at higher rigidity [71]. The two fits were required to be consistent by applying the following cut:

$$0.4 < \frac{R_{\text{Fast}}}{R_{\text{GEANE}}} < 2.5\,. \tag{5.1}$$

In addition to the rigidity measured on the full track (at least 4 hits) the Fast fit also measured the rigidity of the first 3 hits and the last 3 hits of the track. These "half" fits were required to yield non-zero rigidity with the same curvature sign for each half. If the signs did not match it would indicate the curvature from the upper 3 hits was different from the lower 3 hits possibly due to large scattering. The χ^2 for each half fit was also compared to the χ^2 for the total Fast fit and the event was cut if the difference was too large (see Equation 5.2):

$$|\chi^2_{\text{Fast}} - \chi^2_{\text{Upper or Lower Half}}| < 30\,. \tag{5.2}$$

Additionally the upper and lower half fits were required to be close to the fit generated by GEANE (see Equation 5.3):

$$|\frac{R_{Upper\ Half}}{R_{GEANE}} - \frac{R_{Lower\ Half}}{R_{GEANE}}| < 0.45\,. \tag{5.3}$$

A Fast fit was also generated without including any uncertainties from multiple scattering. Since this fit was performed without all the errors it is more appropriate to call the χ^2_{No-MS} a "track quality estimator" [54]. A correspondingly high χ^2_{No-MS} for such a fit could possibly indicate a large amount of scattering [54] and events were removed if $\chi^2_{No-MS} > 200$.

Tracks were also required to be made of hits which spanned at least 4 tracker planes. Events were cut if gaps existed in which a tracker plane registered no hits even though hits were detected in the planes above and below it. Such gaps could mask large scattering events which could lead to a lower measured rigidity (see Figure 5-2).

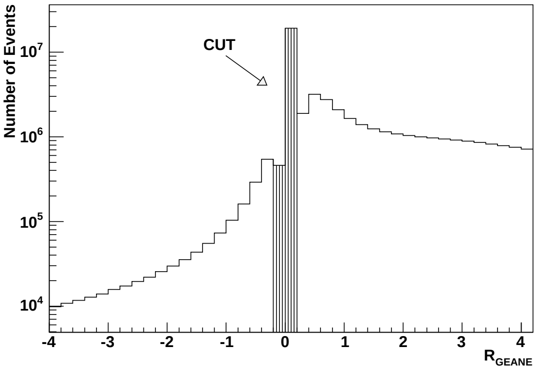

Figure 5-1: Number of events as a function of rigidity measured with the GEANE fit.

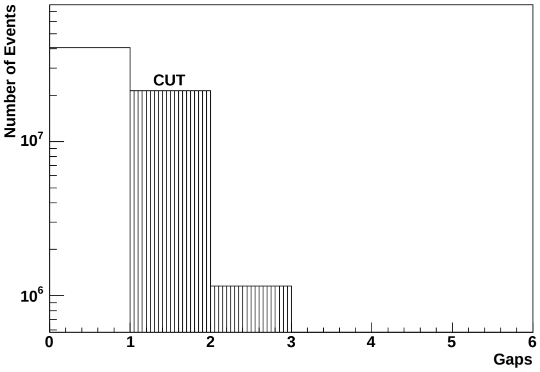

Figure 5-2: Distribution of gaps.

Generally tracks were generated by finding the most populated combination of tracker hits which fit a straight line (with a minimum of 4 hits and a $\chi^2 < 5$) [56]. Sometimes this was not possible because there were not enough K-side (x-direction, non-bending plane) clusters with a high enough signal-to-noise. In these cases 3-hit combinations were tried and false K-side clusters were added to the missing hits (according to the 3-hit track). A new attempt was then made to reconstruct the track. If even the 3-hit method didn't work sometimes the straight line fit to the TOF clusters was used to generate K-clusters (referred to as FalseTOF K-side clusters). Following the recommendations of reference [54] tracks were cut if they only had 4 hits and FalseTOF K-side clusters.

The position of the events on the TOF planes could be measured in two different ways. First the upper two and lower two planes were arranged in orthogonal directions allowing for the position to be measured. Additionally the difference in timing from the PMTs on each scintillator paddle end allowed the hit location to be determined to 1.8 cm [63]. Finally the event could be extrapolated back to the TOF using the tracker information. The event was kept if the extrapolated TOF hits matched the measured TOF hits to within 5.5 cm.

Possible backgrounds could arise from events which generate secondaries in the upper part of the detector. These events were removed by placing a cut on the amount of energy deposited near each track (see "Tracker Clustercut" in Table 5.2).

Velocity Cuts

Accurate measurements of a particle's velocity and overall direction are important to determine its mass and charge sign. To establish confidence in the velocity measurement a number of cuts were applied to data from the TOF for each event. Velocity measurements were required to be constructed of clusters from at least 3 TOF layers. Fits to velocity using the timing information were required to have a $\chi^2_\beta(\text{time}) < 5$ and fits to the spatial separation of the TOF clusters were required to have $\chi^2_\beta(\text{space}) < 3$ [54] (see Figures 5-3 and 5-4). This allowed the removal of events with possible particle interactions or more than one particle [54].

The velocity of any cosmic ray entering the detector is bounded by the speed of light. Due to the finite resolution of the TOF it was possible to mis-reconstruct events with a velocity greater then the speed of light. As a result a "corrected" velocity, β_c, was calculated which took this resolution into account and always returned a value $\beta_c < 1$ [56]. Equation 5.4 illustrates how β_c was determined from the reconstructed velocity, β, and its error σ_β.

$$\beta_c = \frac{\int_{-1}^{1} x\, e^{-(x-\beta)^2/(2\sigma_\beta^2)} dx}{\int_{-1}^{1} e^{-(x-\beta)^2/(2\sigma_\beta^2)} dx}\,. \tag{5.4}$$

A cut for events with $\beta_c < 0$ was added which removed any events passing up from the bottom of the detector.

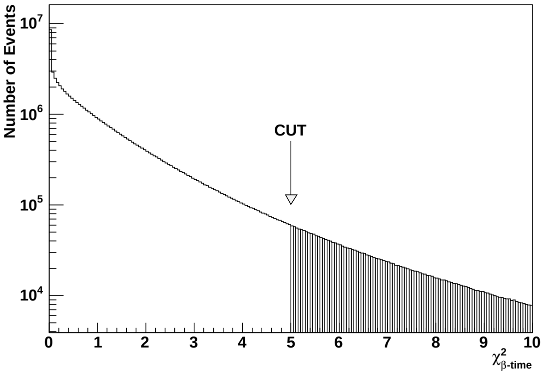

Figure 5-3: Number of data events versus χ^2_β(time).

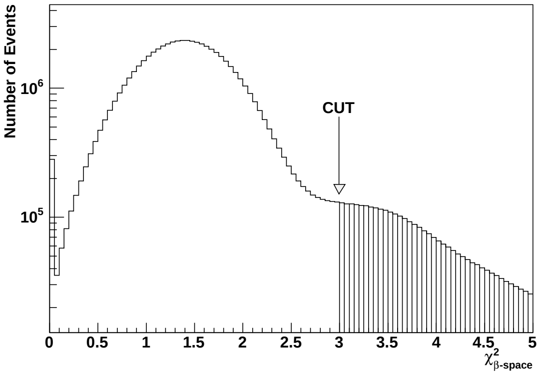

Figure 5-4: Number of data events versus χ^2_β(space).

Charge Magnitude Cuts

The charge magnitude of each event can be measured up to 10 times in AMS-01 from the energy deposition in the 4 TOF planes and 6 tracker planes. A maximum likelihood fit was used to determine the integer charge from both the tracker and the TOF [56] and these were required to agree and have an absolute charge value of Q=|1|. The large number cut from the data, relative to simulation, matches that expected from helium ions and other nuclei.

5.2.3 Analysis Cuts

Finally there were a few global cuts which were applied to reduce backgrounds (see Table 5.3). This included removing events with incident angles greater than 40 degrees from the AMS-01 z-axis (see Figure 4-6) which greatly simplified acceptance calculations and only cut about 2% of events. During the time *Discovery* was docked with *MIR* part of the space station lay in the AMS-01 field of view and generated secondary $\mu^\pm$ and $\pi^\pm$ particles from proton interactions with the station [54]. Since these could corrupt the $Z = -1$ spectrum all events collected during the *MIR* docking were removed. Additionally data was cut when the shuttle passed over the South Atlantic Anomaly where the trigger rate saturated and the detector livetime calculations could not be reliably calculated [48]. A general cut was also applied to any events recorded when the detector livetime was below 35%, which also removed some of the data collected when AMS-01 was at high latitude. These latter cuts did not effect the Monte-Carlo generated protons and electrons because neither the magnetic field of the Earth nor the livetime was simulated and the simulated detector was always pointing at zenith. After all of these cuts the initial data set consisted of 2.4×10^6 $Z = +1$ particles (primarily protons) and 4.1×10^4 $Z = -1$ particles (primarily electrons).

ANALYSIS	Data	MC protons	MC electrons
Additional Cuts	(% cut)	(% cut)	(% cut)
Time docked with *MIR*	41.4	0.00	0.00
South Atlantic Anomaly Region	2.24	0.00	0.00
Livetime fraction < 0.35	0.53	0.00	0.00
Incidence Angle > 40 degrees	1.97	2.51	2.37

Table 5.3: Analysis Cuts: Value shown is the percent of events cut which passed all the cuts above it in the table.

5.2.4 Applying the Geomagnetic Cutoff

A final set of cuts were required to remove particles trapped in the Earth's magnetic field which could distort our primary cosmic ray signals. As mentioned in section §3.4 the Earth's geomagnetic field provides a natural momentum cutoff for primary cosmic rays which varies as a function of latitude, direction and charge. Events below the cutoff were generally due to particles which were trapped in the magnetic field, either from low energy cosmic rays or from particles produced in the upper atmosphere from collisions, which could distort the primary signal. This varying cutoff must be taken into account when correcting for the AMS-01 exposure time. The exposure time for each energy bin is the time in which the total AMS-01 acceptance was available to accept primary particles above that energy. For example the exposure time for primary particles with energy less then 1 GeV was extremely short because the only time the detector was exposed to them was close to the magnetic poles. 100 GeV primary particles had a large exposure time because, even at the equator, the cutoff for most detector positions was well below 100 GeV. The exposure time should not be confused with livetime, which is the amount of time in which the detector is ready to read an event.

Electrons (or antiprotons) and protons, having opposite charges, have different cutoff rigidities when calculated at the same position and incident angle, there by requiring two separate cutoff calculations. If AMS-01 was pointed toward east primary protons were required to have a relatively high momentum while primary electrons/antiprotons could be accepted with a relatively low momentum, and vice-versa when AMS-01 faced west. When low momentum primary electrons/antiprotons were accepted both high momentum mis-measured primary protons and low momentum mis-measured secondary protons were also accepted, contributing to the Z = -1 background. This might have caused the mis-measured proton background (a combination to primary and secondary protons) to deviate from a power-law at low energies. By comparing plots of protons with the Z = $+1$ cutoff and Z = -1 cutoff the effect was estimated to be negligible and was ignored in this analysis.

Following a procedure described in reference [48] only events which had momentum $\vec{p} > 1.3\vec{p}_{\text{cutoff}} + 2.5\sigma(\vec{p})$ were accepted, where $\vec{p}_{\text{cutoff}}$ is the calculated cutoff momentum and $\sigma(\vec{p})$ is the resolution of the measured momentum. Placing the cut well above the calculated value assured that only primary particles were counted. The cutoff momentum was calculated for the most extreme edge of the detector (40 degrees from the

AMS-01 z-axis) where the cutoff momentum would be the highest. This allowed the entire aperture to accept above cutoff particles, simplifying the calculation of acceptance and exposure time. This cutoff was calculated at each shuttle position and was dependent on the magnetic latitude and orientation of AMS-01 with respect to geomagnetic east. The dataset used in this analysis was originally restricted to data taken when AMS-01 pointed within 50 degrees of zenith and later further restricted to data when AMS-01 pointed within 2 degrees of zenith.

In order to extend the exposure so as to collect more primary events the acceptance was divided into two regions [48]; an "incident" region for particles which entered the detector within 20 degrees of the z-axis and an "oblique" region for particles which entered within 20-40 degrees of the z-axis (see Figure 5-5). The maximum cutoff rigidity was calculated separately for each region and was lower for the "incident" region allowing for more primary particles to be accepted. Histograms of the data after accounting for the livetime correction and geomagnetic cutoff can be seen in Figures 5-6 and 5-7. The exposure times were also calculated separately for each region (see Figure 5-8). The two datasets were combined by first dividing each dataset by its corresponding exposure

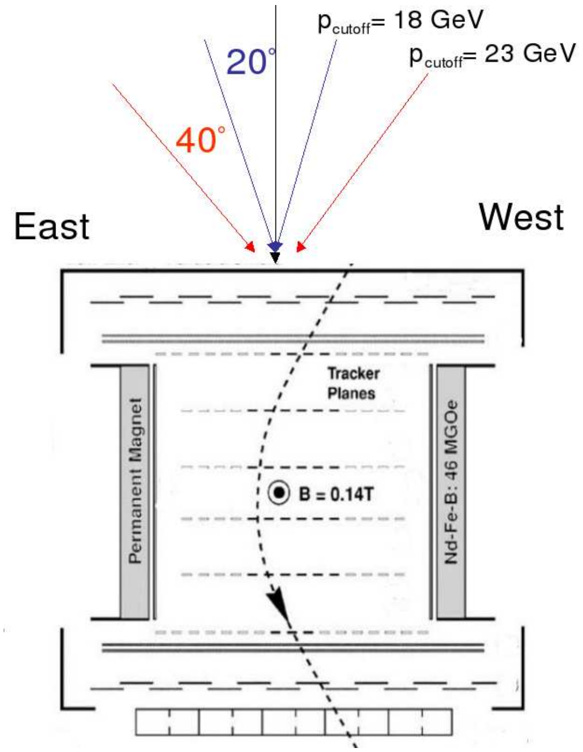

Figure 5-5: Incident (0-20 degree) and oblique (20-40 degree) acceptance regions and the corresponding calculated momentum cutoffs for an electron at their extreme edges. Calculation assumes AMS-01 is at the magnetic equator and pointing toward zenith and the electrons are traveling in the plane of the equator.

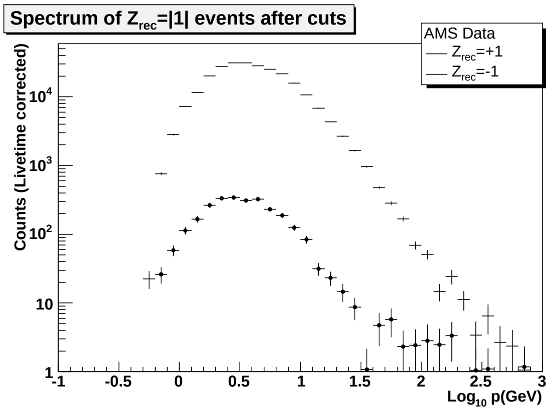

Figure 5-6: Livetime corrected counts for particles detected between 0-20 degrees of AMS-01 z-axis.

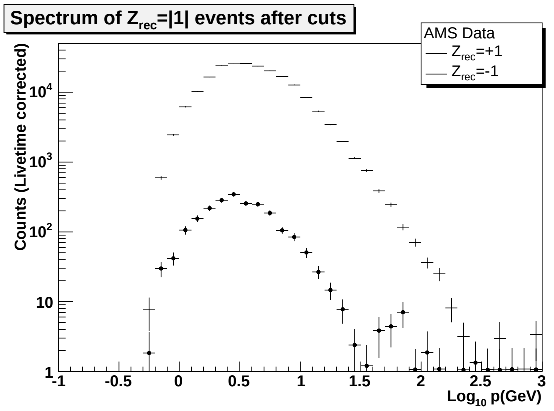

Figure 5-7: Livetime corrected counts for particles detected between 20-40 degrees of AMS-01 z-axis.

time (for each momentum bin). This resulted in the number of primary Z = +1 and Z = −1 particles detected by AMS-01 per second for 0-20 degrees and 20-40 degrees. Adding these results gave the average number of primary particles accepted by AMS-01 between 0-40 degrees (see Figure 5-9). The errors for each momentum bin were scaled by the exposure rate for that bin with the assumption that the error on the exposure rate was negligible. The errors were then combined in quadrature to give the total error on the combined oblique and incident data. The application of this geomagnetic cutoff, combined with the removal of the data subset in which AMS-01 faced Earth, gave us a final dataset of 9.8×10^5 Z = +1 particles (primarily protons) and 1.1×10^4 Z = −1 particles (primarily electrons).

Two data sets were obtained in order to check the calculations of the geomagnetic cutoff as a function of time. The first data set calculates the cutoff separately for Z = +1 and Z = −1 particles as mentioned previously and includes the time in which the detector varied within 50 degrees of zenith. A subset of this data was collected when the detector was pointed within 2 degrees of zenith. In this position the cutoff rigidity is the same for Z = +1 and Z = −1 particles. It was discovered that the full dataset obtained power-law fits that were flatter then observed with the zenith only data. The results for the zenith only subset appeared to be more consistent with other published measurements [33] so it was decided to use this subset in the analysis with the inconsistency of the two datasets to be left to future investigations. The total primary cosmic ray count of the zenith only subset was 2.9×10^5 Z = +1 particles and 3.0×10^3 Z = −1 particles.

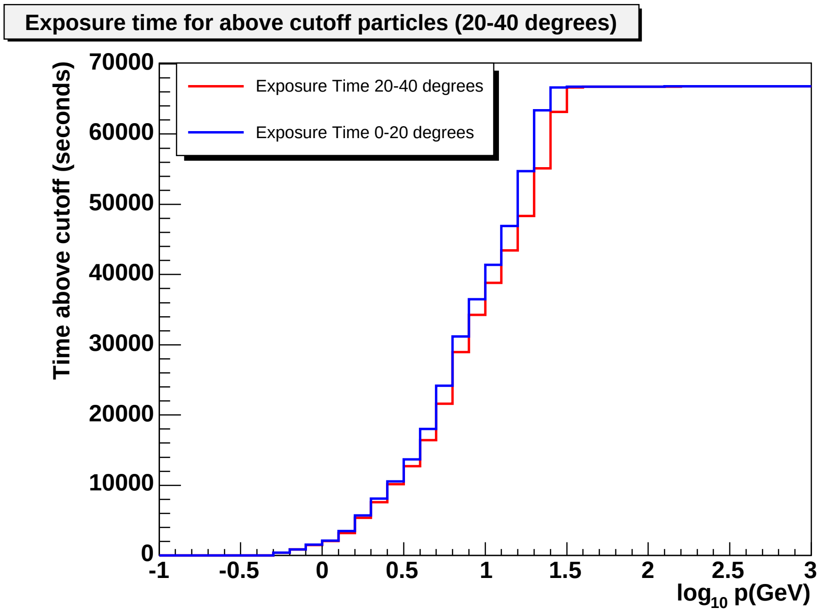

Figure 5-8: The exposure time above geomagnetic cutoff for "incident" particles (0-20 degrees) and for "oblique" particles (20-40 degrees). The total (livetime corrected) counts from Figures 5-6 and 5-7 are then divided by the corresponding exposure time to get the count rate for particles between 0-20 degrees and 20-40 degrees respectively.

5.3 Analysis Method

5.3.1 Initial Dataset

From the data which passed all the previous cuts, histograms of the momentum distribution were made for reconstructed $Z_{\text{rec}} = -1$ particles and for reconstructed $Z_{\text{rec}} = +1$ particles (see Figure 5-9). In generating the momentum spectra from data the livetime of the detector was accounted for by simply dividing each particle by the livetime calculated at the time it was collected. This gave the number of particles one would expect if the detector had 100% livetime. The errors in each momentum bin were maintained to be the square-root of the number of events detected (with negligible error from livetime estimates).

From the Monte-Carlo, 2-D histograms were made of the number of events with initial MC momentum versus reconstructed momentum. These 2-D histograms give the resolution function after all cuts and allow for the estimation of detector inefficiencies, momentum resolution and gathering area (see Figure 5-10).

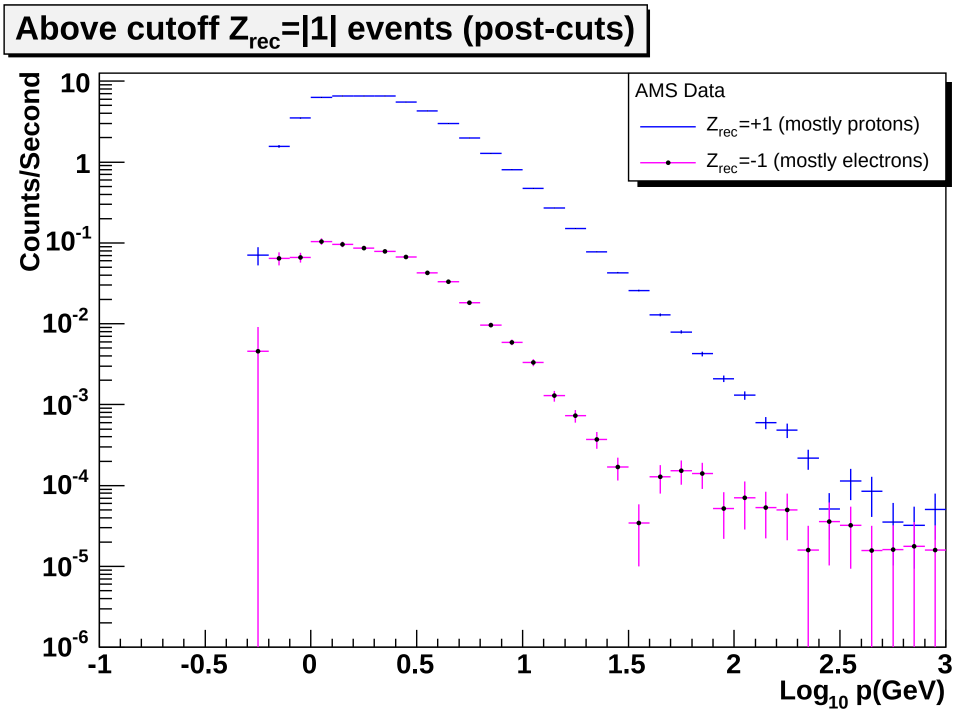

Figure 5-9: The rates for AMS-01 to detect charge Z = +1 and Z = −1 particles as a function of momentum (livetime and exposure time corrected). This plot is generated from the time AMS-01 was pointed toward zenith.

5.3.2 Acceptance, Efficiency and Resolution

Once the total rate of primary Z = ±1 particles was determined the flux could be calculated using Monte-Carlo estimates of the detector's geometric acceptance, detection efficiency and momentum resolution. The latter two were combined into the probability for a particle entering the detector acceptance (A) with momentum p_j to be detected with reconstructed momentum p_i ($P(p_i|p_j)$). Equation 5.5 shows how these two functions relate the detected spectra, $\Phi(p_i)$ (with units 1/sec), to the primary flux integrated over momentum, $\Phi'(p_j)$ (with units 1/m^2-str-sec).

$$\Phi(p_i) = \sum_{j=1}^{40} P(p_i|p_j)\ A\ \Phi'(p_j)\,. \tag{5.5}$$

The AMS-01 Monte-Carlo simulation was used to generate events uniformly on a surface 1 meter above the center of the simulated detector. The surface area was chosen to be large enough so that it entirely covered the aperture but small enough so that most of the simulated events entered the detector. Using Figure 4-6 as a reference all events were generated within 90 degrees of the detectors z-axis (toward the detector). The aperture, efficiency and resolution matrix were combined into a total acceptance

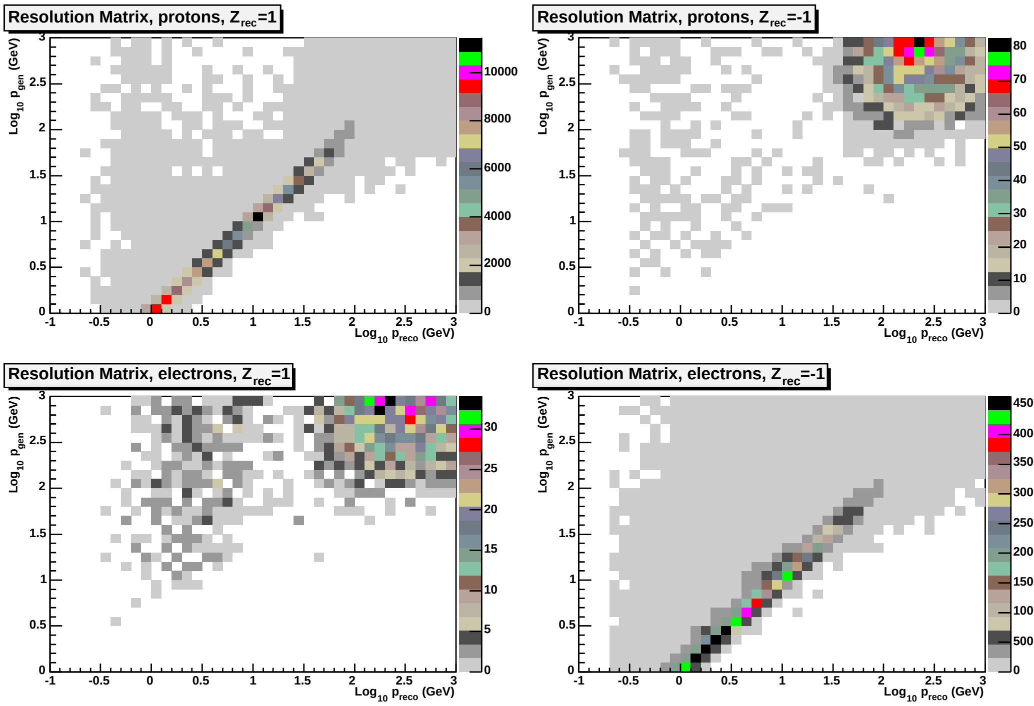

Figure 5-10: The resolution matrices which show the probability for a particle with generated momentum (y-axis) to be detected with a certain reconstructed momentum (x-axis). They are divided into correctly and incorrectly measured charge sign plots. In the mis-reconstructed charge plots the events in the upper right are generally due to loss of detector momentum resolution while the events on the left are most likely a result of multiple scattering.

matrix, $A(p_i|p_j)$, by first determining the number of events with generated momentum p_j and reconstructed momentum p_i, which defined the resolution matrix, $r(p_i|p_j)$. Each generated momentum bin was then multiplied by the generating area times the subtended solid angle [72] divided by the number of events simulated in that momentum bin. This gave the acceptance matrix, $A(p_i|p_j)$, with units of m^2-str (see Equation 5.6):

$$A(p_i|p_j) = r(p_i|p_j)\frac{Generating\ Area \times \pi}{Number\ Generated(p_j)}\,. \tag{5.6}$$

This was determined separately for events with correctly reconstructed charge sign and mis-reconstructed charge sign as illustrated by the labeling of the various acceptance matrices in Table 5.4.

The error on the acceptance matrix was determined as a combination of systematics and finite Monte-Carlo statistics. For bins with a large number of events ($n > 5$ events) the errors were considered as $\sqrt{n}$ and added in quadrature. Initially bins with a smaller number of events were required to sample from the Poisson distribution for each bin in

Matrix Label	Events with correctly measured charge
$A^e_-(p_i \mid p_j)$	electrons with $Q_{rec} = -1$
$A^p_+(p_i \mid p_j)$	protons with $Q_{rec} = +1$
	Events with mis-measured charge
$A^e_+(p_i \mid p_j)$	electrons with $Q_{rec} = +1$
$A^p_-(p_i \mid p_j)$	protons with $Q_{rec} = -1$

Table 5.4: Labeling of acceptance matrices to be used later in the analysis.

order to correctly determine the errors but, when compared with the combined errors from using $\sqrt{n}$ for all bins it was determined that this difference was small enough to safely ignore.

Systematic corrections to the acceptance arose from trigger efficiency variations and differences in event reconstruction. The Monte-Carlo generally overestimated the efficiency of the subdetectors and triggers. Most of these effects were studied using prescaled events (see §4.2.2) for Z = +1 particles in [73, 53] and this analysis assumes similar effects for Z = −1 particles. For corrections to the efficiency of the Monte-Carlo Fast trigger prescaled events could not be used due to their requirement of a Fast trigger. By comparing events that only triggered one end of a TOF paddle to events which triggered both ends a correction of -3 ± 1.5% could be estimated for the Fast trigger [54]. Using prescaled events it was determined that the Level 1 Trigger was well simulated and corrections to the efficiency of the ACC were 0 ± 1%. For the Level 3 trigger the efficiency correction for a signal at both ends of a TOF cluster in plane 1 was -4 ± 2%. The correction for the Level 3 trigger requirement of least 3 track clusters within the TOF generated fiducial road was -2 ± 1% . Simulated particles were also reconstructed slightly more efficiently then real particles (from comparison to beam tests) requiring corrections to the track and velocity reconstruction of -2 ± 1% and -3 ± 1% respectively. Finally the interactions of particles in the detector added a correction of +1 ± 1.5% to the efficiency. All of these corrections were found to be weakly momentum dependent [54] and could be added as an overall correction to the detector acceptance calculated from the Monte-Carlo. A list of the acceptance corrections can be found in Table 5.5.

The systematic corrections were added to the acceptance matrices in Table 5.4 by subtracting 13% from each bin ($N = (1 - 0.13) \times N_{counts}$) and adding the overall systematic error of $\sigma_{sys} = 0.035 \times N_{counts}$ to the statistical error of each bin in quadrature:

$$\sigma_{bin} = \sqrt{\sigma_{sys}^2 + \sigma_{stat}^2} = \sqrt{(0.035 \times N_{counts})^2 + N_{counts}}\,. \tag{5.7}$$

5.3.3 Primary Spectra and Background Estimation

Determining the Z = −1 spectrum required accounting for the background from protons with mis-measured charge ($Q_{rec} = -1$). The large flux of protons (10^2 times greater then electrons at 10 GeV) meant that even a small percent of mis-reconstructed events

Correction	Value and Error in %
Fast Trigger	-3 ± 1.5
ACC Trigger	0 ± 1
Level3 TOF	-4 ± 2
Level3 Tracker	-2 ± 1
Track Fit	-2 ± 1
β Fit	-3 ± 1
Particle Interactions	+1 ± 1.5
Total Correction	-13 ± 3.5

Table 5.5: Proton acceptance corrections and corresponding systematic uncertainty

would lead to a large background, especially at higher energies where the tracker loses momentum resolution. The method used was to estimate the proton spectrum above AMS-01 and then use the mis-measured charge acceptance matrix $A^p_-(p_j|p_i)$ to determine the expected background rate as a function of momentum.

The proton spectrum was estimated by assuming a power-law with no large variations over the range of 10-200 GeV. The power-law spectrum was defined by the following equation: $\Phi(p) = Np^\gamma$, where N is the normalization, p is momentum and γ is the spectral-index. To get the number of particles for each momentum bin (i) the power-law was integrated over each bin's momentum range:

$$\Phi'_{int}(p_i) = \int_{p_{i-0.5}}^{p_{i+0.5}} Np^\gamma dp\,. \tag{5.8}$$

This integrated flux was then convolved with the proton acceptance matrix for correctly measured charge $(A^p_+(p_j|p_i))$ to obtain expected count rates in the detector:

$$\Phi_{simulation}(p_i) = \sum_{j=1}^{40} A^p_+(p_i, p_j)\Phi'_{int}(p_j)\,. \tag{5.9}$$

The errors on this expected count rate were determined by scaling the errors from the acceptance matrix (as determined in §5.3.2) by the integrated flux and adding them in quadrature:

$$\sigma_{simulation}(p_i) = \sqrt{\sum_{j=1}^{40}(\sigma_{Acceptance}(p_i, p_j) \times \Phi'_{int}(p_j))^2}\,. \tag{5.10}$$

The expected counting rate was then fit to the data $(\Phi_{data}(p_i))$ using the program Minuit [74] and the SIMPLEX minimization routine to minimize the χ^2 with the normalization (N) and spectral-index (γ) as free parameters:

$$\chi^2 = \sum_{i=21}^{33} \frac{\Phi_{data}(p_i) - \Phi_{simulation}(p_i)}{\sigma^2_{data}(p_i) + \sigma^2_{simulation}(p_i)}\,. \tag{5.11}$$

Proton Flux	$\Phi'_{int}(p_j) = \mathrm{N}p_j^{-\gamma}$
Normalization (N)	$(9.1 \pm 0.6) \times 10^3$
Spectral Index (γ)	-2.68 ± 0.02
χ^2	21.25
NDOF	11

Table 5.6: Proton background fit parameters. The errors were calculated using the MINOS package in Minuit.

The fit range was set to 10-200 GeV (bins 21 to 33) to avoid solar modulation effects at low momentum. The results for this fit of the proton background are listed in Table 5.6 and can be seen in Figure 5-11

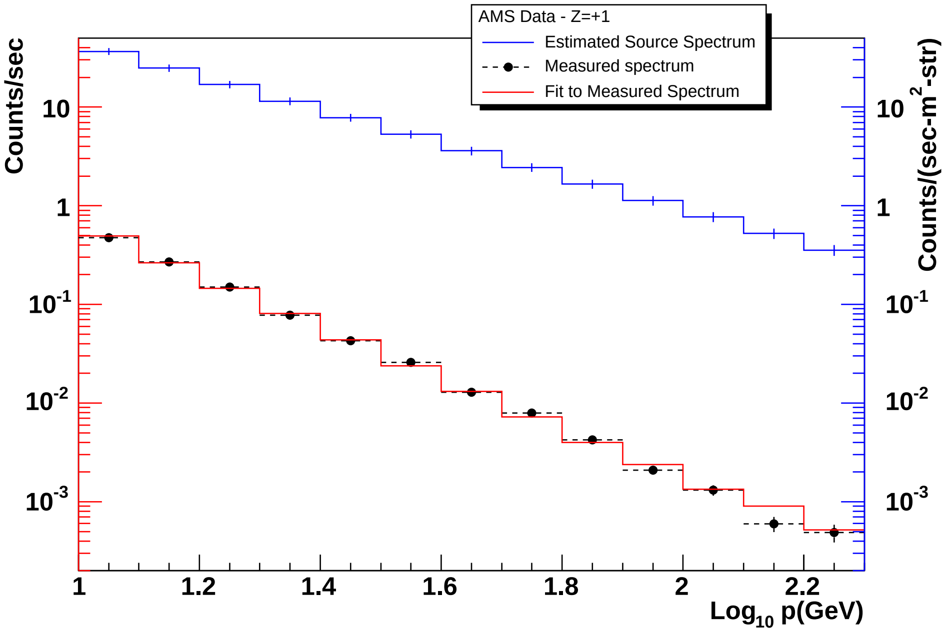

Figure 5-11: A fit of a power-law convolved with the acceptance matrix with the measured spectrum for protons (left hand axis). The upper plot shows what the projected primary proton power-law spectrum would look like (right hand axis).

The contribution of mis-measured protons to the $Z = -1$ spectrum was determined by taking the estimated proton flux and convolving it with the acceptance matrix for protons with mis-measured charge, $Z_{\mathrm{rec}} = -1$ (see Equation 5.6 and Table 5.4):

$$\Phi_{bkgd}(p_i) = \sum_{j=1}^{40} A^p_-(p_i, p_j)\Phi'_{int}(p_j)\,. \tag{5.12}$$

The Poisson nature of the low statistics in the mis-measured proton acceptance matrix (A^p_-) needs to be accounted for in estimating the proton background to the Z = −1 spectrum. The value of each $\Phi_{bkgd}(p_i)$ was estimated by first generating a Poisson distribution for each integer value of the resolution matrix for $r(p_i, p_j)$. Each distribution was then sampled and multiplied by the corresponding generating area over number generated times source flux. The contribution of all 40 possible values were added up to give one entry into the $\Phi_{bkgd}(p_i)$ histogram. This procedure was repeated until a relatively smooth distribution was obtained in which the most probable value was chosen for $\Phi_{bkgd}(p_i)$ and the error on this value was determined by the range which contained 68.27% of the error and the highest probability density. Comparing this to the results for simple gaussian errors showed only minor differences and, for simplicity, the gaussian errors were used for the remainder of the analysis. Figure 5-12 shows the uncorrected electron spectrum with the estimated mis-reconstructed proton background.

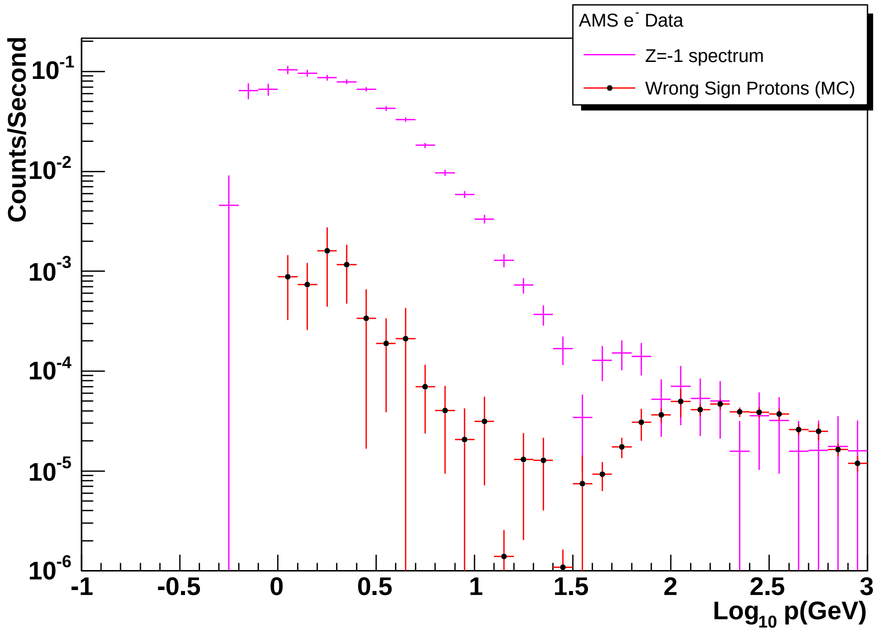

Figure 5-12: Spectrum for charge $Z_{rec} = -1$ particles including the estimated contribution from mis-reconstructed protons.

5.3.4 W^+W^- final state generation

By concentrating on searching for W^+W^- pairs produced in the local area of the galaxy various details of dark matter candidate decays and interactions could be ignored. W^+W^- pairs decay directly (or via quark fragmentation) to stable particles such as neutrinos, photons, protons and electrons as well as their antiparticles. The Pythia Monte-Carlo code [10] was used to determine the electron and antiproton spectra of a W^+W^- pair decay chain with total center of mass energies from 160 GeV-2000 GeV (80-1000 GeV for each W boson). This range was determined by the minimum energy to create a W^+W^- pair from WIMP co-annihilation and the upper-range of plausible dark matter candidates of approximately a TeV.

Figures 5-13 and 5-14 were generated by decaying 10^6 W^+W^- pairs in PYTHIA, collecting the output electrons and antiprotons and normalizing by 10^6 to get the average result for one W^+W^- pair. This essentially gave the primary $Z = -1$ spectrum at the point where the dark matter co-annihilated through W^+W^- production. The errors on this spectrum were determined to be negligible compared to the errors from the data. The next step was to convolve this with the results from GALPROP for electron and antiproton propagation in the galaxy in order to determine the actual flux from dark matter sources expected at Earth.

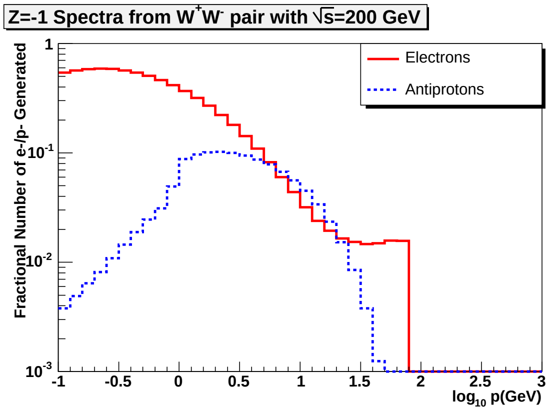

Figure 5-13: W^+W^- E_{cm}=200 GeV

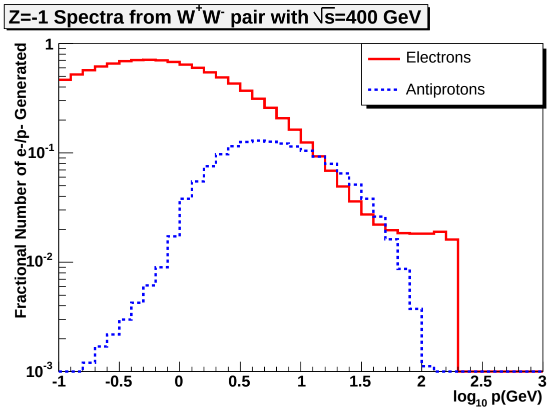

Figure 5-14: W^+W^- E_{cm}=400 GeV

5.3.5 GALPROP propagation

The GALPROP code was written by Igor Moskalenko and Andrew Strong in order to simulate cosmic ray propagation through the galaxy [11]. Using an input source distribution and boundary conditions, GALPROP solves the galactic transport equations for all known cosmic ray species using the propagation Equation 3.6.

For this analysis sources of electrons and antiprotons were placed at different grid points in the galaxy. A specific energy (E_g) and position dependent rate of emission ($R(r)$) was set at each point. The rate of emission was related to the WIMP density via Equation 3.5 and this analysis assumes the WIMP density follows an isothermal distribution (Equation 2.1). The source rates were thus defined as:

$$R(r) = R_0 \left(\frac{r_C^2 + r_E^2}{r_C^2 + r^2} \right)^2 , \tag{5.13}$$

where $r_C = 2.8$ kpc is the estimated galactic core radius, $r_E = 8.5$ kpc is the distance of the Earth from the galactic center, r is the distance the grid point is from the galactic center, and R_0 is the electron or antiproton source density at Earth. This density was normalized so that $R_0 = 1$ electron (or antiproton) per cm^3 per second, giving us a rate of production which could easily be convolved with the spectra of electrons and antiprotons from W$^+$W$^-$ decay. The propagation code was run for source energies ranging from 100 MeV to several TeV with a flux at Earth obtained for each source energy. The parameter settings for these propagation runs can be seen in appendix D. Figures 5-15 and 5-16 illustrate the differences in propagation between the light electrons, which spread out relatively quickly in momentum space, and the heavier antiprotons which don't lose their initial energy nearly as quickly.

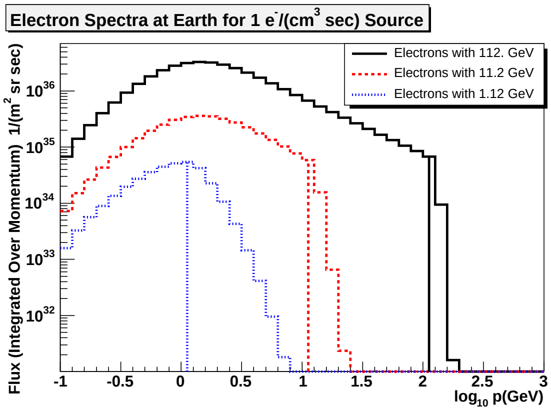

Figure 5-15: Flux at Earth given isothermal distribution of electron sources with specific injection energies (indicated by the vertical lines).

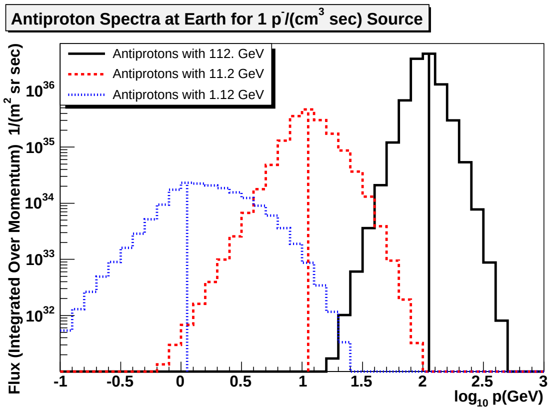

Figure 5-16: Same as 5-15 but for antiproton sources. Both are fluxes from 1 particle/(cm^3-s) to simplify future calculations.

The flux at Earth, for each source electron or antiproton energy, was then convolved with the corresponding spectrum for the various W$^+$W$^-$ pairs in order to see what their signal would be at Earth, given an isothermal distribution. This corresponded to multiplying the value in each energy bin of the W$^+$W$^-$ decay with the spectra for particles propagated at that initial energy and then adding each individual spectrum to get the total for $\rho_0 = 1$ W$^+$W$^-$/(cm^3 sec) at a specific generated energy. Figure 5-17 illustrates the relative rise in the antiproton signal with respect to the electrons from Figures 5-13 and 5-14 as a result of the difference in energy loss rates from galactic propagation.

For this analysis a reasonable propagation model was chosen whose parameters are defined in Appendix D. The model used included diffusive re-acceleration and had a grid spacing of 0.5 kpc in the x-y direction and 4 kpc in the z direction. The galaxy was defined as 20 kpc in radius and 8 kpc in disk thickness. Studies of various GALPROP

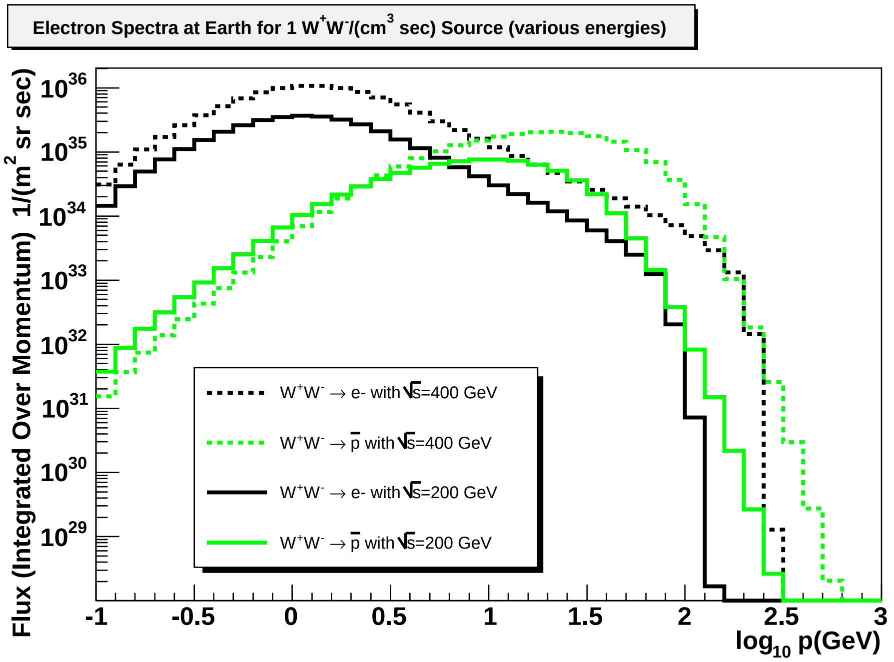

Figure 5-17: Final flux at Earth in electrons and antiprotons for 1 W^+W^- pair per cm^3 per second at 200 GeV and at 400 GeV total center-of-mass energy being generated in the local region of the galaxy.

models with different parameters and grid-spacings found approximately an order of magnitude difference in the flux magnitudes [75]. This potential error in the flux estimates was included in our final results (see Chapter 7).

5.3.6 Dark Matter Fitting Procedure

Once a potential dark matter signal was generated from the GALPROP convolved output of W^+W^- particles generated in the galaxy fits could be made to the data to determine what, if any, contribution dark matter could be making to the $Z = -1$ spectrum. In order to account for all backgrounds a combined fit was done by adding the contributions of a standard power-law electron spectrum, a mis-measured proton spectrum and the dark matter contribution. Each of these contributions were passed through the appropriate acceptance matrices before they could be directly compared to the data. The electron power-law component was determined from Equation 5.14 where the normalization (N_e) and spectral index (γ) were allowed to vary:

$$\Phi_{PL}(p_i) = \sum_{j=1}^{40} A_e^-(p_i; p_j)[\int_{p_{j-0.5}}^{p_{j+0.5}} N_e(p_j)^\gamma] . \tag{5.14}$$

The contribution from the mis-measured protons is given in Equation 5.12 and Figure 5-12.

The expected electron flux from 1 W$^+$W$^-$ pair/cm^3-sec ($\Phi_{DM\ e\ flux}(E)$) was convolved with the acceptance matrix for correctly measured electrons (see Equation 5.15) while the corresponding antiproton contribution ($\Phi_{DM\ \bar{p}\ flux}(E)$) was convolved with the correctly measured proton acceptance matrix (see Equation 5.16).

$$\Phi_{DM\ e}(p_i) = \sum_{j=1}^{40} A_e^-(p_i;p_j)\Phi_{DM\ e\ flux}(p_j)\,. \tag{5.15}$$

$$\Phi_{DM\ \bar{p}}(p_i) = \sum_{j=1}^{40} A_p^+(p_i;p_j)\Phi_{DM\ \bar{p}\ flux}(p_j)\,. \tag{5.16}$$

These contributions were then added together and multiplied by an overall floating normalization N_{DM} to give a combined Z $= -1$ dark matter rate inside the AMS-01 detector. Figure 5-18 illustrates the effect that the AMS-01 acceptance has on a dark matter candidate of 100 GeV. It should be noted that, even though the edge in the electron spectrum at 100 GeV gets smoothed out from poor momentum resolution in this range, the antiprotons contribute enough to show a change in slope at approximately 30 GeV.

$$\Phi_{DM}(p_i) = N_{DM}(\Phi_{DM\ \bar{p}}(p_i) + \Phi_{DM\ e}(p_i))\,. \tag{5.17}$$

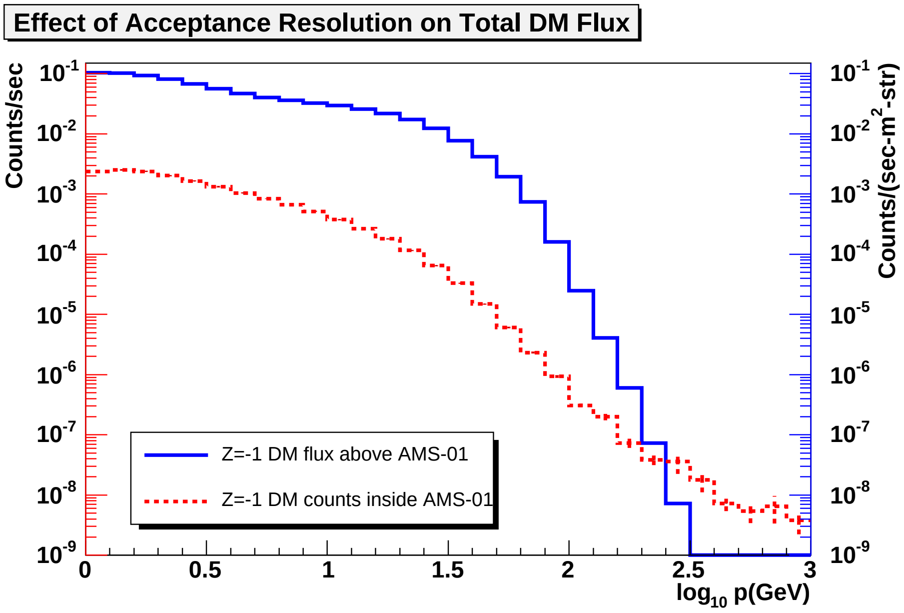

Figure 5-18: Sum of e$^-$ and $\bar{p}$ from 100 GeV DM before and after AMS-01 Acceptance (arbitrary flux normalization). The upper plot is the initial flux (right hand axis) and the lower plot is the corresponding count rate in the detector (left hand axis).

All of these contributions to the Z $= -1$ spectrum were used to define a χ^2 (see Equation 5.18) which was then minimized using the program Minuit, leaving the electron power-law normalization (N_e) and spectral index (γ) and the dark matter normalization (N_{DM}) as free parameters:

$$\chi^2 = \sum_{i=Low\ Range}^{High\ Range} \frac{(\Phi_{data}(p_i) - \Phi_{PL}(p_i) - \Phi_{eback}(p_i) - \Phi_{DM}(p_i))^2}{\sigma_{data}^2 + \sigma_{PL}^2 + \sigma_{eback}^2 + \sigma_{DM}^2}. \tag{5.18}$$

The errors in the power-law and dark matter contributions (σ_{PL}^2 and σ_{DM}^2) of Equation 5.18 were determined primarily from the errors in the acceptance matrices. Fits were then run on this data for various dark matter candidate masses and the results are listed in Table 6.3.

Chapter 6

Results

The final data set consists of Z $= -1$ particles with momentum from 500 MeV to a TeV (Figure 5-9). The AMS-01 Monte-Carlo was used to determine the flux normalization once over-efficiencies were taken into account. For this analysis fits of the data were run with and without dark-matter, in the form of W^+W^- emission, for masses in the range of 80 GeV - 1000 GeV.

6.1 Fitting Procedures

The fitting procedure was performed in the following steps.

1. A power-law fit was performed assuming no measurable dark matter component and allowed the power-law normalization (N_{PL}) and spectral index (γ) to float.
2. To set a baseline conservative limit on dark matter co-annihilation it was then assumed that the entire Z $= -1$ spectrum was due to W^+W^- co-annihilation. This is highly unlikely given the large number of known astrophysical cosmic ray sources but it gives a robust limit. Fits of various dark matter masses returned the expected dark matter normalization (N_{DM}), error, and fit χ^2.
3. Finally a fit was performed with the dark matter and power-law components simultaneously. The normalization of the dark matter (N_{DM}) and the normalization (N_{PL}) and spectral index (γ) of the power-law were allowed to float. The results from this fit was then compared with the previous two fits to determine the maximum possible extent of the dark matter contribution to the measured Z $= -1$ spectrum.

6.2 Power-Law Fit

A fit was performed from 10-200 GeV using only an integrated power-law to model a standard cosmic ray spectrum from astrophysical sources. The dark matter contribution was set to zero and the power-law was convolved with the acceptance matrix of correctly measured electrons. Secondary antiprotons generated from primary cosmic ray collisions are estimated to contribute only negligibly to this Z $= -1$ spectrum. The results of the fit can be see in Table 6.1 and in Figure 6-1.

N_{PL}	Spectral Index γ	χ^2
$362\ ^{+366}_{-176}$	$-3.40\ ^{+0.24}_{-0.26}$	17.4

Table 6.1: Fitting only electron power-law spectrum to data. Number of Degrees of Freedom=11

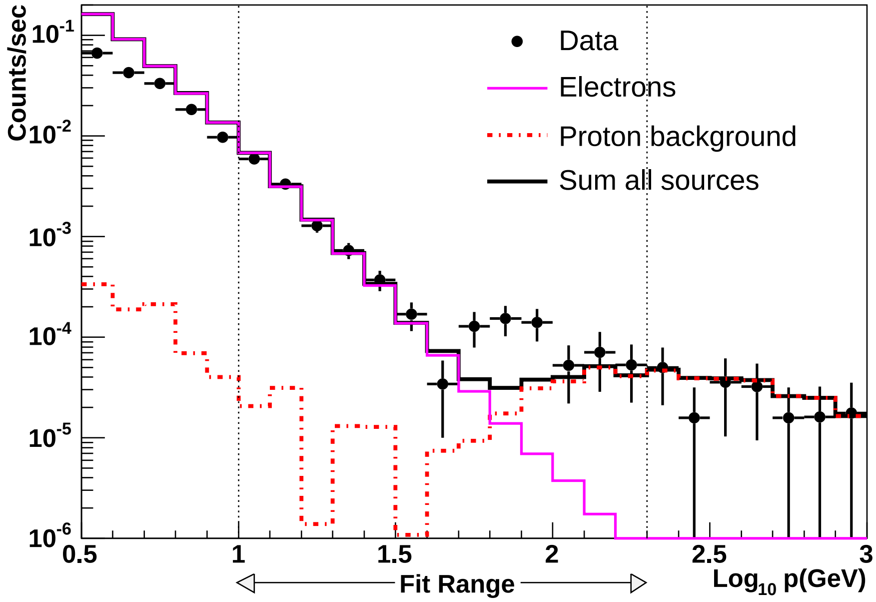

Figure 6-1: The fit of a power-law to the data including the contribution from mismeasured protons (no dark matter).

A residual plot ($\frac{data-fit}{data}$) was also generated in order to determine the deviation of the data from a power-law and can be seen in Figure 6-2. From just a visual inspection there does not seem to be any large deviation from the straight line though the three points between $10^{1.7}$ - $10^{2.0}$ GeV do seem to lie far enough off the line to be of interest. One possibility is that these could be due to variations in the accuracy of the track finding algorithms GEANE and Fast fit (the latter of which is more accurate than the former at around these energies) and could be a target for further investigations [76].

6.3 Dark Matter Only Fits

The initial dark matter fits ran a minimization of the χ^2, defined in Equation 5.18, with the power-law contribution set to zero and a floating dark matter normalization

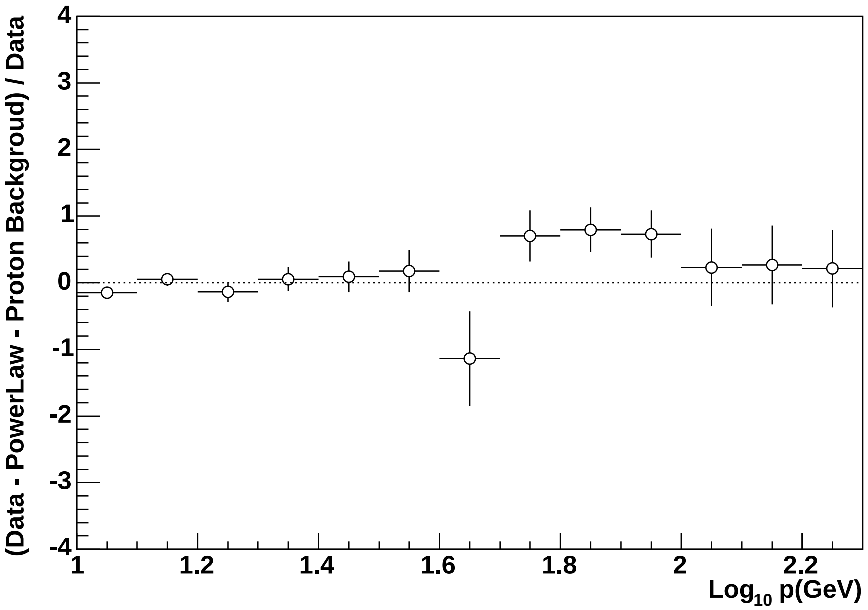

Figure 6-2: Residual plot of data with fitted power-law and proton background subtracted.

N$_{DM}$. The fit range was set from 10-200 GeV. The fits for three dark matter masses are illustrated in Figure 6-3, 6-5, 6-7.

Each fit resulted in an estimated dark matter normalization and error which was used to generate a limit to the rate of W$^+$W$^-$ particles generated locally. The numerical results, including errors and χ^2 from the fits, are specified in Table 6.2 and a plot of the corresponding 90% confidence upper limit to the production rate is shown in Figure 6-9. In general the errors calculated from MINOS were asymmetric (as seen in Table 6.2) but the production rate and cross-section upper limits were generated using symmetric parabolic errors, which were usually quite close the MINOS results.

6.4 Cross Section Limits

Once an upper limit was placed on the rate of W$^+$W$^-$ production (Figure 6-9) a cross-section limit for dark matter co-annihilation could be estimated by transforming Equation 3.5 into:

$$\sigma_{co-annihilation} = \frac{R_{co-annihilation}}{v(\frac{\rho^2}{M_\chi^2})} \,. \tag{6.1}$$

Accounting for the estimated errors in the overall dark matter mass density of $\rho = 0.3 \pm 0.2$ GeV/cm^3 [4] and in the velocity distribution of $\vec{v} = 220 \pm 100$ km/sec and including the previously determined $R_{co-annihilation} \pm \sigma_R$ the error in the estimated cross-

$W^{\pm}$ Energy	Estimated Production Rate	χ^2
(GeV)	N_{DM} in $W^+W^-/(cm^3\text{-sec})$	
80	$(6.0^{+0.5}_{-0.4}) \times 10^{-36}$	27.1
100	$(1.1^{+0.1}_{-0.1}) \times 10^{-36}$	61.2
126	$(5.2^{+0.4}_{-0.5}) \times 10^{-37}$	84.7
158	$(3.0^{+0.3}_{-0.3}) \times 10^{-37}$	102
200	$(1.9^{+0.2}_{-0.2}) \times 10^{-37}$	113
251	$(1.4^{+0.1}_{-0.1}) \times 10^{-37}$	120
316	$(1.0^{+0.1}_{-0.1}) \times 10^{-37}$	126
398	$(8.3^{+1.1}_{-0.7}) \times 10^{-38}$	129
501	$(6.6^{+0.7}_{-0.7}) \times 10^{-38}$	130
631	$(5.6^{+0.5}_{-0.7}) \times 10^{-38}$	131
794	$(4.7^{+0.5}_{-0.6}) \times 10^{-38}$	130
1000	$(4.0^{+0.4}_{-0.5}) \times 10^{-38}$	129

Table 6.2: Fitting only Dark Matter contribution from WIMPs co-annihilating to W^+W^- pairs at a specific energy for each W boson. Number of Degrees of Freedom=12.

section (σ_{CS}) was determined from error propagation to be:

$$\sigma_{CS}^2 = \sigma_R^2 \left(\frac{1}{v(\frac{\rho^2}{M_\chi^2})}\right)^2 + \sigma_v^2 \left(\frac{R}{v^2(\frac{\rho^2}{M_\chi^2})}\right)^2 + \sigma_\rho^2 \left(\frac{2R}{v(\frac{\rho^3}{M_\chi^2})}\right)^2 . \tag{6.2}$$

A 90% confident cross-section limit was then placed on WIMPs co-annihilating into W^+W^- pairs, the results of which can be seen in Figure 6-10.

6.5 Combined Power-Law and Dark Matter Fit

Finally a full fit was performed using contributions from both a power-law and dark matter. The fit allowed the dark matter normalization (N_{DM}) and the power-law normalization (N_{PL}) and spectral index (γ) to float when running the SIMPLEX minimization. When the MINOS error calculations were run the spectral index was set to the constant obtained from the minimization. This was required because the non-linear power-law led to failures with the MINOS routines. The results of this fit for various dark matter masses can be seen in Table 6.3 and examples of three fits can be seen in Figures 6-4, 6-6 and 6-8.

A limit to the contribution from dark matter to the overall spectrum could then be deduced using the same method mentioned in sections §6.3 and §6.4 (see Figures 6-9 and 6-10). By including the standard power-law background, the limits are improved over the dark matter only limits.

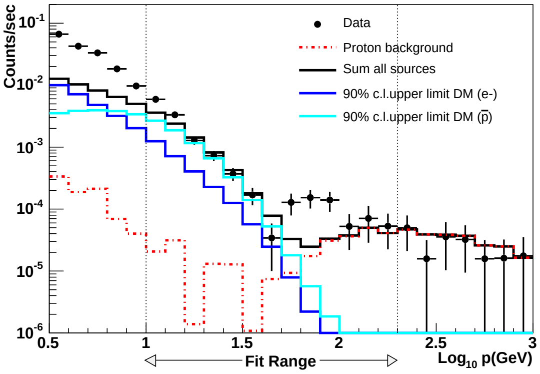

Figure 6-3: Dark matter Z = −1 (mass 80 GeV) fit to data.

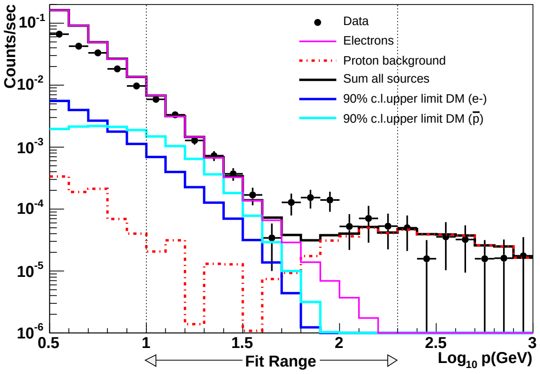

Figure 6-4: Power-Law + dark matter Z = −1 (mass 80 GeV) fit to data.

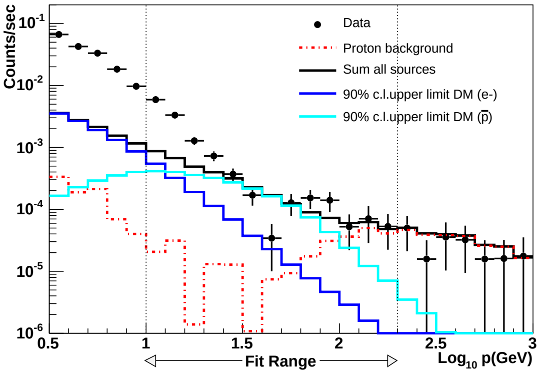

Figure 6-5: Dark matter Z = −1 (mass 250 GeV) fit to data.

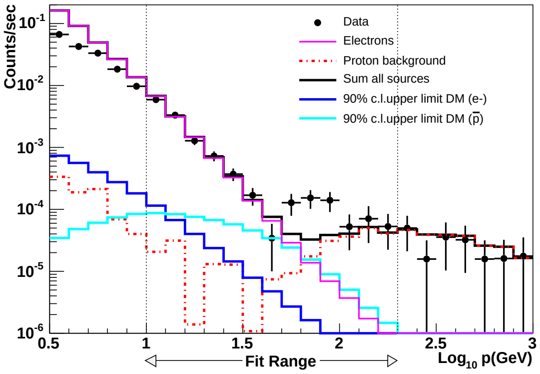

Figure 6-6: Power-Law + dark matter Z = −1 (mass 250 GeV) fit to data.

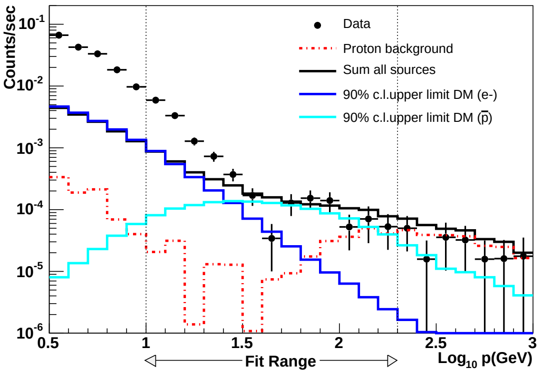

Figure 6-7: Dark matter Z = −1 (mass 1000 GeV) fit to data.

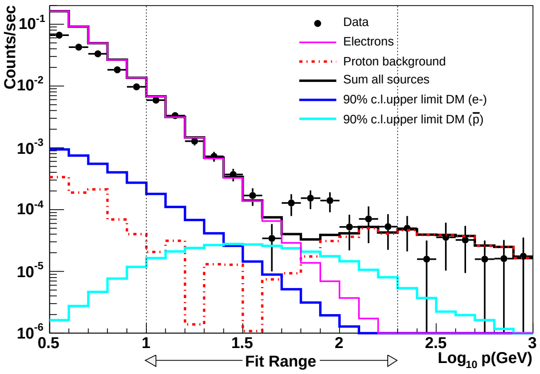

Figure 6-8: Power-Law + dark matter Z = −1 (mass 1000 GeV) fit to data.

$W^{\pm}$ Energy	Production Rate	N_{PL}	γ	χ^2
(GeV)	$W^+W^-/(\mathrm{cm}^3\text{-sec})$			
80	$(0.0^{+1.5}_{-3.2}) \times 10^{-36}$	$363\ ^{+190}_{-94}$	-3.4	17.4
100	$(0.0^{+1.6}_{-2.2}) \times 10^{-37}$	$363\ ^{+65}_{-50}$	-3.4	17.4
126	$(0.1^{+7.3}_{-7.9}) \times 10^{-38}$	$363\ ^{+47}_{-44}$	-3.4	17.4
158	$(0.2^{+4.4}_{-3.9}) \times 10^{-38}$	$363\ ^{+38}_{-42}$	-3.4	17.4
200	$(0.3^{+3.0}_{-2.4}) \times 10^{-38}$	$363\ ^{+33}_{-43}$	-3.4	17.4
251	$(0.3^{+2.4}_{-1.5}) \times 10^{-38}$	$363\ ^{+29}_{-45}$	-3.4	17.4
316	$(0.2^{+2.0}_{-1.0}) \times 10^{-38}$	$363\ ^{+27}_{-48}$	-3.4	17.3
398	$(0.2^{+1.8}_{-0.7}) \times 10^{-38}$	$363\ ^{+25}_{-51}$	-3.4	17.3
501	$(0.1^{+1.6}_{-0.5}) \times 10^{-38}$	$363\ ^{+25}_{-55}$	-3.4	17.2
631	$(0.1^{+1.5}_{-0.4}) \times 10^{-38}$	$363\ ^{+25}_{-58}$	-3.4	17.2
794	$(0.0^{+1.4}_{-0.3}) \times 10^{-38}$	$363\ ^{+25}_{-62}$	-3.4	17.2
1000	$(0.0^{+1.2}_{-0.2}) \times 10^{-38}$	$363\ ^{+26}_{-65}$	-3.4	17.2

Table 6.3: Fitting dark matter contribution from WIMPs co-annihilating to W^+W^- pairs at a specific energy for each W boson plus an astrophysical electron power-law spectrum. Number of Degrees of Freedom=11 (power-law spectral index is set to constant).

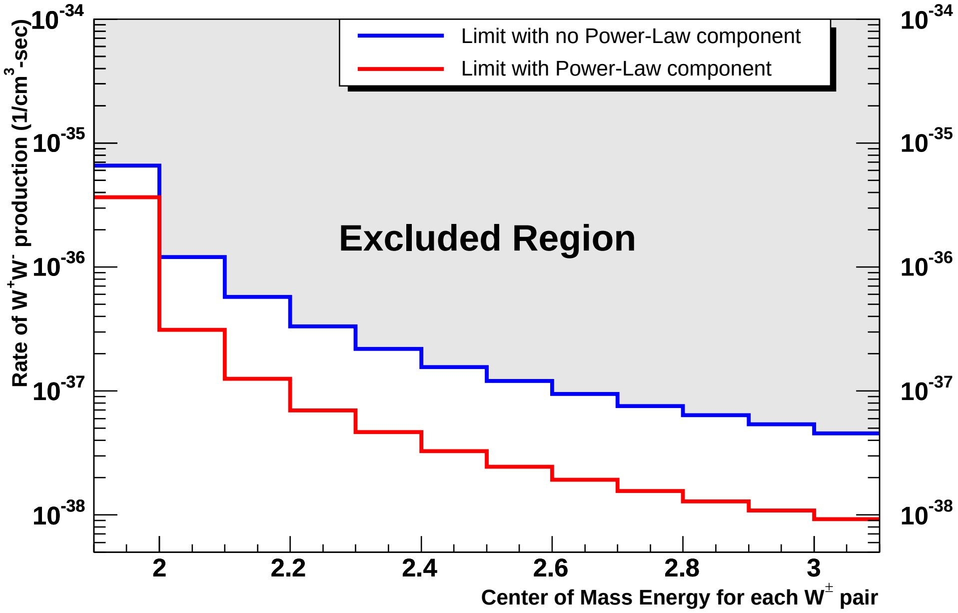

Figure 6-9: The upper limit to W^+W^- production from local dark matter co-annihilation to 90% confidence. The upper curve (blue) is a limit assuming only dark matter is contributing to $Z = -1$ cosmic rays while the lower limit (red) is when a standard astrophysical power-law is added.

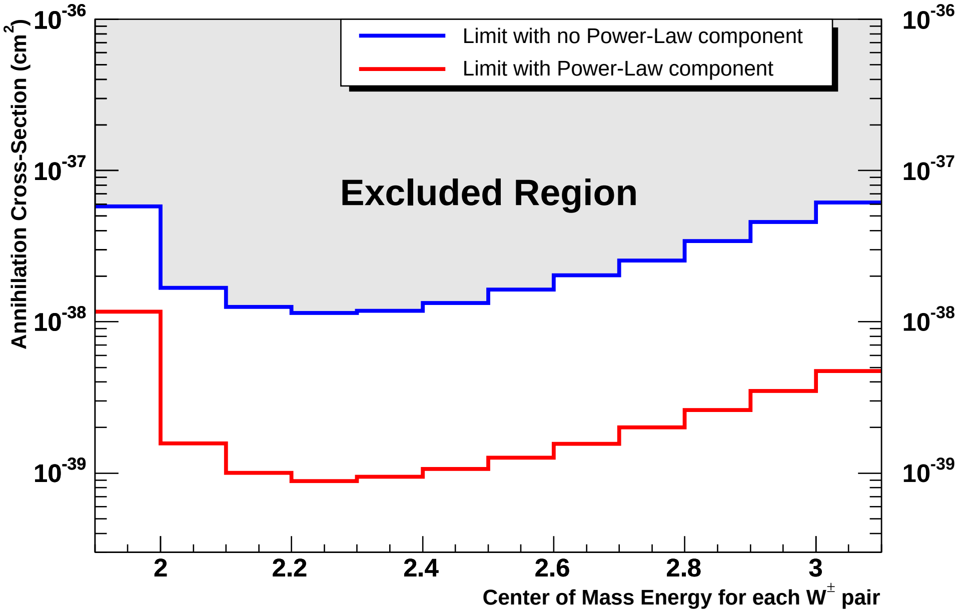

Figure 6-10: The cross-section limits assuming that WIMPs co-annihilate entirely through the W^+W^- channel and that they are distributed throughout the galaxy in a smooth isothermal halo. The upper curve (blue) is a limit assuming only dark matter is contributing to $Z = -1$ cosmic rays while the lower limit (red) is when a standard astrophysical power-law is added.

Chapter 7

Conclusions

7.1 Summary

A search for signatures of WIMPs co-annihilating to W^+W^- bosons in our galaxy was performed by looking in the cosmic ray $Z = -1$ spectrum measured by AMS-01. The GALPROP and PYTHIA simulations were used to generated the shape and proportions of electron and antiprotons which would be observed at earth given a smooth isothermal distribution of dark matter. The normalization of this spectrum was then directly correlated to the amount of W^+W^- production locally in the galaxy. It was discovered that the electron spectrum from dark matter co-annihilation convolved with the AMS-01 acceptance matrix lost any pronounced features from poor momentum resolution of the detector in the region of interest (above 60 GeV).

As a baseline analysis, it was possible to set a very conservative limit by assuming that all $Z = -1$ particles were from dark matter (see §6.3). The main error on this can be taken from the uncertainties in the GALPROP models of propagation (currently taken to be an order of magnitude). These fits generally had a much higher χ^2 than the fit with a simple power-law (which is predicted from standard astrophysics). A combined fit of a power-law and dark matter components also yielded similar χ^2 values as obtained with just a power-law fit leading to the following conclusions:

1. Expected electron power-law spectrum explains the measured spectrum.
2. Dark matter alone can not explain our measured $Z = -1$ spectrum.
3. Added dark matter does not improve the description.
4. The dark matter electron spectrum looks like a power-law with decreasing spectral index as the WIMP mass increases.
5. The dark matter antiproton contribution dominates the electrons at higher energies and has a peak which moves to higher energies for heavier WIMPs.

Though our search did not find any strong signatures of WIMP co-annihilation we were able to place limits on the rate of W^+W^- bosons that could be produced in the

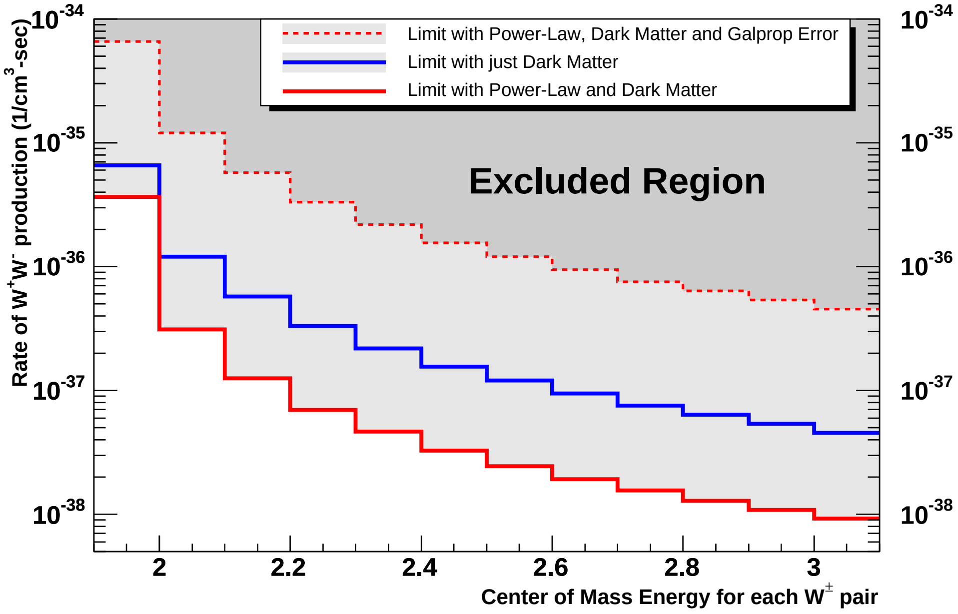

Figure 7-1: Upper limit to W$^+$W$^-$ production from local dark matter co-annihilation at 90% confidence level comparing the dark matter plus power-law limit along with an estimate of the GALPROP error.

local region of the galaxy (see Figure 7-1) as well as limits on their cross-section to co-annihilation (see Figure 7-2). The major source of error on these limits come from the uncertainties in the galactic propagation software GALPROP which could affect the normalization by an order of magnitude, which is also plotted.

7.2 Future Work

7.2.1 Prospects for continued analysis of AMS-01 data

This analysis of the AMS-01 Z = −1 spectrum is not entirely exhaustive. Other work that could be done includes the following.

1. Model Z = −1 rates from ZZ or $b\bar{b}$ channels of WIMP co-annihilation.
2. Searches for monoenergetic sources of WIMP co-annihilation.
3. Searches for signatures from specific SUSY models.
4. Increased studies of GALPROP systematics to tighten errors.
5. Include possible additional effects such as secondary antiprotons from cosmic ray interactions.

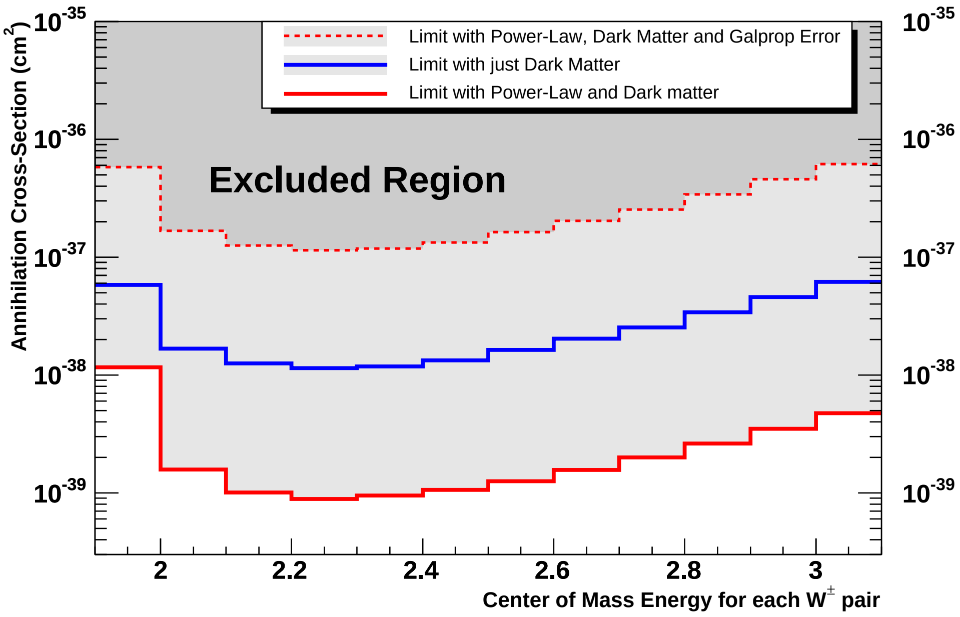

Figure 7-2: Cross-section limits assuming that WIMPs co-annihilate entirely through the W^+W^- channel and that they are distributed throughout the galaxy in a smooth isothermal halo.

6. More studies of the AMS-01 Monte-Carlo could allow for tighter error estimates.

7.2.2 Prospects for AMS-02 search

AMS-02 is currently under construction and is planned to be installed on the International Space Station in 2008. It is essentially the same core design as AMS-01 with a number of major improvements [53]:

- A superconducting magnet with a field 6 times more powerful then original magnet allowing for a much higher maximum design rigidity,
- A fully instrumented silicon tracker,
- A Transition Radiation Detector (TRD) for the separation of protons from electrons and positrons with momenta up to 300 GeV,
- A Ring Imaging Cerenkov Counter (RICH) which will replace the threshold Cerenkov counter of AMS-01,
- An Electromagnetic Calorimeter (ECAL) which can also distinguish protons from electrons and positrons,
- A 3 year exposure time.

The electron-positron/proton separation using the TRD and the ECAL will allow AMS-02 to make an extremely precise measurement up to 300 GeV allowing us to make a direct comparison to the HEAT results [77]. If the anomalous rise that the HEAT detector saw at 10 GeV exists in the AMS-02 data and it drops back to the expected curve for positrons from cosmic pion production it would be a very strong indication of WIMP co-annihilation in the galaxy.

Appendix A

Analysis Chain

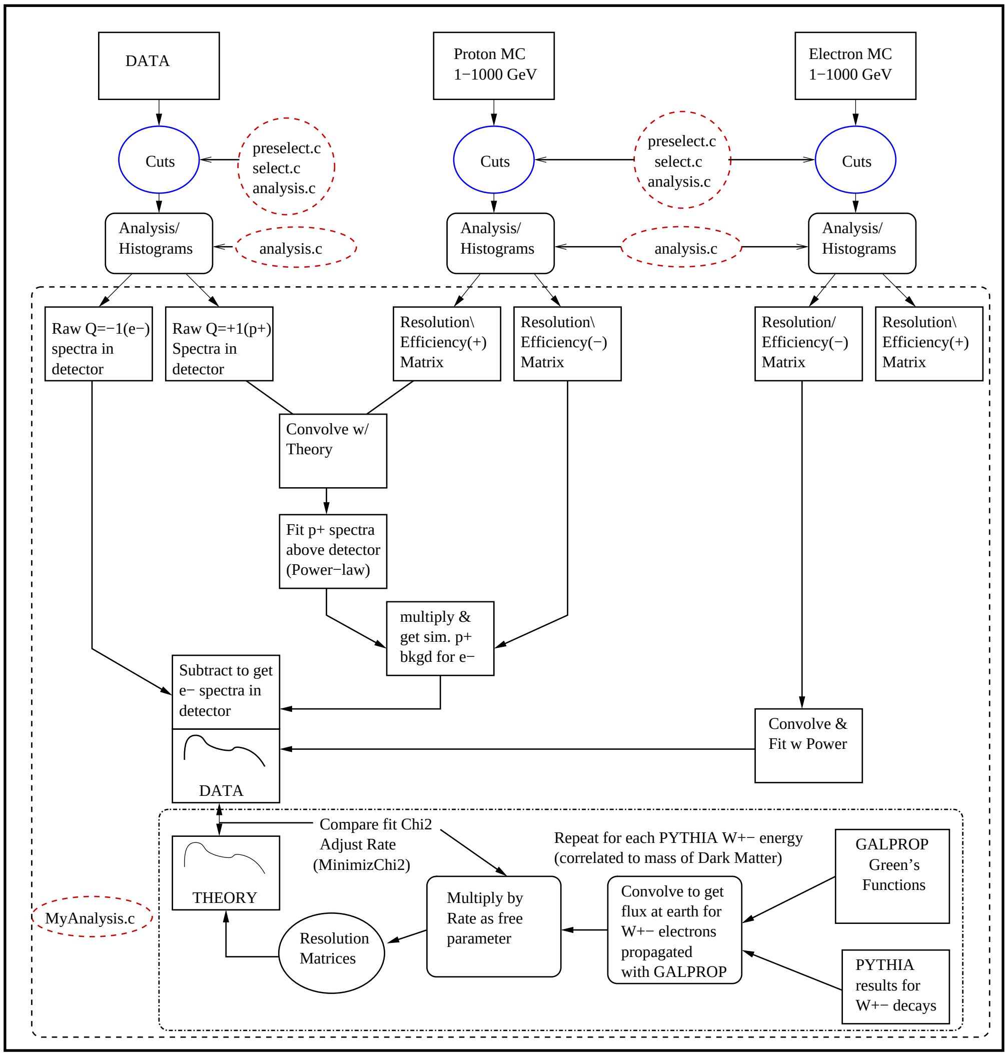

Figure A-1: Analysis Chain

Appendix B

AMS-01 Monte-Carlo Settings

The following is an example of a job file used to set the variables when running the AMS-01 Monte-Carlo.

```
#!/bin/bash
[ -z "\$UNAME" ]      && UNAME=‘(uname) 2>/dev/null‘
[ -z "\$UNAME" -a -d /sys/node_data ] && UNAME="DomainOS"
[ -z "\$UNAME" ]      && (echo could not determine hosttype ; exit)
if [ "\$UNAME" = "AIX" ] ; then
   MACHINE="aix"
elif [ "\$UNAME" = "OSF1" ] ; then
    MACHINE="osf1"
elif [ "\$UNAME" = "Linux" ] ; then
    MACHINE="linux"
else
echo \$UNAME is not supported yet
fi

export AMSDataDir=/net/csraid1/home/rhenning/AMSDataDir
export CERN_ROOT=/lns/cernlib/pro
/net/csraid1/home/rhenning/exe/gbatch.exe > LOGS/1410033.log <<!
LIST
KINE 14
LOSS 1
HADR 1
MULS 1
CUTS 1=0.0005 2=0.0005 3=0.001 4=0.001 5=0.001
TRIG 20000
DEBUG -1 10 1000
C          Nparticles
MCGEN 1=-125. 2=-45. 3=100. 4=125. 5=45. 6=101.
13=1. 14=1000. 15=1 16=0. 17=0. 19=1410033 20=5 21=0
IOPA 1=3 2=’/net/csraid1/home/fisherp/AMS/work/protons’
43=101  45=’TriggerLVL1   ’ 126=30000
L3REC 11=0
RNDM 14 10033
AMSJOB 1=10000 2=0 3=20. 4=0  5=0 46=’AMSSHUTTLE’
TERM=1234567890
END
```

!

Appendix C

AMS-01 Paw Ntuple Structure

The following is a list of elements for each reconstructed particle as written to a PAW ntuple via the AMS-01 reconstruction program. This list is taken from the AMS-01 internal analysis documents.

```
#  \$Id: appc.tex,v 1.1 2005/12/13 16:41:15 gcarosi Exp $
This is AMS01 ntuple description (frozen)
NB : Record Length = 8000
# ! Annotations by bmonreal


 ********************************************
* Type *    Range     *  Block   *  Name    *
 ********************************************
* I*4  *              * EVENTH   * eventno          // Event no    ! The EVENTH block summarizes the contents
* I*4  *              * EVENTH   * run              // run no      ! of this event, and the shuttle/orbit parameters
* I*4  *              * EVENTH   * runtype          //
* I*4  *              * EVENTH   * time(2)          // Event time
                                                    // (1) Unix time (sec)  ! time(1) = absolute time.  T0 = 896849225
                                                    // (2) usec time        ! time(2) resets when AMS-01 daq computer reboots
* I*4  *              * EVENTH   * rawwords         // Event Lenght in bytes
                                                    // (20 low bits, program
                                                    // version (12 high bits)

* R*4  *              * EVENTH   * RadS             // Shuttle Altitude (I2000 cm)
* R*4  *              * EVENTH   * ThetaS           // Shuttle Lattitude (GTOD rad) ! GTOD = Greenwich true-of-date ref frame
* R*4  *              * EVENTH   * PhiS             // Shuttle phi (GTOD rad)
* R*4  *              * EVENTH   * YawS             // Shuttle yaw (LVLH rad) ! see footnote (LVLH = Local Vertical/Local Horizontal ref frame)
* R*4  *              * EVENTH   * PitchS           //         pitch          ! for zenith angle eq.
* R*4  *              * EVENTH   * RollS            //         roll
* R*4  *              * EVENTH   * VelocityS        // Shuttle speed (rad/sec)
* R*4  *              * EVENTH   * VelTheta         // speed theta (GTOD rad)
* R*4  *              * EVENTH   * VelPhi           // speed phi (GTOD rad)
* R*4  *              * EVENTH   * ThetaM           // Magnetic Latitude ***)
* R*4  *              * EVENTH   * PhiM             // Magnetic Longitude ***)

* I*4  *              * EVENTH   * Particles        // No of Particles
* I*4  *              * EVENTH   * Tracks           // No of Tracks
* I*4  *              * EVENTH   * Betas            // No of Betas
* I*4  *              * EVENTH   * Charges          // No of Charges
* I*4  *              * EVENTH   * TrRecHits        // No of 3 dim trackerpoints
* I*4  *              * EVENTH   * TrClusters       // No of Tr Clusters
* I*4  *              * EVENTH   * TrRawClusters    // No of Tr Raw Clusters
* I*4  *              * EVENTH   * TrMCClusters     // No of Tr MC hits
* I*4  *              * EVENTH   * TOFClusters      // No of TOF Clusters
* I*4  *              * EVENTH   * TOFMCClusters    // No of TOF MC Hits
* I*4  *              * EVENTH   * CTCClusters      // No of Cerenkov clusters
* I*4  *              * EVENTH   * CTCMCClusters    // No of Cerenkov MC hits
* I*4  *              * EVENTH   * AntiMCClusters   // No of Anti MC Hits
* I*4  *              * EVENTH   * AntiClusters     // No of Anti clusters
* I*4  *              * EVENTH   * EventStatus      // EventStatus (see status.doc)


* I*4  * [0,10]       * BETA     * nbeta              // betas number
* I*4  *              * BETA     * betastatus         // 4 - ambig
* I*4  *              * BETA     * betapattern(nbeta) // beta pattern(beta.doc)
* R*4  *              * BETA     * beta(nbeta)        // velocity             ! THIS is the velocity.  Note, sometimes > 1
* R*4  *              * BETA     * betac(nbeta)       // corrected velocity  ! this is E.Choumilov's guess at the velocity such that it is always < 1.0
* R*4  *              * BETA     * betaerror(nbeta)   // est error 1/velocity
* R*4  *              * BETA     * betaerrorc(nbeta)  // est error 1/corrected velocity
* R*4  *              * BETA     * betachi2(nbeta)    // chi2 of beta fit(time)
* R*4  *              * BETA     * betachi2s(nbeta)   // chi2 of beta fit(space)
* I*4  *              * BETA     * betantof(nbeta)    // number of tof planes
```

```
* I*4  *               * BETA     * betaptof(4,nbeta)  // pointers to tof planes
* I*4  *               * BETA     * betaptr(nbeta)     // pointer to track


* I*4  * [0,10]        * CHARGE   * ncharge                // charges number
* I*4  *               * CHARGE   * chargestatus           // 1 - refitted
* R*4  *               * CHARGE   * chargebetap(ncharge)   //pointer to velocity
* I*4  *               * CHARGE   * chargetof(ncharge)     // TOF charge
* I*4  *               * CHARGE   * chargetracker(ncharge) // Tracker Charge
* R*4  *               * CHARGE   * probtof(4,ncharge)     // TOF highest Probs
* I*4  *               * CHARGE   * chintof(4,ncharge)     // charge indices for
                                                           // highest Probs (see
                                                           // charge.doc)
* R*4  *               * CHARGE   * probtracker(4,ncharge) // Tracker highest Probs
* I*4  *               * CHARGE   * chintracker(4,ncharge) // charge indices for
                                                           // highest Probs (see
                                                           // charge.doc)
* R*4  *               * CHARGE   * proballtracker(ncharge)// Tracker highest Prob
                                                           // (all hits)
* R*4  *               * CHARGE   * truntof(ncharge)      // Trun (-1) mean (Anodes)
* R*4  *               * CHARGE   * truntofd(ncharge)     // Trun (-1) mean (Dynodes)
* R*4  *               * CHARGE   * truntracker(ncharge) // Trun (-1) mean


* I*4  * [0,10]        * PARTICLE * npart             // particles number   ! The PARTICLE block amasses all of the data
   ! from other blocks and tries to guess what
   ! actual particles are present.  In each array,
   ! the first entry (FORTRAN index 1, C++ ind 0)
     ! contains the "best" particle found in this event.
* I*4  *               * PARTICLE * pbetap(npart)     // pointer to beta
* I*4  *               * PARTICLE * pchargep(npart)   // pointer to charge
* I*4  *               * PARTICLE * ptrackp(npart)    // pointer to track,
                                                      // or -1 if particle doesn't
                                                      // contain a track
* I*4  *               * PARTICLE * pid(npart)        // Geant Particle Id     ! Using the charge and mass, pid(i) is the best guess at the GEANT particle ID
* I*4  *               * PARTICLE * pidvice(npart)    // Geant vice-Particle Id  ! " " second-best guess ""
* R*4  *               * PARTICLE * probpid(2,npart)  // probabilities
* R*4  *               * PARTICLE * fitmom(npart)     // fitted mom for pid
* R*4  *               * PARTICLE * pmass(npart)      // particle mass          ! calculated naively from beta (or betac?) and momentum.
* R*4  *               * PARTICLE * perrmass(npart)   // error in particle mass
* R*4  *               * PARTICLE * pmom(npart)       // particle momentum       ! pmom(i) = ridgidity(ptrackp(i))*sign(beta(pbetap(i)))*pcharge(i).
                                                      //  (signed)
* R*4  *               * PARTICLE * perrmom(npart)    // error in momentum       ! based on rigidity error
* R*4  *               * PARTICLE * pcharge(npart)    // charge                  ! = some combination of chargetracker and chargetof
* R*4  *               * PARTICLE * ptheta(npart)     // theta (1st(last) tracker plane)  ! \ the particle direction
* R*4  *               * PARTICLE * pphi(npart)       // phi  -----------                 ! /
* R*4  *               * PARTICLE * thetagl(npart)    // theta global **)                 ! ???
* R*4  *               * PARTICLE * phigl(npart)      // phi global
* R*4  *               * PARTICLE * pcoo(3,npart)     // coo  -----------       ! location of particle at 1st tracker pl.
* I*4  *               * PARTICLE * atcnbcel(2,npart) // nb of acrossed cells
* R*4  *               * PARTICLE * atcnbphe(2,npart) // nb of photoelectrons
* I*4  *               * PARTICLE * atcidcel(2,npart) // cells id              ****)
* I*4  *               * PARTICLE * atcdispm(2,npart) // PM minimal distance   ****)
* I*4  *               * PARTICLE * atcdaero(2,npart) // Aerogel path length   ****)
* I*4  *               * PARTICLE * atcstatu(2,npart) // Bad ATC cells         ****)
* R*4  *               * PARTICLE * cutoff(npart)     // geomag cutoff in GeV/c    ! A crude calculation - recommend don't use
* R*4  *               * PARTICLE * cooctc(3,2,npart) // tracker extrapol in ctc
* R*4  *               * PARTICLE * cootof(3,4,npart) // tracker extrapol in tof
* R*4  *               * PARTICLE * cooanti(3,2,npart)// tracker extrapol in anti
* R*4  *               * PARTICLE * cootr(3,6,npart)  // tracker extrapol in tr *****) !use this for 3-D position of track
                                                                                 !(interesting to compare to trrh positions)
* I*4  * [0,20]        * TOFCLUST * ntof             // TOF clusters number     !
* I*4  *               * TOFCLUST * TOFStatus(ntof)  // Status:
                                                     // bit 4 - ambig
                                                     // bit 128 -> problems with history
                                                     // bit 256 -> "1-sided" counter   ! this bit flags TOF bars with only one end
                                                     // bit 512 -> bad t-measurement
                                                     //            on one of the sides
                                                     // bit 2048 -> recovered from
                                                     // 1-sided  (bit256 also set)
* I*4  *               * TOFCLUST * plane(ntof)        // Tof layer no       ! with 4 layers and 14 bars per layer,
                                                       //1..4 up..down       ! I assigned a TOF Bar ID as follows:
* I*4  *               * TOFCLUST * bar(ntof)          //  TOF bar no        ! mytofbarid(i) = bar(i) + 14*(plane(i)-1)
* R*4  *               * TOFCLUST * TOFEdep(ntof)      // TOF energy loss (MeV)
                                                       // from Anode
* R*4  *               * TOFCLUST * TOFEdepd(ntof)     // TOF energy loss (MeV)
                                                       // from Dynode
* R*4  *               * TOFCLUST * TOFTime(ntof)      // TOF time (sec)
* R*4  *               * TOFCLUST * TOFETime(ntof)     // Error in TOF time
* R*4  *               * TOFCLUST * TOFCoo(3,ntof)     // TOF Coo (cm)       ! position _along_ bar, I think.
* R*4  *               * TOFCLUST * TOFErCoo(3,ntof)   //
* I*4  *               * TOFCLUST * nmemb(ntof)        // Number of bars in cluster


* I*4  * [0,200]       * TOFMCCLU * ntofmc            // TOF MC hits number
* I*4  *               * TOFMCCLU * TOFMCIdsoft(ntofmc)    // Idsoft
                                                        // Ask E. Choumilov
                                                        // if needed
                                                        //
* R*4  *               * TOFMCCLU * TOFMCXcoo(3,ntofmc)// coo
* R*4  *               * TOFMCCLU * TOFMCtof(ntofmc)   // time
```

```
* R*4  *              * TOFMCCLU * TOFMCedep(ntofmc)  // energy(meV)


* I*4  * [0,50]       * TRCLUSTE * ntrcl              // Tracker clusters number
* I*4  *              * TRCLUSTE * Idsoft(ntrcl)      // Idsoft
                                                      // mod(id,10) layer
                                                      // mod(id/10,100) ladder
                                                      // i=mod(id/1000,10)
                                                      // i==0 x 1st half
                                                      // i==1 x 2nd half
                                                      // i==2 y 1st half
                                                      // i==3 y 2nd half
                                                      // id/10000 strip
* I*4  *              * TRCLUSTE * Statust(ntrcl)     // Status *)
* I*4  *              * TRCLUSTE * NelemL(ntrcl)      // -Number of strips left to max
* I*4  *              * TRCLUSTE * NelemR(ntrcl)      // Number of strips right to max
* R*4  *              * TRCLUSTE * Sumt(ntrcl)        // Amplitude total
* R*4  *              * TRCLUSTE * Sigmat(ntrcl)      // Sigma total
* R*4  *              * TRCLUSTE * Meant(ntrcl)       // CofG (local)
* R*4  *              * TRCLUSTE * RMSt(ntrcl)        // RMS cluster
* R*4  *              * TRCLUSTE * ErrorMeant(ntrcl)  // error in CofG
* R*4  *              * TRCLUSTE * Amplitude(5,ntrcl) // strips ampl


* I*4  * [0,200]      * TRMCCLUS * ntrclmc           // Tracker MC hits number
* I*4  *              * TRMCCLUS * IdsoftMC(ntrclmc) // Idsoft
                                                     // mod(id,10) layer
                                                     // mod(id/10,100) ladder
                                                     // id/1000 sensor
* I*4  *              * TRMCCLUS * Itra(ntrclmc)     // Particle Id (or 555 if noise)
* I*4  *              * TRMCCLUS * Left(2,ntrclmc)   // left strip no
* I*4  *              * TRMCCLUS * Center(2,ntrclmc) // center strip no
* I*4  *              * TRMCCLUS * Right(2,ntrclmc)  // right stip no
* R*4  *              * TRMCCLUS * ss(5,2,ntrclmc)   // Strip amplitudes
* R*4  *              * TRMCCLUS * xca(3,ntrclmc)    // local input coo
* R*4  *              * TRMCCLUS * xcb(3,ntrclmc)    // local output coo
* R*4  *              * TRMCCLUS * xgl(3,ntrclmc)    // global coo
* R*4  *              * TRMCCLUS * summc(ntrclmc)    // total amplitude


* I*4  * [0,200]      * TRRECHIT * ntrrh          // tracker 3dim points number
* I*4  *              * TRRECHIT * px(ntrrh)      // pointer to x track clster
* I*4  *              * TRRECHIT * py(ntrrh)      //  --------  y --------
* I*4  *              * TRRECHIT * statusr(ntrrh) // Status *)
* I*4  *              * TRRECHIT * Layer(ntrrh)   // Layer no 1-6 up-down
* R*4  *              * TRRECHIT * hitr(3,ntrrh)  // gl 3dim coordinates
* R*4  *              * TRRECHIT * ehitr(3,ntrrh) // error to above
* R*4  *              * TRRECHIT * sumr(ntrrh)    // Amplitude
* R*4  *              * TRRECHIT * difosum(ntrrh) // (A_x-A_y)/(A_x+A_y)
* R*4  *              * TRRECHIT * cofgx          //local cfg x
* R*4  *              * TRRECHIT * cofgy          //local cfg y


* I*4  * [0,20]       * TRTRACK  * ntrtr           // tracks number    ! ptrackp(i) points entries in this bank
* I*4  *              * TRTRACK  * trstatus(ntrtr) // Status *)   ! important thing in status: if k-side is not
                                                                  ! reconstructed (matched to TOF), then the chi2 values
                                                          ! are gibberish/meaningless, and the track direction is
                                                                  ! assigned to point through the CENTER of the tof bar
                                                                  ! in the non-bending direction.
* I*4  *              * TRTRACK  * pattern(ntrtr)  // Pattern (datacards.doc) see -> \$\$) at the bottom of the page
* I*4  *              * TRTRACK  * address(ntrtr)  // address (trrec.C buildaddress)
* I*4  *              * TRTRACK  * nhits(ntrtr)    // number of hits        ! note: this is # of hits used, there may be more
                                                                            ! along or near the track.
* I*4  *              * TRTRACK  * phits(6,ntrtr)  // pointers to trrechit
                                                                           ! check that these pointers are valid before
                                                                           ! following them; in a few events they point to
                                                                           ! numbers > ntrrh.  The pointers are in order from
                                                                           ! top to bottom.  If there are only 4 hits, for
                                                                           ! example, phits(5,i) and phits(6,i)=-1.
* R*4  *              * TRTRACK  * LocDbAver(ntrtr) // rel mom from testbeam   ! I don't trust this in TB data
* I*4  *              * TRTRACK  * GeaneFitDone(ntrtr) // != 0 if done
* I*4  *              * TRTRACK  * AdvancedFitDone(ntrtr) --------------
* R*4  *              * TRTRACK  * Chi2StrLine(ntrtr) // chi2 sz fit
* R*4  *              * TRTRACK  * Chi2Circle(ntrtr) // chi2 circular fit
* R*4  *              * TRTRACK  * CircleRidgidity(ntrtr) // circular rigidity
* R*4  *              * TRTRACK  * Chi2FastFit(ntrtr) // chi2 fast nonl fit
* R*4  *              * TRTRACK  * Ridgidity(ntrtr) // fast nonl rigidity  ! This is the best rigidity, most of the time
* R*4  *              * TRTRACK  * ErrRidgidity(ntrtr) // err to 1/above
* R*4  *              * TRTRACK  * Theta(ntrtr) // theta (from fast)     ! theta, phi, and coords appear to be the same
* R*4  *              * TRTRACK  * phi(ntrtr)   // phi ---------         ! as ptheta, pphi, and pcoo in the particle bank
* R*4  *              * TRTRACK  * p0(3,ntrtr)  // coords ----------     !
* R*4  *              * TRTRACK  * gchi2(ntrtr) // geane chi2
* R*4  *              * TRTRACK  * gridgidity(ntrtr)// ------ rigidity   ! this is in principle better, but not always there
* R*4  *              * TRTRACK  * gerrridgidity(ntrtr) //error to 1/above
* R*4  *              * TRTRACK  * gtheta(ntrtr)// -------- theta
* R*4  *              * TRTRACK  * gphi(ntrtr)  // -------- phi
* R*4  *              * TRTRACK  * gp0(3,ntrtr) // ------ coords
* R*4  *              * TRTRACK  * hchi2(2,ntrtr) // two halves chi2s
* R*4  *              * TRTRACK  * HRidgidity(2,ntrtr) //-------- rigities
* R*4  *              * TRTRACK  * HErrRidgidity(2,ntrtr) // errors to 1/above
* R*4  *              * TRTRACK  * htheta(2,ntrtr) // ------- thetas
```

```
* R*4  *              * TRTRACK  * hphi(2,ntrtr) // ------ phis
* R*4  *              * TRTRACK  * hp0(3,2,ntrtr) // ------- coords
* R*4  *              * TRTRACK  * fchi2ms(ntrtr) // fast chi2 mscat off
* R*4  *              * TRTRACK  * pirigerr(ntrtr) // PathInt err(1/rig)
                                               // (<0 means fit wan not succesful)
* R*4  *              * TRTRACK  * ridgidityms(ntrtr) // fast rigidity mscat off
* R*4  *              * TRTRACK  * pirigidity(ntrtr) // PathInt rigidity


* I*4  * [0,20]       * MCEVENTG * nmcg // Number of input particles in MC gen  ******)  !=0 for flight data
* I*4  *              * MCEVENTG * nskip  //Pos no for test beam data or MC spec
* I*4  *              * MCEVENTG * Particle(nmcg) // Geant particle id    ! NOTE: if Particle is negative, that is a secondary
                                                                            ! created in collision/delta-ray/spallation.
                                                                ! Many secondary low-energy electrons are created for most
                                                                ! events; inelastic scatterings are pretty obvious
                                                                ! with multiple hadrons, etc.
   Particle     GEANT ID

   Photon           1
   Positron         2
   Electron         3

   Mu+              5
   Mu-              6
   Pi0              7
   Pi+              8
   Pi-              9
   K0long          10
   K+              11
   K-              12
   Neutron         13
   Proton          14
   Antiproton      15
   K0short         16
   Eta             17
   Lambda          18

   Deuteron        45
   Triton          46
   Alpha           47
   He3             49


* R*4  *              * MCEVENTG * coo(3,nmcg)  // geant particle coos  ! 3-D point where particle was created.
                                                                        ! This is how you can tell if a particle was made
                                                                        ! inside the upper TOF/tracker (likely to affect
                                                                        ! tracking), lower TOF (maybe affect charge?), or below
                                                                        ! that (prob. no affect, unless it comes back to ACC)
* R*4  *              * MCEVENTG * dir(3,nmcg)  // ------- dir cos ! projections of particle direction on x,y,z axes.
* R*4  *              * MCEVENTG * momentum(nmcg) // momentum
* R*4  *              * MCEVENTG * mass(nmcg)   // mass
* R*4  *              * MCEVENTG * charge(nmcg) // charge


* I*4  * [0,20]       * CTCCLUST * nctccl            // cerenkov clusters number
* I*4  *              * CTCCLUST * CTCStatus(nctccl)  // Status *)
* I*4  *              * CTCCLUST * CTCLayer(nctccl)   // layer no
* R*4  *              * CTCCLUST * ctccoo(3,nctccl)   // coords
* R*4  *              * CTCCLUST * ctcercoo(3,nctccl) // errors to above
* R*4  *              * CTCCLUST * ctcrawsignal(nctccl) // raw signals
* R*4  *              * CTCCLUST * ctcsignal(nctccl)  // corrected ones
* R*4  *              * CTCCLUST * ctcesignal(nctccl) // error to above


* I*4  * [0,200]      * CTCMCCLU * nctcclmc    // cerenkov mc hits number
* I*4  *              * CTCMCCLU * CTCMCIdsoft(nctcclmc) // Idsoft
                                                         // Ask E. Choumilov
                                                         // if needed
                                                         //
* R*4  *              * CTCMCCLU * CTCMCXcoo(3,nctcclmc) // coords
* R*4  *              * CTCMCCLU * CTCMCXdir(3,nctcclmc) // dir cos
* R*4  *              * CTCMCCLU * CTCstep(nctcclmc)     // step size (cm)
* R*4  *              * CTCMCCLU * ctccharge(nctcclmc)   // particle charge
* R*4  *              * CTCMCCLU * ctcbeta(nctcclmc)     // velocity
* R*4  *              * CTCMCCLU * ctcedep(nctcclmc)     // energy dep (MeV)


* I*4  * [0,16]       * ANTICLUS * nanti                 // Anti clusters number  ! if >0, event vetoed
* I*4  *              * ANTICLUS * AntiStatus(nanti)     // Status
* I*4  *              * ANTICLUS * AntiSector(nanti)     // Sector no(1-16)
* R*4  *              * ANTICLUS * AntiEdep(nanti)       // Energy dep (MeV)
* R*4  *              * ANTICLUS * AntiCoo(3,nanti)      // Coo (cm)
* R*4  *              * ANTICLUS * AntiErCoo(3,nanti)    // Err to Coo
* I*4  * [0,200]      * ANTIMCCL * nantimc               // MC Anti hits number
* I*4  *              * ANTIMCCL * AntiMCIdsoft(nantimc) // idsoft
* R*4  *              * ANTIMCCL * AntiMCXcoo(3,nantimc) // coo
* R*4  *              * ANTIMCCL * AntiMCtof(nantimc)    // Tof
* R*4  *              * ANTIMCCL * AntiMCedep(nantimc)   // energy dep (GeV)
```

```
* I*4  * [0,2]       * LVL3     * nlvl3                  // lvl3trigger number  ! NLVL3 sometimes=2.  If so, the i=1 version
                                                                               !  is that reported by the hardwarde, the i=2
                                                                               ! version is that reported by the software.
                                                                               ! I think.  Also, keep in mind that MC has NO
                                                                               ! TRIGGERS APPLIED - run xtrig.f to learn how
                                                                               ! the event would trigger or not.

* I*4  *             * LVL3     * LVL3TOFTr(nlvl3)       // TOF Trigger
                                          // -1 if rejected by matrix trigger,
                                          // 0 if rejected by adj hits, 1 otherwise
* I*4  *             * LVL3     * LVL3AntiTr(nlvl3)  // Anti Trigger  not used now
* I*4  *             * LVL3     * LVL3TrackerTr(nlvl3)  // TrackerTrigger      ! Tracker trigger turned on only before
                                                        // 0  - initial state  ! MIR docking.  To see when the trigger
                                                        // 1  - reject (p)     ! was turned on, look for non-consecutive
                                                        // 2  - Too many hits  ! "eventno".
                                                        // 3  - No comb found
                                                        // 4  - >=2 comb found
                                                        // 5  - Reserved
                                                        // 6  - Reserved
                                                        // 7  - Accept (ap)
                                                        //+8  - Heavy Ion
                                                        //+32 - Prescaled evts
* I*4  *             * LVL3     * LVL3NTrHits(nlvl3)    // Number Tr Hits
* I*4  *             * LVL3     * LVL3NPat(nlvl3)       // Number "Tracks" found
* I*4  *             * LVL3     * LVL3Pattern(2,nlvl3)  // Pattern no
* R*4  *             * LVL3     * LVL3Residual(2,nlvl3) // Aver Residual (cm)
* R*4  *             * LVL3     * LVL3Time(nlvl3)       // Alg Time (sec)
* R*4  *             * LVL3     * LVL3ELoss(nlvl3)      // Aver energy loss


* I*4  * [0,1]       * LVL1     * nlvl1                 // lvl1trigger number  ! See NLVL3 note: run xtrig.f to get the
* I*4  *             * LVL1     * LVL1LifeTime(nlvl1)   // DAQLifeTime *1000   ! actual trigger flags.
                                                        // + 10000* (sum tof
                                                        // temperatutes (8 crates)
* I*4  *             * LVL1     * LVL1Flag(nlvl1)       // z from trigger +4/4?10:0
* I*4  *             * LVL1     * LVL1TOFPatt(4,nlvl1)  // tof pattern
                                                        // 0-13 bit  or
                                                        // 16-29    and
                                                        // 31       plane not
                                                        // in trigger (MC)
* I*4  *             * LVL1     * LVL1TOFPatt1(4,nlvl1) // Tof pattern z>1
                                                        // -------------
* I*4  *             * LVL1     * LVL1AntiPatt(nlvl1)   // antipattern
                                                        // 16-23 bits
                                                        // as in daqevt.doc


* I*4  * [0,50]      * CTCHIT   * nctcht                // CTC Hits number
* I*4  *             * CTCHIT   * CTChitStatus(nctcht)  //  ----  status
* I*4  *             * CTCHIT   * CTChitLayer(nctcht)   //        layer
* I*4  *             * CTCHIT   * ctchitcolumn(nctcht)  //        column(x)
* I*4  *             * CTCHIT   * ctchitrow(nctcht)     //        row(y)
* R*4  *             * CTCHIT   * ctchitsignal(nctcht)  //        signal (pe)


* I*4  * [0,500]     * TRRAWCL  * ntrraw                // trrawcl num
* I*4  *             * TRRAWCL  * rawaddress(ntrraw)    // see TRCLUSTE Idsoft
* I*4  *             * TRRAWCL  * rawlength(ntrraw)     //  rawcl length
* R*4  *             * TRRAWCL  * s2n(ntrraw)           // s/n for seed


* I*4  * [0,32]      * ANTIRAWC * nantiraw                  // antirawcl num
* I*4  *             * ANTIRAWC * antirawstatus(nantiraw)   // status
* I*4  *             * ANTIRAWC * antirawsector(nantiraw)   //sector 1-16
* I*4  *             * ANTIRAWC * antirawupdown(nantiraw)   //0 - up 1 -down
* R*4  *             * ANTIRAWC * antirawsignal(nantiraw)   // (mev)


* I*4  * [0,20]      * TOFRAWCL * ntofraw                   // tofrawclnum (used)  !
* I*4  *             * TOFRAWCL * tofrstatus(ntofraw)       // status
* I*4  *             * TOFRAWCL * tofrplane(ntofraw)        // tof plane1-4
* I*4  *             * TOFRAWCL * tofrbar(ntofraw)          // tof bar 1-14
* R*4  *             * TOFRAWCL * tofrtovta(2,ntofraw)      // anode time      ! If you want to see individual TOF
                                                            //over_thresh (ns) ! ends, look here. toftrovta=0 if end d/n fire.
* R*4  *             * TOFRAWCL * tofrtovtd(2,ntofraw)      // dinode time
                                                            //over_thresh (ns)
* R*4  *             * TOFRAWCL * tofrsdtm(2,ntofraw)       // A-noncorrected
                                                            //  side times
* R*4  *             * TOFRAWCL * tofreda(ntofraw)       // Edep-A (mev)
* R*4  *             * TOFRAWCL * tofredd(ntofraw)       // Edep-D (mev)
* R*4  *             * TOFRAWCL * tofrtm(ntofraw)        // Time (ns)
* R*4  *             * TOFRAWCL * tofrcoo(ntofraw)       // Long.coord.(cm)



----------------------------------------------------------------------------

*) Status bits (counting from 1 to 32)

 1 - REFITTED object                                     (status&1     !=0)
```

```
 2 - WIDE in shape (Tracker)                             (status&2     !=0)
 3 - AMBIGously associated                               (status&4     !=0)
 4 - RELEASED object                                     (status&8     !=0)
 5 - BAD                                                 (status&16    !=0)
 6 - USED as a component of a larger object              (status&32    !=0) #    <-
 7 - DELETED object                                      (status&64    !=0)
 8 - BADHIStory (TOF)                                    (status&128   !=0)
 9 - ONESIDE measurement (TOF)                           (status&256   !=0)
10 - BADTIME information (TOF)                           (status&512   !=0)
11 - NEAR, close to another object (Trck)                (status&1024  !=0)
12 - WEAK, defined with looser criteria (Trck)           (status&2046  !=0)
13 - AwayTOF, away from TOF predictions (Trck)           (status&4096  !=0)
14 - FalseX, x-coordinate built but not measured (Trck)  (status&8192  !=0) # <-Uses 3 hit track to generate false K-side clusters in other ladders
15 - FalseTOFX, x-coordinates from TOF (Trck)            (status&16384 !=0) # <-Uses TOF straightline fit to generate K-side clusters
16 - 4th tof plane was recovered using tracker           (status&32768 !=0)
17 - LocalDB was used to align track                     (status&65536 !=0)
18 - GlobalDB was used to align the track                (status&(65536*2)!=0)   <-
19 - Cluster was used to get the charge                  (status&(65536*4)!=0)
20 - TrRecHit was good enough to be used in track find   (status&(65536*8)!=0) #
21 - Track->Trladder interpol was done on plane level    (status&(65536*16)!=0)
22 - Track was created using TOF only                    (status&(65536*32)!=0)
23 - Object Overflow                                     (status&(65536*64)!=0)
**) AMS global system definition :
GTOD


***) Shuttle coordinates in an eccentric dipole coordinate system where
     GEOMz=-d, GEOMy=GEOMz x S  (d: dipole direction, S: geographic South)


****) The ATC information can be decoded through the following scheme
      for the plane k (k=1,2)

      cells ID:            mod(atcidcel(k)/10**(2*i-2),100)     (i=1,nb cells)
      aerogel path:        mod(atcdaero(k)/10**(2*i-2),100)/10. (i=1,nb cells)
      PM impact parameter: mod(atcdispm(k)/10**(2*i-2),100)/10. (i=1,nb cells)
      bad cells:
           plane 1 - mod(atcstatu(1)/10**(2*i-1),100)     (i=1,mod(atcstatu(1),10))
           plane 2 - mod(atcstatu(2)/10**(2*i-1),100)+80  (i=1,mod(atcstatu(2),10))
                           Cells 166 and 168 are allways dead (dead channell)
                           Cell 175 means module L5

\$\$)Tracker Pattern:

pattern[ptrackp[0]-1]: Layers with hits used

0:   1 2 3 4 5 6
1:   1 2 3 4   6
2:   1 2 3   5 6
3:   1 2   4 5 6
4:   1   3 4 5 6
5:   1 2 3 4 5
6:     2 3 4 5 6
7:   1 2 3 4
8:   1 2 3   5
9:   1 2 3     6
10:  1 2   4 5
11:  1 2   4   6
12:  1 2     5 6
13:
14:  1   3 4   6
15:  1   3   5 6
16:
17:    2 3 4 5
18:    2 3 4   6
19:    2 3   5 6
20:    2   4 5 6
21:      3 4 5 6

Addendum (V.Choutko + F.Barao) : The code below should do the job

         subroutine decatc(iflag,path,pimpact)
*
* Input   from paw common
*
* Output
*        iflag : 0 ok; 1,2,3 bad
*        path : famous path
*        pimpact : distance to pm
*        Note: path & pimpact  are calculated only if iflag==0

         iflag=0
         path=0
         pimpact=10000
         do i=1,2
          do k=1,atcnbcel(i,1)
           idc=mod(atcidcel(i,1)/10**(2*k-2),100)+80*(i-1)
           if(idc.eq.166.or.idc.eq.168)then
            iflag=3
            return
           endif
```

```
           path=path+   mod(atcdaero(i,1)/10**(2*k-2),100)/10.
           pil=mod(atcdispm(i,1)/10**(2*k-2),100)/10.
           if(pimpact.gt.pil)pimpact=pil
           ibad=mod(atcstatu(i,1),10)
           do l=1,ibad
             if(mod(atcstatu(i,1)/10**(2*l-1),100)+80*(i-1).eq.175)then
               if (idc/16+1.eq.10) then
                  iflag=2
                  return
               endif
             endif
             if(idc.eq.mod(atcstatu(i,1)/10**(2*l-1),100)+80*(i-1))then
              iflag=1
              return
             endif
           enddo
          enddo
         enddo
         end
```

```
*****) Changed from build=101

cootr(3,1:nlay(),npart) now contains the minimal distance to sensor edge
in sensor length units;



******) geant3 only  particle=pid+256 means heavy ion nonelstic scattering occured
        in for pid with dir & momentum at coo; particle=-pid means secondary
        particle produced with dir&momentum at coo




*******) For geant4 this value is 0. For geant 3it has several meanings:

Cerenkov photon generated in radiator:

    ricstatus = 100*(mother of Cerenkov if secondary?1:0)+10*(number of
                reflections in mirror) + (photon suffered rayleigh
                scattering?1:0)

PMT noise:

    ricstatus = -1


Cerenkov photon generated in PMT window:

    ricstatus = -(2+100*(mother of Cerenkov if secondary?1:0))

No Cerenkov photon:

    ricstatus = -(3+100*(mother of Cerenkov if secondary?1:0))

NOTE: The information of the mother is only available if RICCONT=1 in the datacards
```

Appendix D

GALPROP Settings

The following is an example of a galdef file used to set the variables when running GALPROP. This examples runs a set of electrons with source strength of 10^6 and a delta function of energy 112 MeV $= 10^{2.05}$ MeV, which is the center of the energy bin from $10^{2.0} - 10^{2.1}$. The center of each energy bin up to a TeV was run in order to simplify the convolution with the results from PYTHIA.

```
1234567890123456789012
======================value
Title                = Production version, electrons, run 800102, 112.
n_spatial_dimensions = 3 *
r_min               =00.0     min r
r_max               =30.0     max r
dr                  =10.0     delta r
z_min               =-4.0    min z
z_max               =+4.0    max z
dz                   = 4.0   delta z

x_min                =  0.0   min x
x_max                =+20.0   max x
dx                   = 0.5    delta x
y_min                =  0.0   min y
y_max                =+20.0   max y
dy                   = 0.5    delta y

p_min               =100.     min momentum (MV)
p_max               =1000000.     max momentum
p_factor            =1.259         momentum factor

Ekin_min            =1.0e2   min kinetic energy per nucleon (MeV)
Ekin_max            =1.0e7   max kinetic energy per nucleon
Ekin_factor         =1.259      kinetic energy per nucleon factor

p_Ekin_grid          = Ekin         p||Ekin alignment

E_gamma_min          = 1.e0   min gamma-ray energy (MeV)
E_gamma_max          = 1.e7    max gamma-ray energy (MeV)
E_gamma_factor       = 1.259     gamma-ray energy factor
```

```
nu_synch_min         = 1.0e6   min synchrotron frequency (Hz)
nu_synch_max         = 1.0e10  max synchrotron frequency (Hz)
nu_synch_factor      = 4.0         synchrotron frequency factor

long_min             =  0.5    gamma-ray intensity skymap longitude minimum (deg)
long_max            =359.5    gamma-ray intensity skymap longitude maximum (deg)
lat_min             =-89.5    gamma-ray intensity skymap latitude  minimum (deg)
lat_max             =+89.5    gamma-ray intensity skymap latitude  maximum (deg)
d_long               =  1.     gamma-ray intensity skymap longitude binsize (deg)
d_lat                =  1.     gamma-ray intensity skymap latitude  binsize (deg)

D0_xx               =3.30e28  diffusion coefficient at reference rigidity
D_rigid_br          =3.0e3    reference rigidity for diffusion coefficient in MV
D_g_1                = 0.47    diffusion coefficient index below reference rigidity
D_g_2                = 0.47    diffusion coefficient index above reference rigidity
diff_reacc          =1        1=include diffusive reacceleration
v_Alfven            =23.      Alfven speed in km s-1

convection           =0        1=include convection
v0_conv              =0.       km s-1        v_conv=v0_conv+dvdz_conv*dz
dvdz_conv            =10.      km s-1 kpc-1  v_conv=v0_conv+dvdz_conv*dz

nuc_rigid_br         =1.e3     reference rigidity for nucleus injection index in MV
nuc_g_1              =2.28     nucleus injection index below reference rigidity
nuc_g_2              =2.28     nucleus injection index index above reference rigidity

inj_spectrum_type    = beta_rig     rigidity||beta_rig||Etot nucleon injection spectrum type

electron_rigid_br    =1.0e3    reference rigidity for electron injection index in MV
electron_g_1         =2.40     electron injection index below reference rigidity
electron_g_2         =2.40     electron injection index index above reference rigidity

He_H_ratio           =0.11     He/H of ISM, by number
X_CO                 =1.9E20   conversion factor from CO integrated temperature
                               to H2 column density
fragmentation        =1        1=include fragmentation
momentum_losses      =1        1=include momentum losses
radioactive_decay    =1        1=include radioactive decay
K_capture            =0        1=include K-capture

start_timestep       =1.0e7
  end_timestep       =1.0e1
timestep_factor      =0.25
timestep_repeat      =20    number of repeats per timestep in  timetep_mode=1
timestep_repeat2     =0     number of timesteps in timetep_mode=2
timestep_print       =1000   number of timesteps between printings
timestep_diagnostics =10000  number of timesteps between diagnostics
control_diagnostics  =0      control detail of diagnostics

network_iterations   =1      number of iterations of entire network

prop_r               = 1  1=propagate in r (2D)
```

```
prop_x               = 1  1=propagate in x (2D,3D)
prop_y               = 1  1=propagate in y (3D)
prop_z               = 0  1=propagate in z (3D)
prop_p               = 1  1=propagate in momentum

use_symmetry         = 1  0=no symmetry, 1=optimized symmetry, 2=xyz symmetry by copying(3D)

vectorized           = 0  0=unvectorized code, 1=vectorized code

source_specification = 1  2D::1:r,z=0 2:z=0  3D::1:x,y,z=0 2:z=0 3:x=0 4:y=0 *
source_model         = 1  0=zero 1=parameterized  2=Case&B 3=pulsars 4= 5=S&Mattox
                          6=S&Mattox with cutoff
source_parameters_1  = 0.5    model 1:alpha
source_parameters_2  = 1.0    model 1:beta
source_parameters_3  = 20.0   model 1:rmax


n_cr_sources         = 0     number of pointlike cosmic-ray sources   3D only!
cr_source_x_01       = 10.0  x position of cosmic-ray source 1 (kpc)
cr_source_y_01       = 10.0  y position of cosmic-ray source 1
cr_source_z_01       = 0.1   z position of cosmic-ray source 1
cr_source_w_01       = 0.1 sigma width  of cosmic-ray source 1
cr_source_L_01       = 10000.0   luminosity of cosmic-ray source 1
cr_source_x_02       = 3.0   x position of cosmic-ray source 2
cr_source_y_02       = 4.0   y position of cosmic-ray source 2
cr_source_z_02       = 0.2   z position of cosmic-ray source 2
cr_source_w_02       = 2.4 sigma width  of cosmic-ray source 2
cr_source_L_02       = 2.0   luminosity of cosmic-ray source 2


SNR_events           = 0    handle stochastic SNR events
SNR_interval         = 1.0e4 time interval in years between SNR in 1 kpc^-3 volume
SNR_livetime         = 1.0e4 CR-producing live-time in years of an SNR
SNR_electron_sdg     = 0.00      delta electron source index Gaussian sigma
SNR_nuc_sdg          = 0.00      delta nucleus  source index Gaussian sigma
SNR_electron_dgpivot = 5.0e3     delta electron source index pivot rigidity (MeV)
SNR_nuc_dgpivot      = 5.0e3     delta nucleus  source index pivot rigidity (MeV)

elect_delta_source   = 1000000.
elect_delta_energy   = 112.
elect_delta_x        = 0.
elect_delta_y        = 0.
elect_delta_z        = 0.
elect_delta_mode     = 0

posit_delta_source   = 0.
posit_delta_energy   = 0.
posit_delta_mode     = 0.

B_field_model        = 050100020   bbbrrrzzz    bbb=10*B(0)  rrr=10*rscale zzz=10*zscale

proton_norm_Ekin     = 1.00e+5 proton kinetic energy for normalization (MeV)
proton_norm_flux     = 4.95e-9 flux of protons at normalization energy
```

```
                       (cm^-2 sr^-1 s^-1 MeV^-1)

electron_norm_Ekin   = 3.45e4  electron kinetic energy for normalization (MeV)
electron_norm_flux   = 4.0e-10 flux of electrons at normalization energy
                       (cm^-2 sr^-1 s^-1 MeV^-1)

max_Z                = 2      maximum number of nucleus Z listed
use_Z_1              = 1
use_Z_2              = 1
use_Z_3              = 1
use_Z_4              = 1
use_Z_5              = 1
use_Z_6              = 1
use_Z_7              = 1
use_Z_8              = 1
use_Z_9              = 1
use_Z_10             = 1
use_Z_11             = 0
use_Z_12             = 0
use_Z_13             = 0
use_Z_14             = 0
use_Z_15             = 0
use_Z_16             = 0
use_Z_17             = 0
use_Z_18             = 0
use_Z_19             = 0
use_Z_20             = 0
use_Z_21             = 0
use_Z_22             = 0
use_Z_23             = 0
use_Z_24             = 0
use_Z_25             = 0
use_Z_26             = 0
use_Z_27             = 0
use_Z_28             = 0
use_Z_29             = 0
use_Z_30             = 0

iso_abundance_01_001 = 1.054e6        H  relative isotopic abund. within element as
iso_abundance_02_004 = 0.803e5        He in solar system Anders, E., & Grevesse, M.
iso_abundance_03_006 =    0.          Li Geochim. Cosmochin. Acta 1989, 53, 197
iso_abundance_04_009 =    0.          Be
iso_abundance_05_010 =    0.          B
iso_abundance_06_012 = 2817.7         C
iso_abundance_06_013 =   34.2
iso_abundance_07_014 =  207.6         N
iso_abundance_07_015 =    0.8
iso_abundance_08_016 = 3651.          O
iso_abundance_08_017 =    1.5
iso_abundance_08_018 =    8.4
iso_abundance_09_019 =    0.5         F
iso_abundance_10_020 =  382.1         Ne
iso_abundance_10_021 =    1.2
```

```
iso_abundance_10_022 =   51.2
iso_abundance_11_023 =   24.6         Na
iso_abundance_12_024 =  570.5         Mg
iso_abundance_12_025 =   76.7
iso_abundance_12_026 =   87.8
iso_abundance_13_027 =   55.0         Al
iso_abundance_14_028 =  641.4         Si
iso_abundance_14_029 =   33.9
iso_abundance_14_030 =   23.
iso_abundance_15_031 =    7.17        P
iso_abundance_16_032 =   92.61        S
iso_abundance_16_033 =    0.76
iso_abundance_16_034 =    4.36
iso_abundance_16_036 =    0.01
iso_abundance_17_035 =    1.84        Cl
iso_abundance_17_037 =    0.63
iso_abundance_18_036 =   10.68        Ar
iso_abundance_18_038 =    2.12
iso_abundance_19_039 =    3.70        K
iso_abundance_20_040 =   38.7         Ca
iso_abundance_20_042 =    0.3
iso_abundance_20_044 =    0.9
iso_abundance_20_048 =    0.09
iso_abundance_21_045 =    0.068       Sc
iso_abundance_22_046 =    0.17        Ti
iso_abundance_22_047 =    0.16
iso_abundance_22_048 =    1.60
iso_abundance_22_049 =    0.12
iso_abundance_22_050 =    0.12
iso_abundance_23_051 =    0.0         V  0.7
iso_abundance_24_050 =    0.72        Cr
iso_abundance_24_052 =   14.49            12
iso_abundance_24_053 =    1.69
iso_abundance_24_054 =    0.43
iso_abundance_25_055 =   16.21        Mn
iso_abundance_26_054 =   37.95        Fe
iso_abundance_26_056 =  619.8
iso_abundance_26_057 =   15.06
iso_abundance_26_058 =    2.31
iso_abundance_27_059 =    1.25        Co
iso_abundance_28_058 =   26.19        Ni
iso_abundance_28_060 =   10.43
iso_abundance_28_061 =    0.48
iso_abundance_28_062 =    1.50
iso_abundance_28_064 =    0.46

total_cross_section  = 0  total cross section option: 0=L83 1=WA96 2=BP01
cross_section_option = 011    100*i+j  i=1: use Heinbach-Simon C,O->B j=kopt j=11=Webber, 21=ST

t_half_limit         =    1.0e4 year - lower limit on radioactive half-life for
                                       explicit inclusion

primary_electrons    = 1
```

```
secondary_positrons  = 1
secondary_electrons  = 1
secondary_antiproton = 1
tertiary_antiproton  = 1
secondary_protons    = 1

gamma_rays           = 0    1=compute gamma rays
IC_anisotropic       = 0    1=compute anisotropic IC
synchrotron          = 0    1=compute synchrotron

output_gcr_full      = 0  output full galactic cosmic ray array
warm_start           = 0  read in nuclei file and continue run

verbose              = 0        verbosity: 0=min,10=max <0: selected debugs
test_suite           = 0  run test suite instead of normal run
```

Bibliography

[1] Committee on the Physics of the Universe. Connecting Quarks with the Cosmos: Eleven Science Questions for the New Century. Technical report, National Research Council of the National Academies, 2003.

[2] F. Zwicky. On the Masses of Nebulae and of Clusters of Nebulae. *Helvetica Physica Acta*, 1933.

[3] D.N. Spergel et. al. First-Year Wilkinson Microwave Anisotropy Probe (WMAP) Observations: Determination of Cosmological Parameters. *Astrophysical Journal Supplement Series*, 148(1):175–194, 2003.

[4] Gerad Jungman, Marc Kamionkowski, and Kim Griest. Supersymmetric Dark Matter. *Physics Reports*, 267:195–373, 1996.

[5] H. Cheng, J.L. Feng, and K.T. Matchebv. Kaluza-Klein Dark Matter. *Physical Review Letters*, 89(21):1301(4), November 2002.

[6] Benjamin W. Lee and Steven Weingberg. Cosmological Lower Bound on Heavy-Neutrino Masses. *Physical Review Letters*, 39(4):165–168, July 1977.

[7] L. Zhang and K.S. Cheng. Cosmic-ray positrons from mature gamma-ray pulsars. *Astronomy and Astrophysics*, 368:1063–1070, 2001.

[8] HEAT Collaboration. New Measurement of the Cosmic-Ray Positron Fraction from 5 to 15 GeV. *Physical Review Letters*, 93(24):1102(4), December 2004.

[9] M. Kamionkowski and M.S. Turner. Distinctive positron feature from particle dark-matter annihilations in the galactic halo. *Physical Review D*, 43(6):1774–1780, March 1991.

[10] Torbjörn Sjöstrand et al. High-energy-physics event generation with PYTHIA 6.1. *Computer Physics Communications*, 135:238–259, 2001.

[11] Igor V. Moskalenko and Andrew W. Strong. GALPROP C++ v.41: Explanatory Supplement. Description of Code, 2000.

[12] K.G. Begeman, A.H. Broeils, and R.H. Sanders. Extended Rotation Curves of Spiral Galaxies - Dark Haloes and Modified Dynamics. *Royal Astronomical Society, Monthly Notices*, 249:523–537, April 1991.

[13] D. Zaritsky. The Mass of Spiral Galaxy Halos. *Publications of the Astronomical Society of the Pacific*, 104:831–834, September 1992.

[14] J.A. Tyson. Mapping Cosmic Dark Matter. In *Proceedings of Snowmass 1994: Particle and Nuclear Astrophysics and Cosmology in the Next Millennium Symposium on the Theory of Computing*, 1995.

[15] U.G. Briel, J.P. Henry, and H. Bohringer. Observations of the Coma cluster of galaxies with ROSAT during the All-Sky Survey. *Astron. Astrophys.*, 259:L31–L34, 1992.

[16] R. Minchin et al. A Dark Hydrogen Cloud in the Virgo Cluster. *The Astrophysical Journal*, 622:L21–L24, March 2005.

[17] Particle Data Group. Review of Particle Physics: Dark Matter. *Physics Letters B*, 592:216–220, 2004.

[18] R. Bradley et. al. Microwave cavity searches for dark-matter axions. *Review of Modern Physics*, 75:777–817, July 2003.

[19] Donald Perkins. *Particle Astrophysics*, volume 1 of *Oxford Master Series in Particle Physics, Astrophysics, and Cosmology*, section 4.8, pages 106–108. Oxford University Press, Oxford, UK, first edition, 2003.

[20] P.L. Schecter and J.D. Schnittman. The Physics of Galaxies and the Universe. Lecture Notes: MIT 8.902, 2005.

[21] Paolo Gondolo. Either neutralino dark matter or cuspy dark halos. *Physics Letters B*, 494:181–186, 2000.

[22] V. Berezinksy, V. Dokuchaev, and Y. Eroshenko. Small-scale clumps in the galactic halo and dark matter annhilation. *Physical Review D*, 68:103003(19), 2003.

[23] J. Diemand, B. Moore, and J. Stadel. Earth-mass dark-matter haloes as the first structures in the early Universe. *Nature*, 433:389–391, January 2005.

[24] Lars Bergström. Non-Baryonic Dark Matter: Observational Evidence and Detection Methods. *Reports on Progress in Physics*, 63(5):793–841, May 2000.

[25] CDMS Collaboration. First Results from the Cryogenic Dark Matter Search in the Soudan Underground Lab. *Physical Review Letters*, 93(21):211301(5), November 2004.

[26] DAMA Collaboration. On a further search for a yearly modulation of the rate in particle Dark Matter direct search. *Physics Letters B*, 450:448–455, March 1999.

[27] EDELWEISS Collaboration. Improved exclusion limits from the EDELWEISS WIMP search. *Physics Letters B*, 545:43–49, July 2002.

[28] MACRO Collaboration. Limits on dark matter WIMPs using upward-going muons in the MACRO detector. *Physical Review D*, 60:082002–082012, 1999.

[29] EGRET Collaboration. Evidence for a Galactic gamma-ray halo. *New Astronomy*, 3:539–561, 1998.

[30] Ferrer Francesc. TeV Dark Matter detection by Atmospheric Cerenkov Telescopes. In *2005 Moriond Workshop: Very High Energy Phenomena in the Universe*, 2005.

[31] S. Orito et al. Precision Measurements of Cosmic-Ray Antiproton Spectrum. *Physical Review Letters*, 84(6):1078–1081, February 2000.

[32] Malcolm S. Longair. *Particles, photons and their detection*, volume 1 of *High Energy Astrophysics*, section 9, pages 270–296. Cambridge University Press, Cambridge, UK, second edition, 1994.

[33] Particle Data Group. Review of Particle Physics: Cosmic Rays. *Physics Letters B*, 592:228–234, 2004.

[34] S. Torii et. al. The Energy Spectrum of Cosmic-ray Electrons from 10 to 100 GeV Observed with a Highly Granulated Imaging Calorimeter. *The Astrophysical Journal*, 559:973–984, October 2001.

[35] S.W. Barwick et. al. The Energy Spectra and Relative Abundances of Electrons and Positrons in the Galactic Cosmic Radiation. *The Astrophysical Journal*, 498(2):779–789, May 1998.

[36] J. Nishimura et al. Emulsion Chamber Observations of Primary Cosmic-Ray Electrons in the Energy Range 30-1000 GeV. *The Astrophysical Journal*, 238:394–409, May 1980.

[37] R.L. Golden et al. A Measurement of the Absolute Flux of Cosmic-Ray Electrons. *The Astrophysical Journal*, 287:622–632, December 1984.

[38] K.K. Tang et al. The Energy Spectrum of Electrons and Cosmic-Ray Confinement: A New Measurement and its Interpretation. *The Astrophysical Journal*, 278:881–892, March 1984.

[39] R.L. Golden et al. Observations of Cosmic-Ray Electrons and Positrons Using an Imaging Calorimeter. *The Astrophysical Journal*, 436:769–775, December 1994.

[40] I.V. Moskalenko and A.W. Strong. Production and Propagation of Cosmic-Ray Positrons and Electrons. *The Astrophysical Journal*, 493:694–707, 1998.

[41] H.V. Klapdor-Kleingrothaus and K. Zuber. *Particle Astrophysics*, section 8.2, pages 242–247. Institute of Physics Publishing, Cambridge, UK, 1997.

[42] Donald Perkins. *Particle Astrophysics*, volume 1 of *Oxford Master Series in Particle Physics, Astrophysics, and Cosmology*, section 6.3, pages 155–157. Oxford University Press, Oxford, UK, first edition, 2003.

[43] Enrico Fermi. On the Origin of the Cosmic Radiation. *Physical Review*, 75(8):1169–1174, April 1949.

[44] Roger Blandford and David Eichler. Particle Acceleration at Astrophysical Shocks: A Theory of Cosmic Ray Origins. *Physics Reports*, 154:1–75, 1987.

[45] Guy Pelletier. Fermi Acceleration of Astroparticles. *Lecture Notes in Physics*, 576:58–89, 2001.

[46] R.D. Blandford and J.P. Ostriker. Particle Acceleration by Astrophysical Shocks. *The Astrophysical Journal*, 221:L29–L32, April 1978.

[47] T.K. Gaisser. *Cosmic Rays and Particle Physics*, section 9, pages 115–126. Cambridge University Press, Cambridge, UK, 1990.

[48] Ben Monreal. *Search for microquasar features in cosmic ray spectra with AMS-01*. PhD dissertation, Massachusetts Institute of Technology, Physics Department, May 2004.

[49] Malcolm S. Longair. *Stars, the Galaxy and the interstellar medium*, volume 2 of *High Energy Astrophysics*, section 19, pages 274–301. Cambridge University Press, Cambridge, UK, second edition, 1994.

[50] I.V. Moskalenko and A.W. Strong. Propagation of Cosmic-Ray Nucleons in the Galaxy. *The Astrophysical Journal*, 509:212–228, 1998.

[51] Donald Perkins. *Particle Astrophysics*, volume 1 of *Oxford Master Series in Particle Physics, Astrophysics, and Cosmology*, section 6.2, pages 152–155. Oxford University Press, Oxford, UK, first edition, 2003.

[52] American Institute of Physics. Physics News Graphics: East-West Neutrino Asymmetry. `http://www.aip.org/png/html/eastwest.html`. (3 January 2006).

[53] M. Aguilar et al. (AMS Collaboration). The Alpha Magnetic Spectrometer (AMS) on the International Space Station: Part I - Results from the Test Flight on the Space Shuttle. *Physics Reports*, 366(6):331–405, 2002.

[54] Reyco Henning. *Search for Antideuterons and Strangelets in Cosmic Rays with AMS-01*. PhD dissertation, Massachusetts Institute of Technology, Department of Physics, September 2003.

[55] S. Ahlen et al. An Antimatter Spectrometer in Space. *Nuclear Instruments and Methods A*, 350:351–367, 1994.

[56] Vitaly Choutko. Selected AMS01 Reconstruction Software Issues. AMS Internal Presentation, January 2003.

[57] J. Alcaraz et al. A Silicon microstrip tracker in space: Experience with the AMS silicon tracker on STS-91. *Il Nouvo Cimento*, 112A(11):1325–1344, 1999.

[58] L. Baldini et al. The AMS-01 Time of Flight System. In *7th Int. Conf. on Advanced Technology and Particle Physics*, 2001.

[59] F. Mayet. Performance Results of the AMS-01 Aerogel Threshold Cerenkov. In *XIth Rencontres de Blois (Frontiers of Matter) proceedings Symposium on the Theory of Computing*, 2000.

[60] Markus Cristinziani. *Search for Heavy Antimatter and Energetic Photons in Cosmic Rays with the AMS-01 Detector in Space*. PhD dissertation, University of Geneva, Department of Physics, February 2002.

[61] Vitaly Choutko and Ben Monreal. Private Communication.

[62] Vitaly Choutko. AMS Trigger During Shuttle Flight. AMS internal report, May 1998.

[63] D. Alvisi et al. A high resolution, low power time-of-flight system for the space experiment AMS. *Nuclear Instruments and Methods in Physics Research A*, 437:212–221, 1999.

[64] J.C. Hart and D.H. Saxon. Track and Vertex Fitting in an Inhomogeneous Magnetic Field. *NIM*, 220:309–326, 1984.

[65] R. Frühwirth. Application of Kalman Filtering to Track and Vertex Fitting. *NIM*, A262:444–450, 1987.

[66] Particle Data Group. Review of Particle Physics: Passage of Particles Through Matter. *Physics Letters B*, 592:242–253, 2004.

[67] Vitaly Choutko. AMS Simulation Software Overview. AMS Internal Presentation, January 1997.

[68] Vitaly Choutko. Search for AntiProtons with AMS at STS91. AMS Internal Presentation, February 1999.

[69] Vitaly Choutko. Search for Double Charged Anomalous CR with AMS at STS91. AMS Internal Presentation, July 2002.

[70] Mike Capell and Alexei Lebedev. AMS Data Formats. AMS Internal Report, October 1997.

[71] Vitaly Choutko. On the Alignment of the AMS SI Tracker by Means of Charged Particles. AMS Internal Paper, January 1996.

[72] J.D. Sullivan. Geometrical Factor and Directional Response of Single and Multi-Element Particle Telescopes. *NIM*, 95:5–11, 1971.

[73] Vitaly Choutko. AMS Proton Trigger Acceptance Study. AMS Internal Presentation, June 1999.

[74] F. James. *MINUIT: Function Minimization and Error Analysis.* CERN Computing and Networks Division, Geneva, Switzerland, version 94.1 edition, August 1998.

[75] Sa Xiao and Peter Fisher. Private Communication.

[76] Peter Fisher. Private Communication.

[77] Paolo Maestro. *Indirect Search for Dark Matter by Measurements of the Cosmic Ray Positron Spectrum with the AMS-02 experiment.* PhD dissertation, INFN University of Siena, Physics Department, September 2003.